Experimental and numerical studies of electrothermal phenomena in micro-scale thermoelectric systems

D I S S E R T A T I O N

zur Erlangung des akademischen Grades

Doktoringenieur (Dr.-Ing.)

vorgelegt

der Fakultät Maschinenwesen

der Technischen Universität Dresden

von

M. Sc. David Alberto Lara Ramos

geboren am 28.03.1990 in Coatzacoalcos, Mexiko.

Erstgutachter: Prof. Dr. Kornelius Nielsch

Zweitgutachter: Prof. Dr. Michael Beitelschmidt

Drittgutachter: Prof. Dr. Peter Woias

Fachbetreuerin: Dr. habil. Gabi Schierning

Eingereicht am 31.03.2020

Die Dissertation wurde in der Zeit von 06/2016 bis 03/2020 am Leibniz-Institut für Festkörper- und Werkstoffforschung Dresden angefertigt.

This work is dedicated to all victims of organized and unorganized crime in Mexico.

Acknowledgements

During my three-month research stay for this doctoral thesis in West Lafayette I had the opportunity to visit the Willis Tower in Chicago and get to know the outstanding success story of the migrants Fazlur Rahman Khan and Bruce Graham who built this impressive building. Ever since, their story reminds me that extraordinary things can only be achieved if people are wholeheartedly willing to give everything to make their dreams come true. However, every major achievement is also a synergy effect of the efforts of a large number of participants, and even great achievers such as Mr. Kahn and Mr. Graham could not have built a single wall of their masterpiece without the help of a large number of people involved in every step.

In a similar manner, this thesis has been the result of a long process that started in the winter of 2015, when I began to apply for positions as doctoral candidate in Germany. It is impossible to acknowledge here everyone that helped me throughout these years, but I am grateful to all of them.

First, I want to sincerely thank the people that helped me to grow professionally: my scientific supervisors within the IFW-Dresden: Dr. habil. Gabi Schierning, Dr. Nicolas Perez, Dr. Heiko Reith, and Prof. Dr. Kornelius Nielsch. Thank you for giving me the chance to join the thermoelectric group and investing your precious time on the development of my work within the group. This thesis would not have been possible without your patience, guidance, effort, and support in both professional and personal situations.

I want to thank my colleagues at the IFW-Dresden, with a special mention to: Vida Barati, Ignacio Gonzalez, Bruno Magalhaes, Aditya Dutt, Lauritz Schnatmann, Felix Thiel, and Constantin Wolf. Thank you for the memorable time and also for your support in many different aspects.

I want to express my sincere gratitude to Prof. Dr. Ali Shakouri and Dr. Kerry Maize from the Birck Nanotechnology Center in Purdue University. Thank you for your constant guidance and encouragement and for giving me the chance to visit the Quantum Engineered Systems and Technology group.

I acknowledge the Consejo Nacional de Ciencia y Technologia (CONACYT) for founding my Ph.D. at the IFW-Dresden and earlier my M.Sc. studies at the University of Sheffield in the United Kingdom.

I feel very happy and fortunate that during my stay in Dresden I got to know people that are now a fundamental part of my life, my “hermanitos”: Alex Bereza, Daniel Dzekan, Sebastian Maletti, and Jonas Zehner. I simply cannot be grateful enough for all the things that I have learned from you and for all the great moments that we have shared. Thank you for being such reliable and honest friends. I am looking forward for our next adventure together, gentlemen.

I thank my friends for life Sergio, Andrea and Rafita, that I unfortunately don't have the chance to frequent as much as I would like to, but are always going to have a special place in my heart. I know that every time I need you, you are going to be there for me.

Foremost, I want to thank my family. First, my parents Montserrat Ramos Barges and Manuel Lara Soto for everything that they have done for me, for their unconditional love, support, and vivid example of hard work, discipline, and a genuine desire to help others. I thank my siblings Jorge Isaac, Manuel, Montserrat and Maria Esther for helping me with everything I needed. And of course, I thank the next generation that has come to our life to enlighten it, my nephews Manuel, Pablo, Jennifer, Meztli, Jordi, Fatima, Uriel, Maria Jose and Andre.

I want to thank the Eisentraut family, especially Rita, Georg, Klaus, Manuel, Lucia, Diddi, Christel, Franz and Christine. You have not only made me feel at home during my stay in Germany, but also have earnt a very special place in my heart after so many extraordinary experiences together.

The particularly important last space is dedicated to my best friend and companion in good and bad times: my girlfriend Irene Eisentraut. Thank you for your support, interest, and especially for all your patience. It is clear for me that without your help this project would not have been possible in the first place. You are not only a cornerstone for this thesis, but also for my entire life. Throughout the years we have already achieved great accomplishments together and I am convinced that we will be unstoppable if we keep on supporting each other as much as we do now.

Erklärung der Urheberschaft

Hiermit versichere ich, dass ich die vorliegende Arbeit ohne unzulässige Hilfe Dritter und ohne Benutzung anderer als der angegebenen Hilfsmittel angefertigt habe; die aus fremden Quellen direkt oder indirekt übernommenen Gedanken sind als solche kenntlich gemacht.

Weitere Personen als die jeweils angegebenen waren an der geistigen Herstellung der vorliegenden Arbeit nicht beteiligt. Insbesondere habe ich nicht die Hilfe eines kommerziellen Promotionsberaters in Anspruch genommen.

Dritte haben von mir keine geldwerten Leistungen für Arbeiten erhalten, die in Zusammenhang mit dem Inhalt der vorgelegten Dissertation stehen.

Die Arbeit wurde bisher weder im Inland noch im Ausland in gleicher oder ähnlicher Form einer anderen Prüfungsbehörde vorgelegt und ist auch noch nicht in seiner Gesamtform veröffentlicht worden.

Die Promotionsordnung der Fakultät Maschinenwesen vom 1. Juli 2001 wird anerkannt.

Dresden, 31. Marz 2020.

David Alberto Lara Ramos

Summary

In recent decades the development of technologies capable to offer highly localized and precise temperature control has received increasing attention due to their relevance and applicability in numerous engineering fields. Multiple scientific papers have been written that focus on the enhancement of the performance of thermoelectric materials and micro-devices.

This Ph.D. thesis in the field of Mechanical Engineering pursues three main research goals regarding electrothermal phenomena: (1) To provide an optimization design strategy for micro-thermoelectric coolers by analyzing the interplay between electrical and thermal fluxes during device operation. (2) To analyze the suitability of a device, based on micro-thermoelectric coolers, for controlling the thermal environment in microbiological systems. (3) To develop an experimental technique, based on optical pump-probe thermal imaging, to extract the thermal conductivity anisotropy of thin films. For this purpose, numerical simulations and experiments were carried out.

The results show, that the design of micro-thermoelectric devices must take into account the impact of parameters that are typically neglected in the construction of macro scale devices. Poorly designed parameters, such as the metallic contacts, the distance between thermoelectric elements and their interaction with the substrate, carry severe reductions of the performance of micro-thermoelectric devices. It is demonstrated that the optimal performance is achieved when the thermoelectric legs are properly dimensioned, so that a balance of the Fourier and Joule fluxes is reached.

Numerical analyses prove that micro-thermoelectric coolers offer a feasible alternative to overcome the current spatial and temperature limitations of conventional technologies and therefore enable to investigate the thermal environment of biological systems at the micro-scale. Guidelines for the implementation of the experimental platform are provided.

The evaluation of the numerical and experimental data proves that optical pump-probe thermal imaging is suitable to characterize both the in-plane and the through-plane thermal conductivity of thin films. The experimental conditions to extract the anisotropy of the sample under study are determined.

The outcome of this work yields new insights into electrothermal phenomena at the micro-scale and thus creates new routes in the design, fabrication and characterization of micro- thermoelectric materials and devices.

Zusammenfassung

In den letzten Jahrzehnten hat die Entwicklung von Technologien, die eine genau lokalisierbare und präzise Temperaturregelung ermöglichen, aufgrund ihrer Relevanz und Anwendbarkeit in einer Vielzahl technischer Bereiche vermehrt Beachtung gefunden. Zahlreiche wissenschaftliche Arbeiten, die sich auf die Verbesserung der Leistung von thermoelektrischen Materialien und Mikrogeräten konzentrieren, wurden verfasst.

Folgende Dissertation im Bereich Maschinenbau verfolgt drei Hauptforschungsziele in Bezug auf elektrothermische Phänomene: (1) Bereitstellung einer Optimierungsstrategie für mikrothermoelektrische Kühler durch Analyse des Zusammenspiels zwischen elektrischen und thermischen Flüssen während des Gerätebetriebs. (2) Analyse der Eignung einer auf mikrothermoelektrischen Kühlern basierenden Vorrichtung zur Kontrolle der thermischen Umgebung an mikrobiologischen Systemen. (3) Entwicklung einer experimentellen Technik, basierend auf der optischen Pump-Probe-Wärmebildgebung, zur Bestimmung der Wärmeleitfähigkeitsanisotropie von Dünnschichten. Dazu wurden numerische Simulationen und Experimente durchgeführt.

Die Ergebnisse zeigen, dass beim Entwurf von mikrothermoelektrischen Geräten die Auswirkungen von Parametern berücksichtigt werden müssen, die bei der Konstruktion von gleichartigen Geräten im Makromaßstab meist vernachlässigt werden. Unzureichend beachtete Konstruktionsparameter, wie die metallischen Kontakte, der Abstand zwischen thermoelektrischen Elementen und ihre Wechselwirkung mit dem Substrat, führen zu einer erheblichen Leistungsminderung bei mikrothermoelektrischen Bauelementen. Es wird bewiesen, dass die optimale Leistung erreicht wird, wenn die thermoelektrischen Paare richtig dimensioniert sind, so dass ein Gleichgewicht der Fourier- und Joule-Flüsse erreicht wird.

Numerische Analysen zeigen, dass mikrothermoelektrische Kühler eine praktikable Alternative darstellen, um die aktuellen Limitationen bezüglich Temperatur und Raum der herkömmlichen Technologien zu überwinden und so die thermische Umgebung biologischer Systeme im Mikromaßstab zu untersuchen. Es werden Richtlinien für die Implementierung der experimentellen Plattform aufgestellt.

Die Auswertung der numerischen und experimentellen Daten beweist, dass die optische Pump-Probe-Wärmebildgebung geeignet ist, sowohl die Wärmeleitfähigkeit von Dünnschichten in der Ebene als auch in der Querebene zu charakterisieren. Die experimentellen Bedingungen zur Bestimmung der Anisotropie der untersuchten Probe werden definiert.

Die Ergebnisse dieser Arbeit liefern neue Einblicke in die elektrothermischen Phänomene im Mikromaßstab und eröffnen somit Innovationen bei der Konstruktion, Herstellung und Charakterisierung von mikrothermoelektrischen Materialien und Bauelementen.

Table of content

Acknowledgements IV
Erklärung der Urheberschaft VI
Summary VII
Zusammenfassung VIII
Table of content IX
List of figures XI
List of tables XIV
Abbreviations and symbols XV
1 Introduction 1
1.1 Motivation 1
1.2 Outline of the thesis 4
1.2.1 Chapter 2 - Fundamentals 4
1.2.2 Chapter 3 - Design guidelines of micro-thermoelectric coolers 4
1.2.3 Chapter 4 - Development of a platform for biological systems experimentation 4
1.2.4 Chapter 5 - Development of a technique for thermal transport characterization in thin films 5
1.2.5 Chapter 6 - Main conclusion and future research 5
1.3 Main research objectives 5
2 Fundamentals 7
2.1 Thermoelectric phenomena 7
2.2 Performance estimation of micro-thermoelectric coolers 10
2.3 Finite element modelling 12
2.3.1 Introduction to finite element modelling 12
2.3.2 Finite element modelling of thermoelectric phenomena 17
2.4 Thermoreflectance imaging microscopy 19
3 Design guidelines of micro-thermoelectric coolers 26
3.1 Introduction 26
3.2 Micro-thermoelectric coolers: an alternative for thermal management 28
3.3 Analysis approach 29
3.3.1 Input current optimization 31
3.3.2 Metallic contacts 32
3.3.3 Leg pair geometry 35

3.3.4 Fill factor 38
3.3.5 Experimental characterization of μTECs 41
3.4 Summary 44
4 Development of a platform for biological systems experimentation 46
4.1 Introduction 46
4.2 Thermal analysis on biological systems 48
4.3 Platform conceptual proposal 50
4.4 Analysis approach 52
4.4.1 Input current optimization 52
4.4.2 Fill material 54
4.4.3 Thermotaxis 55
4.4.4 Top material 56
4.4.5 Cold spot optimization 58
4.5 Experimental platform construction 59
4.6 Summary 62
5 Development of a technique for thermal transport characterization in thin films 64
5.1 Introduction 64
5.2 Thermal anisotropy characterization in thin films 65
5.3 Experimental apparatus 66
5.4 Experimental measurements 69
5.5 Analysis approach 72
5.5.1 Thermal conductivity anisotropy analysis 76
5.5.2 Effect of the laser power on the temperature distribution 79
5.5.3 Enhancement of the system sensitivity 80
5.6 Summary 83
6 Main conclusion and future research 85
6.1 Main conclusion 85
6.2 Outlook 88
7 References 89
8 Scientific output 97
8.1 Publications in peer review journals 97
8.2 Selected conference abstracts 98
9 Curriculum vitae 99

List of figures

Figure 1. Experimental and simulation of the cooling performance of μTECs. 1
Figure 2. Schematic of the proposed integration of μTECs and photonics systems. 2
Figure 3. Schematic diagrams of a simple thermocouple. 7
Figure 4. Schematic diagram of the Thomson effect. 9
Figure 5. Schematic diagram of a single leg pair thermoelectric cooler and its components. . 10
Figure 6. Summary of mesh convergence analysis. 14
Figure 7. Impact of the mesh refinement on the calculated temperature field. 16
Figure 8. Temperature and electrical field distribution of an array of μTECs. 18
Figure 9. Diagram of the thermoreflectance imaging basic principle. 20
Figure 10. Schematic diagram of the thermoreflectance imaging experimental set up. 21
Figure 11. Experimental set up of electrically pumped thermoreflectance imaging microscopy. 22
Figure 12. Diagram of the thermoreflectance imaging timing signals. 23
Figure 13. Relationship between thermoreflectance coefficient and illumination wavelength for Gold, Titanium, Nickel and Aluminum. 24
Figure 14. Schematic fabrication line for integrated μTECs and corresponding secondary electron images. 26
Figure 15. Schematic diagram of a single leg pair μTEC. 29
Figure 16. Simulation results of the impact that I presents on ΔT for baseline geometry. 31
Figure 17. Schematic diagram of the initial and final data points for the metallic contact analysis of a μTEC. 32
Figure 18. Relationship between metallic contact thickness, ΔT and R. 33
Figure 19. Relationship between ΔT and R for the baseline μTEC as a result of the metallic contacts thickness variation. 33
Figure 20. Variation of the temperature distribution as a result of the TCT variations. 34
Figure 21. Dependency of the electrical field lines distribution as a result of BCT variations. 34
Figure 22. Schematic diagrams of the geometry variations for the thermoelectric leg geometry 35

Figure 23. Interrelation of heat fluxes and resulting ΔT and COP for geometry variations of the thermoelectric legs. 36

Figure 24. ΔT as a result of the heat flux balance between $\dot{Q}_{Fourier}$ and $\dot{Q}_{Joule}$ 37

Figure 25. Scanning electron microscopy of an array of µTECs constructed by ECD. 38

Figure 26. Schematic diagram of the study cases for the FF analysis 39

Figure 27. Dependency of ΔT, T_2 and R as a result of FF variation. 40

Figure 28. Thermal imaging characterization of µTEC device. 42

Figure 29. Correlation between the numerically and experimentally obtained ΔT of a µTEC device. 43

Figure 30. Commercial use of solid state thermoelectric devices. 46

Figure 31. Schematic diagram of the proposed platform for experimentation on the thermal microenvironment of biological systems. 50

Figure 32. Schematics of the FEM used to analyze the effect that the fill material presents on ΔT 53

Figure 33. Summary of the FEM on the effect that the fill material presents on ΔT 53

Figure 34. Impact of λ_{fill} on ΔT. 54

Figure 35. Impact of λ_{fill} on ΔT across the µTEC device. 55

Figure 36. Impact of the encapsulating material thermal conductivity on ΔT across the µTEC device. 57

Figure 37. Effect of the top material thickness and distance between arrays of µTECs on ΔT across the µTEC device. 58

Figure 38. Schematic diagram of the proposed experimental implementation of the platform for thermal investigations in biological microsystems. 59

Figure 39. Photolithography mask design for the independently activated µTECs for thermal investigations in biological microsystems. 60

Figure 40. Photolithography mask for the chip containing the active µTECs and the PCB designed to externally connect the electrical control signal. 61

Figure 41. Mockup of the proposed experimental set up for the platform for thermal investigations in biological microsystems. 61

Figure 42. Experimental set up for optical pump-probe thermoreflectance imaging microscopy. 66

Figure 43. CCD image of the pump laser spot focused on the control sample surface. 68

Figure 44. Measured temperature map generated on the control sample surface. 68

Figure 45. Normalized profile of the laser pump spot focused on the surface of the sample under study. 69

Figure 46. Extracted profiles of the normalized pump reflectance, the measured temperature increase, and the Lorentzian fit of the control sample. 71

Figure 47. Schematic diagram of the FEM of the control sample used for optical pump-probe thermoreflectance imaging. 72

Figure 48. Summary of the temperature distributions obtained by experimental measurements and FEM simulation. 74

Figure 49. Effect of P_0 on the temperature increase. 75

Figure 50. Impact of the thin film thermal conductivity anisotropy on the temperature increase. 76

Figure 51. System sensitivity of small λ_z variations 77

Figure 52. System sensitivity of small λ_r variations 77

Figure 53. Effect of P_0 on the temperature increase 79

Figure 54. System sensitivity to variations of λ_r as a function of $\lambda_{substrate}$. 80

Figure 55. Improvement of the system sensitivity to variations of λ_z and λ_r as a function of $\lambda_{substrate}$. 81

List of tables

Table 1 Summary of common experimental methods for the thermal characterization of microsystems. 19

Table 2. Summary of device components baseline geometry for μTEC performance study... 29

Table 3 Geometry and material properties of the experimentally characterized μTEC for *FF* analysis. 41

Table 4. Geometry and material properties for analysis of μTEC for biological microsystems experimentation. 52

Table 5. Isotropic material properties and geometry of control sample used for optical pump-probe thermoreflectance imaging. 72

Abbreviations and symbols

Abbreviations

µTEC	micro-thermoelectric cooler
2D	two-dimensional
3D	three-dimensional
BCT	bottom contact
BEOL	back-end-of-line
CCD	charge-coupled device
CMOS	complementary metal-oxide semiconductor
COP	coefficient of performance
DOF	degrees of freedom
DRIE	deep reactive ion etching
ECD	electrochemical deposition
EMF	electromotive force
EP	electrical power input
FEM	finite element modelling
FF	fill factor
LED	light-emitting diode
MEMS	microelectromechanical system
NA	numerical aperture
PCB	printed circuit board
PCR	polymerase Chain Reaction
PDEs	partial differential equations
PMMA	poly methyl-methacrylate
TCT	top contact
TDTR	time domain thermoreflectance
TEC	thermoelectric cooler

Capital letters

$\dot{Q}_c$	cooling power
$\dot{Q}_{Fourier}$	Fourier heat flux
$\dot{Q}_{Joule}$	Joule heat flux
$\dot{Q}_{Peltier}$	Peltier cooling effect
$\dot{Q}_{Peltier\ heating}$	Peltier heating effect
$\dot{Q}_{Thomson}$	Thomson effect
C_{TH}	material thermoreflectance coefficient
D_{tec}	thermoelectric leg depth
H_{tec}	thermoelectric leg height
K_n	thermal conductance of the n-type thermoelectric leg
K_p	thermal conductance of the n-type thermoelectric leg
P_0	laser power
U_n	vector of unknown
W_{tec}	thermoelectric leg width
A	normal area
C	specific heat capacity
D	electric flux density vector
E	electric field intensity vector
F	source function
I	current flow
J	electric current density vector
K	thermal conductance
R	electrical resistance
S	standard deviation
T	temperature
V	electrical voltage
ΔV	potential difference
ΔT	temperature difference

Small letters

r_c	electrical contact resistance
a	location parameter in the x coordinate
b	location parameter in the y coordinate
c	linear gain factor
l	thermoelectric leg length
q	heat flow vector
t	time
u	dependent variable in a PDE

Greek symbols

α_n	Seebeck coefficient of the n-type thermoelectric material
α_p	Seebeck coefficient of the p-type thermoelectric material
$\lambda_{effective}$	effective thermal conductivity
λ_{fill}	thermal conductivity of the fill material
λ_r	in-plane thermal conductivity
$\lambda_{substrate}$	substrate thermal conductivity
λ_{top}	thermal conductivity of top material
λ_z	through-plane thermal conductivity
μ	mean value
φ	electric scalar potential
Λ	surface reflectivity
Υ	scale parameter
α	Seebeck coefficient
β	Thomson coefficient
ε	dielectric permittivity matrix
λ	isotropic thermal conductivity
π	Peltier coefficient
ρ	electrical resistivity

ς	density
σ	electrical conductivity matrix
τ	image acquisition delay time with respect to the pump
ψ	basis functions
ϕ	specific flow of heat sources
ϖ	global matrix

Subscripts

If not otherwise specified, the following subscripts refer to:

A	material A
B	material B
h	hot side
c	cold side
$device$	total value of a device
n	n-type thermoelectric material
p	p-type thermoelectric material
tec	thermoelectric leg

“Los grandes proyectos deben comenzar de la manera más sencilla.”

“The greatest projects must start in the simplest possible way.”

– Eugenio Garza Sada, mexican industrialist and philanthropist, * 1892 † 1973 –

1 Introduction

1.1 Motivation

The increasing performance demands on solid state electronic and photonic devices have pushed a constant tendency towards size reduction of components. Recent advances of deposition and micro-fabrication technologies can be used advantageously to increase the performance of micro-devices and expand their field of application. The miniaturization process has brought new challenges regarding highly localized heat fluxes. This compromises the component reliability and necessarily needs to be addressed. For instance, in the case of integrated circuits, the constant miniaturization of transistors carries high on-chip power density, which subsequently creates localized high temperatures [1].

Micro-thermoelectric coolers (μTECs) have received attention as a strategy for localized micro-scale thermal management, since they have unique attributes that make them particularly suitable for this task. They can be directly integrated at the chip level and they offer a precise and fast temperature response. Their operation is maintenance free and with high reliability [2-7]. To illustrate the cooling performance that such devices can provide under operation, the temperature response of a μTEC constructed by electrochemical deposition (ECD) reported by Li et al [2] is shown in Figure 1.

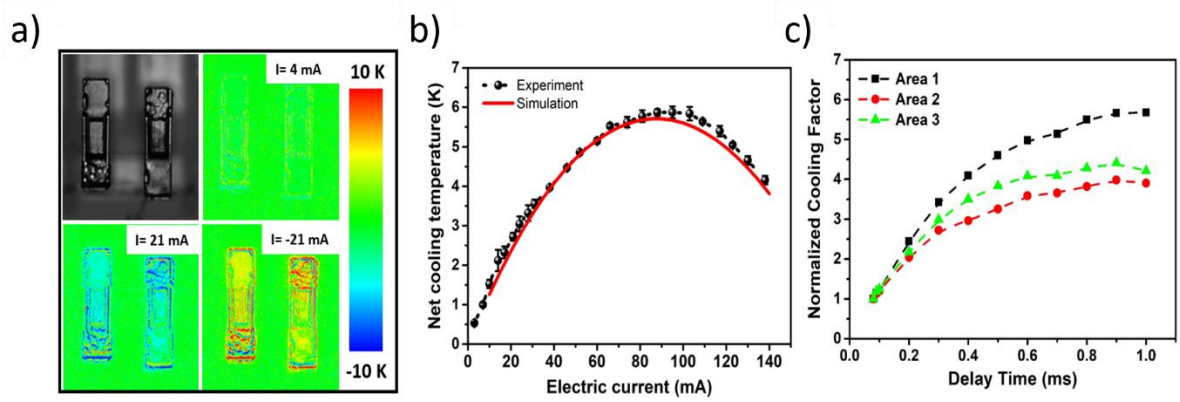

Figure 1. Experimental and simulation of the cooling performance of μTECs. a) Optical microscopy image of the device and temperature response with applied electric currents of 4, 21 and − 21 mA. b) Net cooling temperature of two leg pairs in the electric current range 5–140 mA at room temperature and in an ambient environment. The red curve shows the finite element simulation results. c) Dependence of normalized cooling factor on specific delay time, measured after switching on the electric current of 70 mA for three different areas of μTECs: n-leg of cooler 1 (black), bridge of cooler 1 (green) and n-leg of cooler 2 (red). The dashed lines are guides to the eye. All of the temperature images were obtained by thermoreflectance imaging. Further details of the geometry and material properties of the device can be found in [2].

The unique characteristics of μTECs make them also particularly suitable and advantageous in the field of integrated photonic devices for telecommunication, where high temperature control is needed during operation. Typically, temperature control in the range of ±0.1 °C is required to maintain the wavelength emission within design specifications [4-7]. Currently, state of the art thermal management solutions for photonic integrated circuit packages employ a system of thermoelectric coolers (TECs) and resistive heaters cooler by air, whereas both of these components are macro-size. This is an inefficient approach, since it requires considerable space and provides limited thermal design around the photonic device [4]. To remediate this, previous works have proposed the integration of micro-thermoelectric coolers directly with the target photonic devices, as shown in Figure 2. This innovative strategy represents a substantial improvement of the typical commercial solution for the thermal management. This design would increase the efficiency and allow greater levels of photonic component density than current technologies [4].

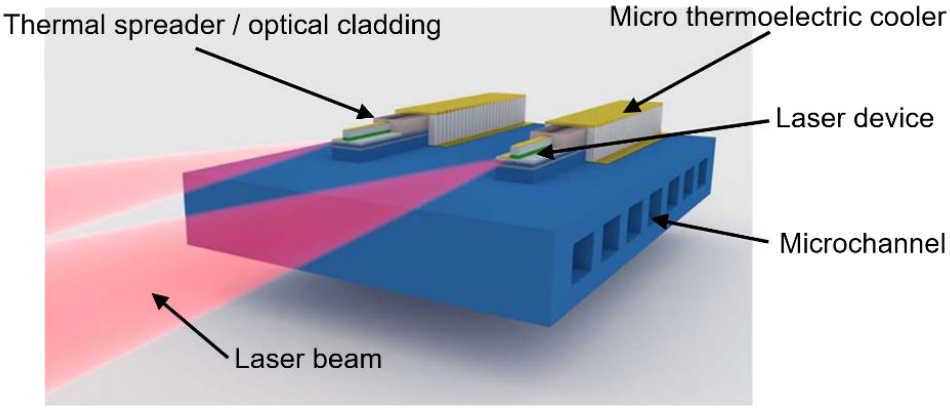

Figure 2. Schematic of the proposed integration of μTECs and photonics systems. In order to further optimize the system, a heat sink with microchannels can be integrated. Adapted from [4].

However, despite their attractive attributes and broad potential field of application, many aspects related to the study of thermoelectric devices at the micro-scale still remain largely unexplored. This includes: (1) The analysis of the effect that the thermomechanical design of μTECs has on the electrical and heat fluxes interplay during device operation and how these factors impact the device performance. (2) The implementation of an experimental platform to take advantage of the unique characteristics of μTECs in a practical application within the biological sciences. (3) The development of an experimental analysis technique for investigations of the thermal transport mechanism in thermoelectric materials deposited as thick and thin films.

It follows from the aforementioned aspects that consummating in-depth studies of thermoelectric materials and devices at the micro-scale would allow an extension of their applicability within a wide range of fields. This includes solid state photonic telecommunication

systems, micro-sensors, internet of things, biological sciences, micromechanical systems, micro-electronic devices and micro-integrated circuits.

In this regard, the scope of this work concerns the analysis of electrothermal phenomena at the micro-scale in three different fundamental aspects: (1) The development of a thermomechanical design strategy specifically tailored to optimize the performance of μTECs. (2) The development of an experimental platform, based on μTECs, for investigations of temperature effects on micro-biological systems. (3) The development of an experimental characterization technique capable to estimate the anisotropic thermal conductivity of thermoelectric materials deposited as thin films.

1.2 Outline of the thesis

The core subject of the present thesis is the study of electrothermal phenomena involved in thermoelectric materials and devices at the micro-scale. This work is composed of six chapters, whose content is detailed next.

1.2.1 Chapter 2 - Fundamentals

Basic principles and fundamental aspects related with the thesis are introduced. This involves the theoretical principles of thermoelectricity, the analysis and performance evaluation approaches of thermoelectric cooling devices, an overview of the finite element method and simulation of Multiphysics systems, and the introduction of a temperature measurement technique suitable for characterization of micro-thermoelectric devices.

1.2.2 Chapter 3 - Design guidelines of micro-thermoelectric coolers

Design optimization strategies for micro-thermoelectric coolers are investigated. In particular, the effect that key factors play in the performance of micro-thermoelectric devices is analyzed. A novel design approach specially tailored to reduce the detrimental effects involved in the design and construction of micro-devices is provided. Finally, a study is performed to experimentally estimate the thermal conductivity of the thermoelectric materials and the electrical contact resistances present in micro-devices.

1.2.3 Chapter 4 - Development of a platform for biological systems experimentation

Based on the results of Chapter 3, the particular factors involved in the conceptual development of an experimental platform suitable for the study of the micro-thermal environment in biological systems are examined. The study focuses on the analysis of key parameters for the integration of an array of micro-thermoelectric devices in a functional experimental platform and the impact of these parameters on the overall performance of the platform. The platform is designed to constrain the biological micro-system under study to highly localized temperature gradients. The conclusions provide design guidelines for the construction and implementation of an experimental platform with optimized performance.

1.2.4 Chapter 5 - Development of a technique for thermal transport characterization in thin films

This chapter proposes the use of a novel experimental approach to characterize thermal parameters of thin films, based on optical pump-probe thermoreflectance imaging. A previously characterized multilayer sample is used for the validation of this technique. The methodology used consists in generating and simultaneously measuring temperature maps generated on the surface of the validation sample. These experimental data are later used as a correlation parameters for a finite element model. The numerical model is then used to analyze the impact that the through-plane and in-plane thermal conductivities of the problem thin film as well as other key factors present on the generated temperature distribution. In this manner, a methodology to extract the thermal parameters of the studied sample is provided. Recommendations regarding how to further improve the sensitivity of the measuring technique are discussed.

1.2.5 Chapter 6 - Main conclusion and future research

The main conclusions are summarized and an outlook of future research lines is provided.

1.3 Main research objectives

The present work pursues three main objectives, as follows:

To examine by finite element modelling the impact that key design parameters have on the performance of micro-scale thermoelectric coolers.

To analyze by finite element modelling the impact that key design parameters carry on the performance of an experimental platform to control the thermal environment of microbiological systems.

To assess a method to characterize thermal conductivity anisotropy of materials deposited as thin films, based on optical pump-probe thermoreflectance imaging microscopy and finite element modelling.

“Ser paciente no significa ser pasivo, sino saber medir los tiempos y mantener la vista en la meta que queremos alcanzar.”

“Being patient does not mean being passive, but knowing how to measure time and circumstances, while keeping our eyes on the goal we want to achieve.”

– Lorenzo H. Zambrano, mexican entrepreneur and philanthropist, *1944 † 2014 –

2 Fundamentals

2.1 Thermoelectric phenomena

In the early XIX century Thomas Johann Seebeck discovered that if the junction of a closed loop conformed by two dissimilar conductors is heated up, a compass needle can be deflected when placed in its vicinity [8]. Seebeck originally concluded that this was the result of a magnetic effect. Today we know that this phenomenon underlies the conversion of heat into electrical power. Nevertheless, his findings represent the first reported studies on the thermoelectric effects and this phenomenon was named after him. The Seebeck effect can be explained if we consider that, when a temperature gradient is constrained between the end points of a finite isotropic conductor, the free carriers at the end with the higher temperature will acquire a higher kinetic energy than the ones at the cold side. Therefore, the first will start to diffuse towards the cold end. As a result, the accumulation of charge will generate an opposite electromotive force (EMF) that will oppose additional charge flow [9].

Jean Charles Athanase Peltier later observed that the flow of electrical current through the junction of two different electrical conductors leads to a heating or cooling, depending on its direction [10]. This is observed, when the flowing electrons present different energies in each of the materials that are joined. Thus, when they pass from one material to the other, the energy transported by the electrons is modified, and this differences emerge as heating or cooling at the junction [9, 11].

A simple circuit conformed of two different conductors (material A and material B), joined together at two different locations (junction i and junction ii) is used in Figure 3 to explain the principles discovered by Seebeck and Peltier [11]. As shown, an open circuit is allowed at material B, where a voltage can either be applied or measured.

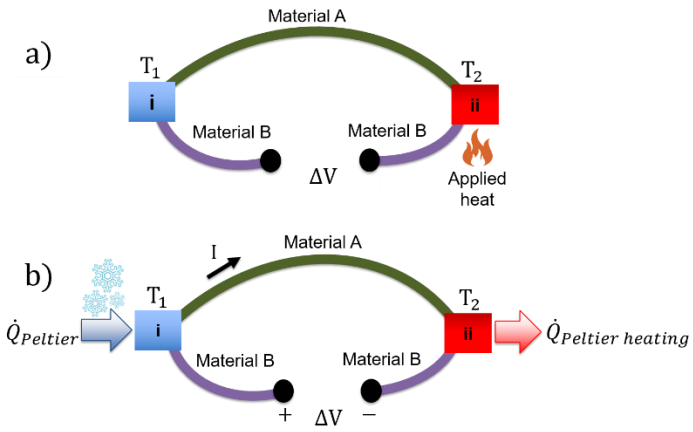

Figure 3. Schematic diagrams of a simple thermocouple. The thermocouple a) depicts the Seebeck effect, while b) shows the Peltier cooling effect. Adapted from [11].

Figure 3 a) shows that when heat is applied at the junction ii, while the temperature of junction i is kept constant, so that $T_2 > T_1$, a temperature gradient will be generated between both points. This is found by $\Delta T = T_2 - T_1$, where T_1 and T_2 are absolute temperatures, expressed in (K). As a result, a potential difference (ΔV) will be observed at the open circuit.

The relationship between ΔV and ΔT is linear for small temperature differences and it is known as the Seebeck coefficient of the junction AB, α_{AB}, found by

$$\alpha_{AB} = \frac{\Delta V}{\Delta T} \qquad \text{Eqn. 1}$$

where α_{AB} is expressed in (V/K), and ΔV in (V). This coefficient is considered conventionally as positive when the Seebeck voltage generates an electric current through conductor A from the junction with higher temperature to the one with lower [11].

The circuit of Figure 3 b) displays the complementary Peltier effect. If this time ΔV is applied to this circuit, an electrical current (I) will flow through it with a clockwise direction. As a result of this current flow a cooling effect ($\dot{Q}_{Peltier}$) will occur at the thermocouple junction i, where heat is absorbed, and a heating effect will occur at junction ii ($\dot{Q}_{Peltier\ heating}$), where heat is expelled. This effect may be reversed whereby a change in the direction of electric current flow will reverse the direction of heat flow.

The Peltier coefficient of the junction AB, π_{AB}, is considered as positive when the junction where the electrical flow enters to the material A is heated up and the other junction is cooled down. It can then be expressed mathematically as [9]

$$\pi_{AB} = \frac{\dot{Q}_{Peltier}}{I} \qquad \text{Eqn. 2}$$

where π_{AB} is expressed in (W A^{-1}). For practical proposes, it is much simpler to measure the Seebeck coefficient than the Peltier coefficient. Therefore, it is more convenient to use the first to characterize the thermoelectric properties of a material. The relationship between these coefficients was investigated by William Thomson (later known as Lord Kelvin), who applied the thermodynamics theory to determine that the Peltier and Seebeck effects keep a relationship, found by [12].

$$\pi_{AB} = \alpha_{AB} T \qquad \text{Eqn. 3}$$

This equation is called as the Kelvin relation. Lord Kelvin also found another phenomena, the Thomson effect, which relates the rate of generation of reversible heat, led by the current flow along a section of a single conductor, which is at the same time subjected to a temperature gradient [12]. According to him, if this temperature gradient is small, it can be expressed that [9]

$$\dot{Q}_{Thomson} = \beta I \Delta T \qquad \text{Eqn. 4}$$

where, β is the Thomson coefficient and it is expressed in (V/K). This principle is depicted in the diagram shown in Figure 4.

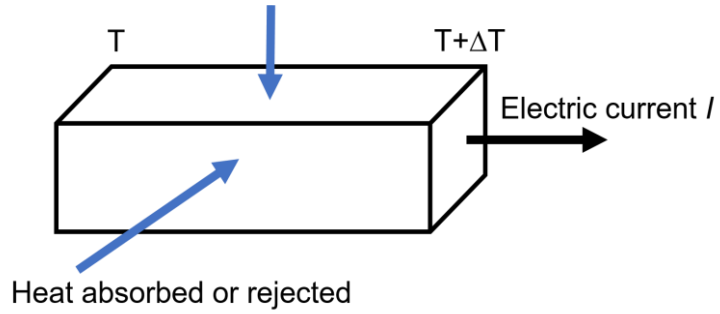

Figure 4. Schematic diagram of the Thomson effect. Adapted from [9].

The Thomson effect has a similar source as the Peltier effect. The difference among them is that for the case of the Thomson effect, the temperature gradient that causes differences in the potential energy of the charge carriers and in the scattering mechanisms is present along the conductor material itself. Both effects keep a relationship, described in Equation 5 [9]

$$\frac{d\alpha_{AB}}{dT} = \frac{\beta_A - \beta_B}{T} \qquad \text{Eqn. 5}$$

where β_A and β_B refer to the Thomson coefficients of the materials A and B, respectively. The impact of the Thomson effect is considered to be relatively small and therefore, it is often neglected in design calculations of thermoelectric devices for simplification purposes.

Until this point, α has been defined for a pair of different conductors, which are typically known as relative coefficients. Fortunately, it can be derived from the Kelvin relations that the measured α_{AB} is a contribution from both joint conductors, as expressed in Equation 6 [9]

$$\alpha_{AB} = \alpha_A - \alpha_B = \frac{\Delta V_A}{\Delta T} - \frac{\Delta V_B}{\Delta T} \qquad \text{Eqn. 6}$$

where α_A and α_B refer to the absolute Seebeck coefficient of conductor A and B, respectively. In this manner, if the absolute Seebeck coefficient of one reference conductor is known, the other can be extracted by measuring the Seebeck coefficient of the junction [9].

Although the aforementioned concept for the Seebeck coefficient measurement is straightforward, the practical implementation of a measurement carries difficulties that necessarily need to be thoughtfully considered [13, 14].

2.2 Performance estimation of micro-thermoelectric coolers

A single leg pair thermoelectric cooler is composed by a p- and n-type thermoelectric leg pair, a substrate, which functions as a heat sink, and bottom and top metallic contacts. As shown in the schematics in Figure 5 the temperatures under operation that a micro-thermoelectric cooler (μTEC) achieves at its hot and cold sides, T_h and T_c, are crucial parameters for its performance characterization. Nevertheless, estimating those values accurately requires to numerically calculate approximate solutions of the thermoelectricity coupled equations, such as heat transfer, thermoelectric effect and electric current. For this, the use of advanced numerical simulation tools, such as finite element modelling is useful. Once T_h and T_c are known, it is possible to calculate relevant performance characterization criteria.

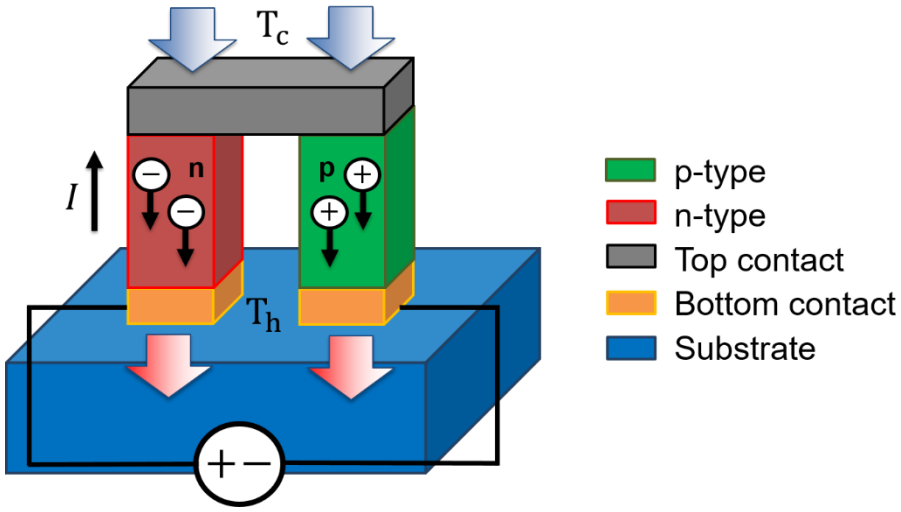

Figure 5. Schematic diagram of a single leg pair thermoelectric cooler and its components. An external electrical current is employed to drive the diffusion of carriers and holes in the n- and p-type thermoelectric elements.

As shown in Figure 5, when I is applied to the device, $\dot{Q}_{Peltier}$ will take place at the cold junction. This can be expressed mathematically by combining Eq 2, Eq 3 and Eqn. 6 and by substituting T_c and the Seebeck coefficients of the p- and n-type thermoelectric materials, α_p and α_n, which leads to

$$\dot{Q}_{Peltier} = (\alpha_p - \alpha_n) I T_c \qquad \text{Eqn. 7}$$

This will be opposed by two different factors: the Fourier heat conduction, $\dot{Q}_{Fourier}$, and the joule heating, $\dot{Q}_{Joule}$. The first refers to the heat transferred by the diffusion of energy as vibrating atoms interact with neighboring particles, which subsequently transfer kinetic and potential energies in the presence of a temperature gradient. The second factor refers to the increase of temperature that occurs as a result of the collision of electrons with atoms in the

lattice of a conductive material, as the electrons flow through it. For the μTEC shown in Figure 5, these competing mechanisms are described in Equations 8 and 9, respectively.

$$\dot{Q}_{Fourier} = (T_h - T_c)K_{device} \quad \text{Eqn. 8}$$

$$\dot{Q}_{Joule} = I^2 R_{device}/2 \quad \text{Eqn. 9}$$

K_{device} stands for the total thermal conductance of the device, which includes the contribution of the p- and n-type thermoelectric legs, K_p and K_n, respectively. R_{device} refers to the total electrical resistance of the device, including the contribution of the thermoelectric legs, the metallic contacts, and the electrical contact resistances.

For each material the thermal conductance, *K*, is found by $K = \frac{\lambda A}{l}$, being λ the thermal conductivity of the material, *A* the thermoelectric leg normal area and *l* the thermoelectric leg length. Likewise, the electrical resistance of each material, *R*, is found by $R = \rho \frac{l}{A}$, where ρ refers to the electrical resistivity.

It should be noted that Equation 9 considers that half of the total $\dot{Q}_{Joule}$ accounts to the heat balance at the cold side and the other half to the hot side, which is an often done assumption for the analysis of macro thermoelectric coolers.

By considering these three factors, the heat flux balance at the cold side of a thermoelectric device can be obtained, expressed as the device cooling power, $\dot{Q}_c$ and described as:

$$\dot{Q}_C = \dot{Q}_{Peltier} - \dot{Q}_{Fourier} - \dot{Q}_{Joule} \quad \text{Eqn. 10}$$

The coefficient of performance, *COP*, of a thermoelectric cooler is defined as the ratio between $\dot{Q}_C$ and the electrical power input, *EP*, expressed as

$$COP = \dot{Q}_c/EP \quad \text{Eqn. 11}$$

where EP is defined as the product of I and the electrical voltage, V.

2.3 Finite element modelling

2.3.1 Introduction to finite element modelling

Finite element modelling (FEM) is a numerical analysis tool that was originally developed for structural analysis in the aerospace and automotive industry. Driven by the constant improvement of computational capabilities of modern computers as well as further improvement of mathematical theory, FEM has been under constant expansion since the middle of the XX century, when the usefulness of the method was first recognized [15].

Today, FEM has become a powerful tool in a wide range of applications across various disciplines, such as heat transfer, fluid flow, mass transport, electromagnetic potential and multi-physics studies [16].

In the aforementioned fields, partial differential equations (PDEs) are widely used in order to describe physical problems. However, for the vast majority of issues, these systems of PDEs cannot be solved analytically in their infinite dimensional function space. Instead, discretization methods can be used to transfer the PDEs in a finite dimensional function space as first functions. After this step, they can be converted into ordinary vectors within a vector space. Later, well-known numerical methods can be used to solve such vector systems. In this way, approximate solutions of physical problems can be obtained by using linear combinations of basis functions, according to Equation 12 and 13 [16].

$$u \approx u_h \qquad \text{Eqn. 12}$$

$$u_h = \sum_{i=1}^{n} u_i \psi_i \qquad \text{Eqn. 13}$$

The function u is the dependent variable in a PDE and the function u_h is an approximation of the function u. The basis functions are defined by ψ_i and their coefficients are defined by u_i [16].

The aforedescribed systematic method is the mathematical working principle behind FEM. However, the complete process of implementing FEM for a real application involves a conceptual, mathematical, numerical, and computational modelling.

The first step requires to build a geometrical representation within a FEM software and to define the system physical properties that can be temperature dependent. Therefore, an idealization of the reality needs to be executed.

The next step is to build a mathematical model of the studied system. This is achieved by describing the arrangement of partial differential equations that govern the physical behavior of the studied system as well as the corresponding boundary conditions.

Next, this mathematical model, expressed with PDEs as differential form or so called strong form, needs to be transformed into its equivalent integral form, also called weak form. Generally, this is achieved with the use of energy principles, methods like the Galerkin method. The weak formulation makes it possible to discretize the mathematical model equations that are found in an infinite continuum space, into a numerical model equations composed of a finite number of points, also called finite elements.

Elements are formed by two or more nodes, located at their vertices. Nodes are discrete points in which field variables are explicitly considered and where the unknowns will be calculated from the field variables. The fact that common nodes are shared among adjacent elements creates a continuum. Nevertheless, shape functions or interpolation functions need to be defined in order to calculate the field variables inside the elements by interpolation from the nodal values calculated.

Afterwards, the so called stiffness matrix of each element is formed considering them to be independent from each other. However, this is not the case, since they are solely interconnected. Hence, an assembly step is undertaken to bring together a global system matrix that considers the nodal information of each element. After applying the boundary condition to the system, a set of simultaneous algebraic equations is described as

$$[\varpi]\,\{U_n\} = \{F\} \qquad \text{Eqn. 14}$$

where F refers to the source function, U_n to the vector of unknown, $U_n = \{U_1, \ldots, U_i, \ldots, U_n\}$ and ϖ to a global $n\ x\ n$ matrix that contains the coefficients of U_i in each equation j within its components B_{ji}. The global matrix receives different names depending on the field of engineering considered. For example, it is called as “stiffness” matrix for the case of structural mechanics or “conductance” matrix for the case of heat transfer studies.

Finally, a solution of this discretized model can be obtained by computational processes and algorithms. At each of the nodal points a solution of this global system of algebraic equations can be found. This is typically performed by an iterative solver that calculates a series of different solutions until the error, found by Equation 15, is almost zero.

$$[\varpi]\{U_n\} - \{F\} \approx 0 \qquad \text{Eqn. 15}$$

Nevertheless, there will always exist certain numerical uncertainty, since an exact solution with zero error cannot be achieved when real numbers are used.

In addition, a critical criterion involved in the accuracy of any finite element model is the mesh used for the analysis. The quality of the mesh must be assessed before any results can be extracted in a reliable manner from a finite element simulation. For the case of steady-state analysis, there are different mesh refinement strategies available, whereas each one of them present advantages and disadvantages. These techniques include the reduction of the element size, the incensement of the element order, the implementation of global and local adaptive mesh refinements, and the manual adjustment of the mesh.

Among these techniques, the latter represents the most labor intensive approach but also offers substantial savings in terms of computational resources, since it allows to refine the mesh only in the areas of interest. Optimizing the number of elements in the model becomes more and more relevant as the complexity of the analyzed system increases, since a larger number of elements in a model causes a larger number of degrees of freedom (DOF). DOF refers to the amount of variables that are computed at the nodes. This is a critical parameter, since the required cost of the solution increases with the square of number of DOF [17].

The impact that the mesh quality presents on the precision of FEM is exemplary summarized in Figure 6. Thereby, the evolution of the temperature increase as a result of the number of DOF considered within the FEM is shown. For this analysis, the number of DOF were incremented by performing a manual adjustment of the element sized of the mesh, as shown in Figure 7.

The simulated temperature increase was calculated at the center of excitation where a laser beam with a Gaussian profile thermally excites a sample kept at ambient conditions and room temperature. The system under analysis was defined as a thin film sample consisting of a 100 nm thick TiN transducer and a 250 nm thick (TiAlSc)N thin film deposited on a 100 µm thick MgO substrate. The laser beam was defined to be focused on the sample surface with a standard deviation of 1 µm and with an intensity of 1 mW.

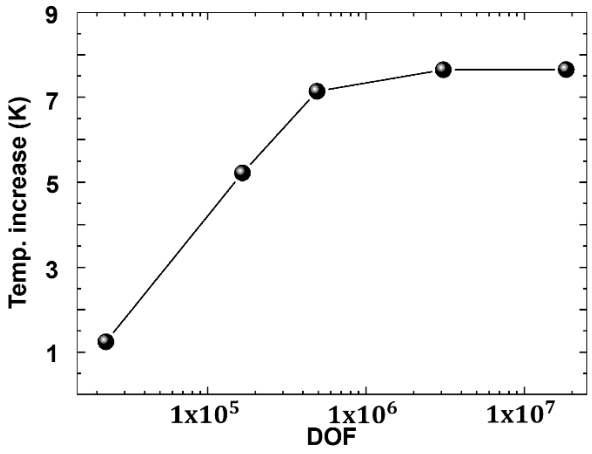

Figure 6. Summary of mesh convergence analysis. The graph shows the dependency of DOF and the calculated temperature increase of a multilayer TiN/AlScN/MgO sample as a result of a laser power with a Gaussian profile.

It can be observed from Figure 6 that as the number of elements present in the mesh is increased, the variations among the calculated temperatures is reduced. It can be concluded that mesh convergence was achieved when roughly $\sim 3 \times 10^6$ DOF were reached, since further increment of DOF until roughly $\sim 18.4 \times 10^6$ carries variations of only 0.06% among calculated temperatures. As observed in Figure 7 a), c), e), g) and i) for the studied case, the mesh refinement was performed by increment of the number of elements present in the area where

the laser beam was deposited, which allowed to optimize computational resources. The corresponding complete temperature fields are shown in Figure 7 b), d), f), h) and j).

Similarly to Figure 6 and 7, a mesh convergence analysis was performed for all the FEM results shown in the following chapters.

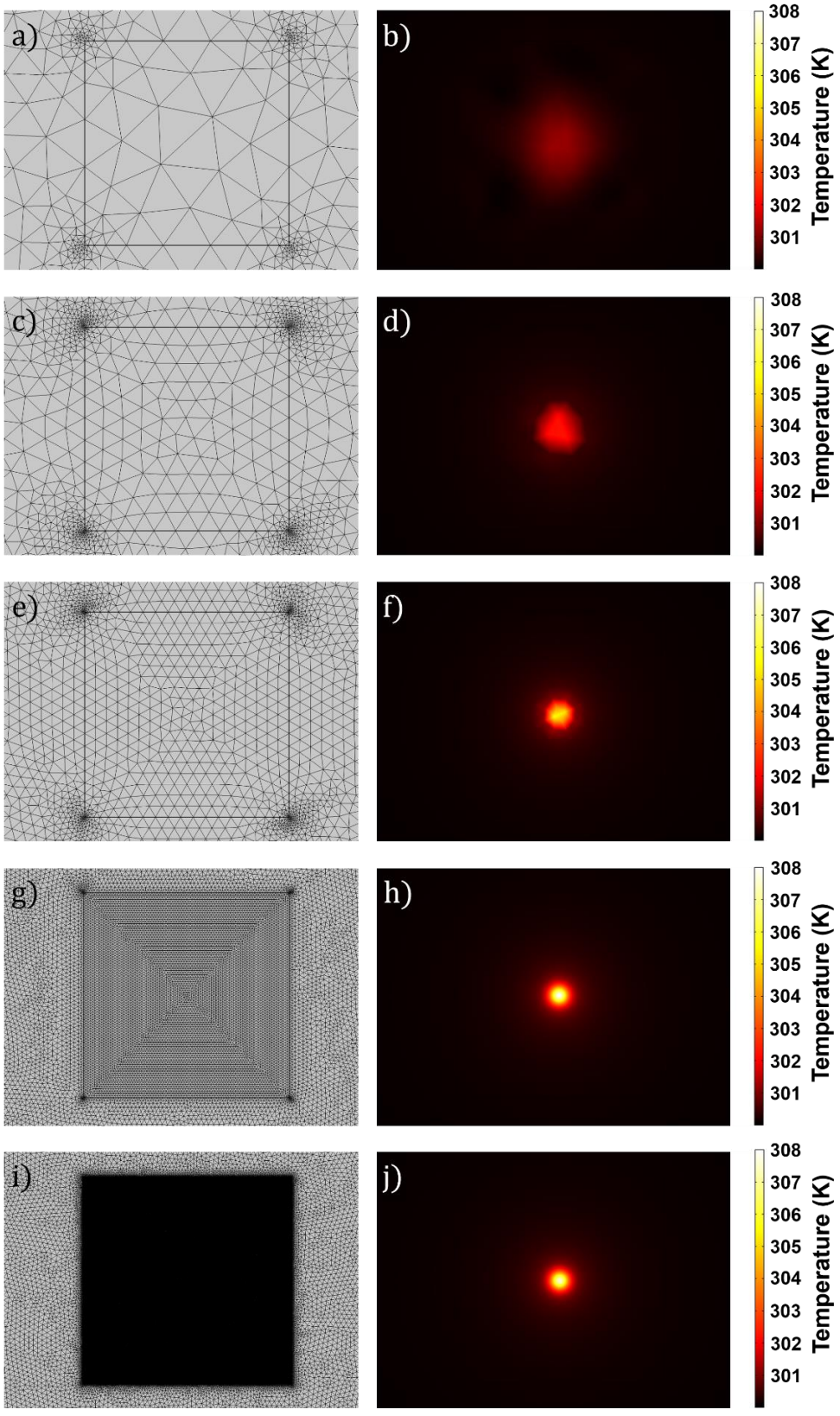

Figure 7. Impact of the mesh refinement on the calculated temperature field. The shown data points correspond to the cases of $\sim 22 \times 10^3$ DOF (a, b), $\sim 165 \times 10^3$ DOF (c, d), $\sim 491 \times 10^3$ DOF (e, f), $\sim 3.08 \times 10^6$ DOF (g, h) and $\sim 18.4 \times 10^6$ DOF (i, j).

2.3.2 Finite element modelling of thermoelectric phenomena

In order to accurately and efficiently analyze thermoelectric devices, a finite element formulation that includes the governing equations of thermoelectricity is required. These governing equations refer to the field equation for heat flow and for electric charge continuity, which are given by Equations 16 and 17, respectively [18, 19]

$$\varsigma C \frac{\partial T}{\partial t} + \nabla q = \phi \qquad \text{Eqn. 16}$$

$$\nabla \left(J + \frac{\partial D}{\partial t} \right) = 0 \qquad \text{Eqn. 17}$$

where ς stands for density, C for specific heat capacity, q for the heat flow vector, ϕ for the specific flow of heat sources, J for the electric current density vector, and D for the electric flux density vector. These field equations are coupled by the so called constitutive thermoelectric equations, given by Equations 18, 19 and 20 [18, 19]

$$q = [\pi] \cdot J - [\lambda] \cdot \nabla T \qquad \text{Eqn. 18}$$

$$J = [\sigma] \cdot (E - [\alpha] \cdot \nabla T) \qquad \text{Eqn. 19}$$

$$D = [\varepsilon] \cdot E \qquad \text{Eqn. 20}$$

where σ refers to the electrical conductivity matrix, E to the electric field intensity vector and ε to the dielectric permittivity matrix. If there are no variations of magnetic fields in time, the electric field can be derived from an electric scalar potential, φ, leading to Equation 21.

$$E = -\nabla \varphi \qquad \text{Eqn. 21}$$

A system of coupled equations of thermoelectricity can be derived if Equation 18-20 are substituted within Equations 16 and 17 [18, 19].

$$\varsigma C \frac{\partial T}{\partial t} + \nabla \cdot ([\pi] \cdot J) - \nabla \cdot ([\lambda] \cdot \nabla T) = \phi \qquad \text{Eqn. 22}$$

$$\nabla \cdot \left([\varepsilon] \cdot \nabla \frac{\partial \varphi}{\partial t} \right) + \nabla \cdot ([\sigma] \cdot [\alpha] \cdot \nabla T) + \nabla \cdot ([\sigma] \cdot \nabla \varphi) = 0 \qquad \text{Eqn. 23}$$

It should be noted that the terms λ, α, and π follow the notation earlier introduced in this work, with the exception that they are considered as matrixes in Equations 18 and 19.

The electric power $J \cdot E$, which is lost due to parasitic Joule Heating, is included in the heat generation term ϕ in Equation 20. Also, the displacement current, $\frac{\partial D}{\partial t}$, related to capacitive

effects is also considered for system completeness, despite its limited relevance to fast transient thermoelectric processes [19].

With these considerations, a properly constructed finite element model becomes a powerful tool to perform in-depth analyses of thermoelectric systems with high accuracy. This tool allows us to analyze the impact that key parameters present on the performance of the device under study within a high variety of scenarios. The analysis of thermoelectric modules in a FEM tool offer both quantitative and qualitative results with a user friendly graphical interphase, as exemplary shown in Figure 8. There, the coupled temperature and electrical distribution of an array of micro-thermoelectric coolers was calculated.

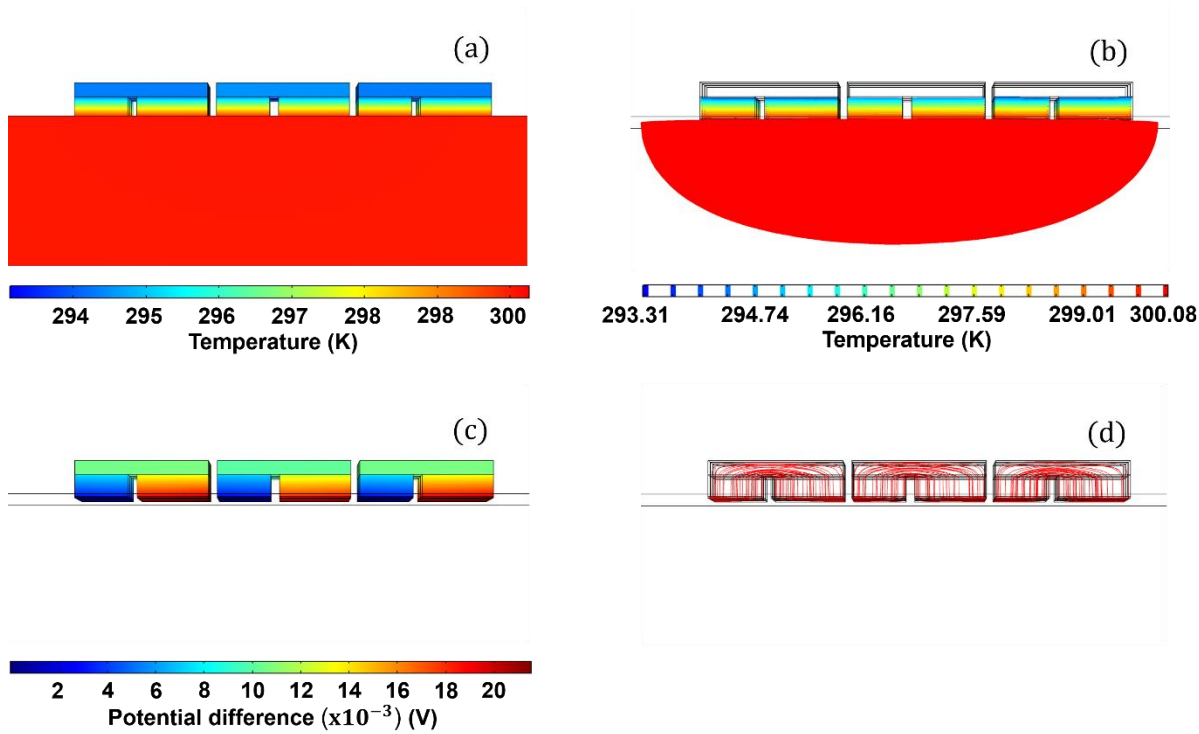

Figure 8. Temperature and electrical field distribution of an array of µTECs.a) Calculated temperature distribution of the device when a constant input current is applied. b) Isothermal contours plot of the µTEC under study. c) Calculated potential difference plot of the device. d) Calculated electric current lines.

2.4 Thermoreflectance imaging microscopy

The capability to thermally characterize micro-sized systems with high temporal and spatial resolution is paramount for the analysis of thermoelectric materials and devices. There are different commercially available experimental methods suitable for this task. These methods are based upon different principles and the present different experimental resolutions. Some of the most popular were summarized by Christofferson et al. [20], as listed in Table 1.

Method	Principle	Spatial resolution [μm]	Temperature resolution [K]	Time resolution [sec]	Imaging?
Micro-thermocouple	Seebeck effect	50	0.01	10-100	No
Infrared thermography	Plank blackbody emission	3-10	0.02-1	20μ	Yes
Liquid crystal thermography	Crystal phase transitions	2-5	0.1	100	Yes
Thermoreflectance imaging microscopy	Temperature dependence of reflection	0.3-0.5	0.01	0.006-0.1 μ	Yes
Scanning thermal microscopy (SThM)	Atomic force microscope with thermocouple tip	0.05	0.1	10-100 μ	Scan
Fluorescence thermography	Temperature dependence of quantum efficiency	0.3	0.01	200 μ	Scan
Optical interferometry	Thermal expansion, Michelson type	0.5	0.0001	0.006-0.1 μ	Scan
Near field probe (NSOM)	Use near field to improve optical resolution	0.05	0.1-1	0.1-10 μ	Scan
Built in temperature sensors	Fabricate a thermal sensor integrated into the device	100	0.0002-0.01	1 μ	No

Table 1 Summary of common experimental methods for the thermal characterization of microsystems. Adapted from [20].

Among the listed techniques, thermoreflectance imaging microscopy has been broadening during the past few years, becoming a well established thermal characterization technique due to its high spatial and thermal resolution and its ultrafast transient resolution capability. This noninvasive optical technique is based on the photo-reflectance principle [21, 22], which makes it capable of mapping three-dimensional (3D) temperature fields of surfaces and devices. The experimental procedure consists of setting the studied device under cyclic excitation by an applied pump pulse, which is normally an electrical current.

This pump excitation causes the device to increase its surface temperature, ΔT, given by

$$\Delta T = T_1 - T_0 \qquad \text{Eqn. 24}$$

where T_1 and T_0 refer to the surface temperature of the studied sample after and before excitation, respectively. Subsequently, the increase of temperature causes the device to experience in-phase changes in its surface reflectivity, $\Delta \Lambda$. This fundamental working principle including the electrical power applied to the device, the incident and in-phase reflected light intensity and the device temperature is illustrated in Figure 9.

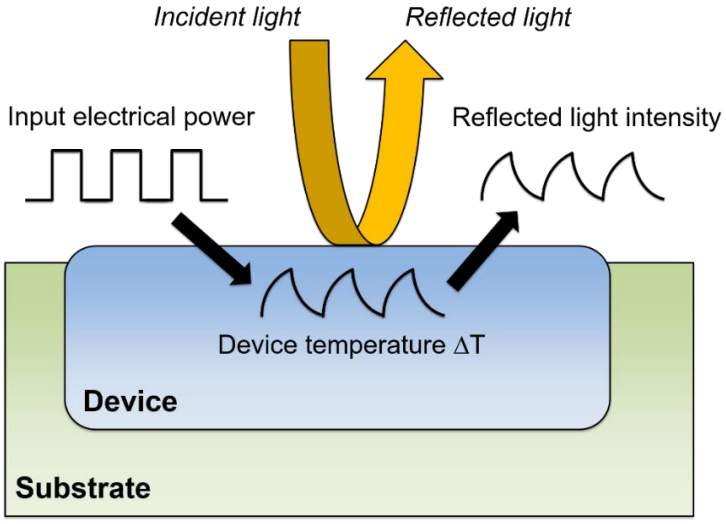

Figure 9. Diagram of the thermoreflectance imaging basic principle. Adapted from [23].

During the measurement, a monochromatic light-emitting diode (LED) probe illuminates the sample and a high signal-to-noise charge-coupled device (CCD) camera simultaneously measures the change in reflectivity of the sample surface at each pixel of the acquired image. This yields to a pixel by pixel map of the change in thermoreflectance signal within the complete field of view of a coupled microscope, which can be expressed as a 3D probe response map.

Considering Λ_0 as the intensity of the reflected light from the studied device at each recorded pixel, at a given temperature, T_0, the normalized change in surface optical reflectivity is defined by Equation 25 [23, 24].

$$\frac{\Delta \Lambda}{\Lambda_0} = \frac{1}{\Lambda_0}\frac{d\Lambda}{dT}\Delta T \qquad \text{Eqn. 25}$$

In practice, the change in thermoreflectance signal is found to be small, typically in the order of $\Delta\Lambda/\Lambda_0 = 10^{-5}K^{-1}$ to $\Delta\Lambda/\Lambda_0 = 10^{-4}K^{-1}$. It is therefore necessary to perform a "lock-in" amplification, which consists on averaging the experimentally measured change in thermoreflectance over a large number of thermal cycles at a given frequency, so that the recorded signal can be extracted from the background noise. After this process, the acquired thermoreflectance image can be transformed to a thermal map from the device surface by scaling it with the material thermoreflectance coefficient C_{TH}, obtained separately. The change in temperature of the device under study is found by Equation 26 [23]

$$\Delta T = \frac{1}{C_{TH}} \frac{\Delta\Lambda}{\Lambda_0} \qquad \text{Eqn. 26}$$

For materials under small temperature changes (<100K) the relationship between thermoreflectance change and temperature can be considered as linear.

Schematics of the required experimental set up for this technique and its main components, which are commercially available, are shown in Figure 10. Photographs of an in-house experimental set up for electrically pumped thermoreflectance imaging are shown in Figure 11.

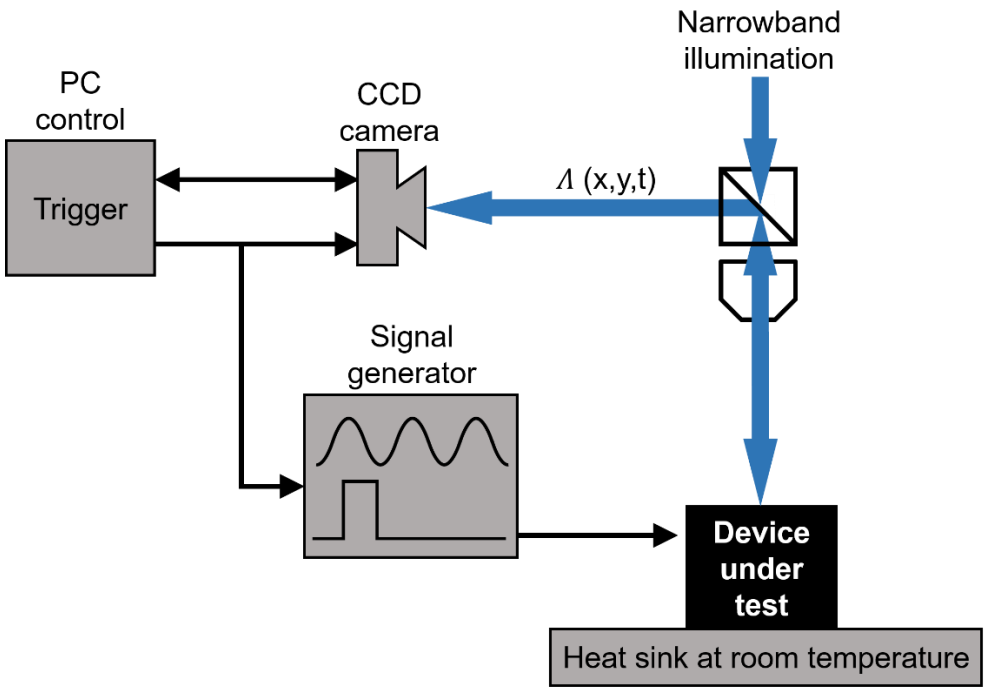

Figure 10. Schematic diagram of the thermoreflectance imaging experimental set up. Adapted from [23].

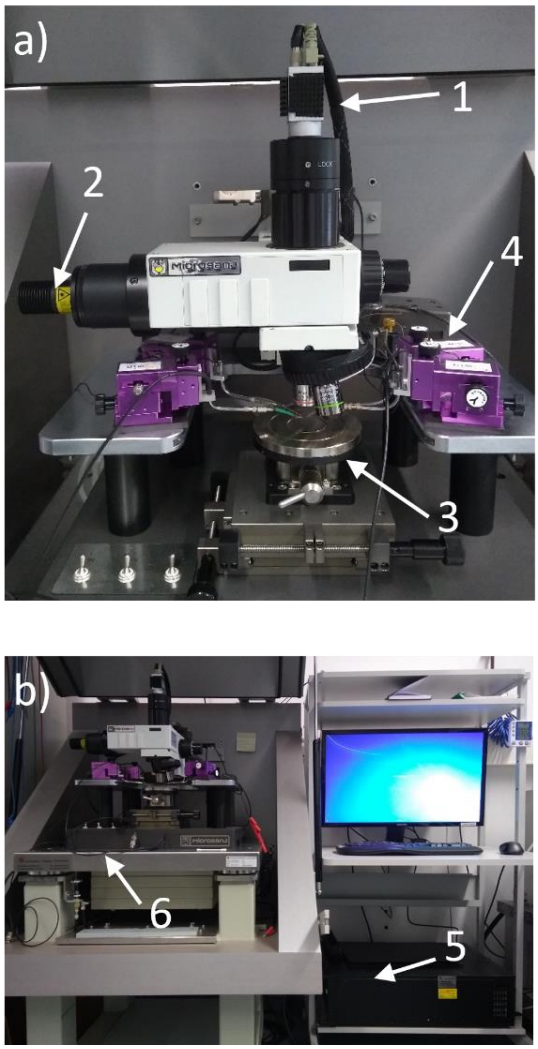

Figure 11. Experimental set up of electrically pumped thermoreflectance imaging microscopy.The main components correspond to 1) CCD Camera, 2) LED, 3) Sample stage, 4) Micro-manipulators, 5) Computer with signal generator and control software, and 6) Pneumatic table.

As shown in Figure 10, the device under test is set to cycled thermal excitation by an applied electrical pump and placed on top of a heat sink held at room temperature. This input excitation is controlled by a signal generator and triggered by a PC that contains the control software interface. The studied sample is located beneath a microscope coupled with a CCD camera and a normal incident light.

The thermoreflectance amplitude over cumulative averaging is extracted by a differential algorithm for a set lock-in frequency. The thermoreflectance imaging is achieved by a pulse measurement scheme, where the electrical device excitation and the illumination probe are low duty cycle square pulse signals.

When the square pump pulse is applied to a device under study, its surface reflectivity will change gradually until thermal steady state is reached. When the device electrical excitation is interrupted, the device reflectivity will gradually go back to its initial state, reaching thermal

balance again. Recorded data from hot and cold images are acquired by the CCD camera in alternate pulse trains, when the probe signal is on. This allows to measure the amplitude of the change in reflectance by differentiating between a hot and cold images. This technique makes it possible to take a set of cold and hot measurement with a frequency between 1 kHz and 1 MHz. Each period begins when the pump signal is activated, shown as t_0 in Figure 12.

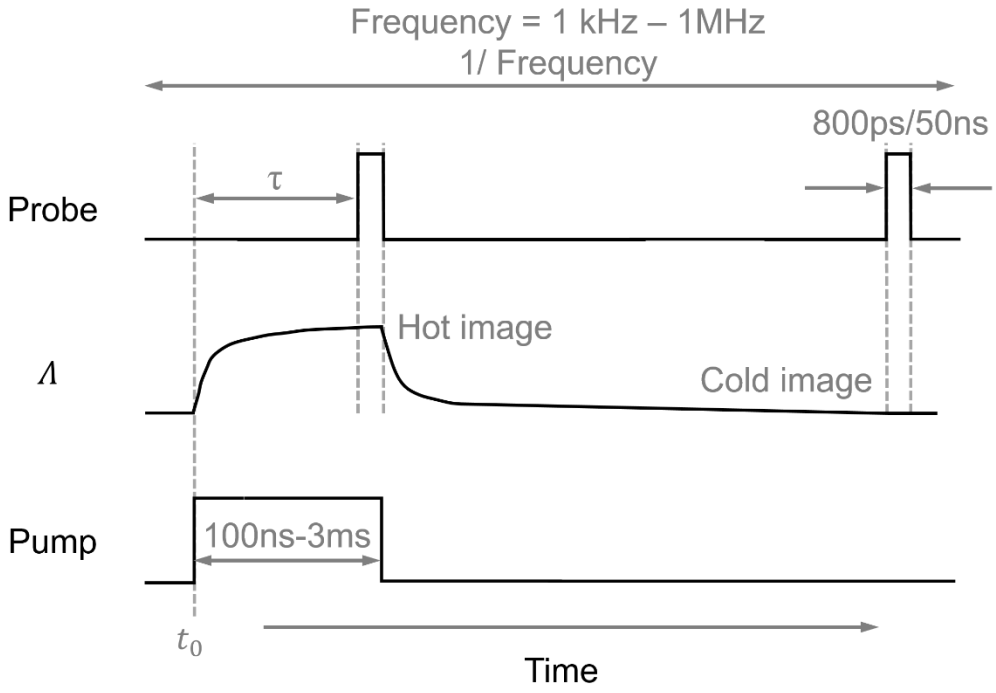

Figure 12. Diagram of the thermoreflectance imaging timing signals. The differential algorithm used to measure the change in reflectance of a studied sample. There are three elements involved; the pump pulse, the sample's surface reflectivity and the illumination probe. Adapted from [23].

The differential algorithm also allows to perform transient characterization of a studied device. If the duration of the probe signal is selected to be shorter than the pump signal and a delay of the illumination pulse, with respect to the rising edge of the device reflectivity pulse, is adjusted, the temperature change for individual time segments can be measured. The complete thermal heating and cooling transient curves can be reconstructed with a transient temporal resolution within 50 nanoseconds [23]. To do so, one must understand the transient dynamic behavior of the device under study and select carefully the image acquisition delay time with respect to the pump (τ), since the CCD camera will only record reflectance data when the probe pulse is on.

The illumination wavelength presents a very strong impact on the measured thermoreflectance amplitude. Therefore, proper selection of illumination wavelength is paramount before performing thermoreflectance image microscopy on the sample of interest. A summary of

different illumination wavelengths and their relation with thermoreflectance coefficient is depicted in Figure 13 [25].

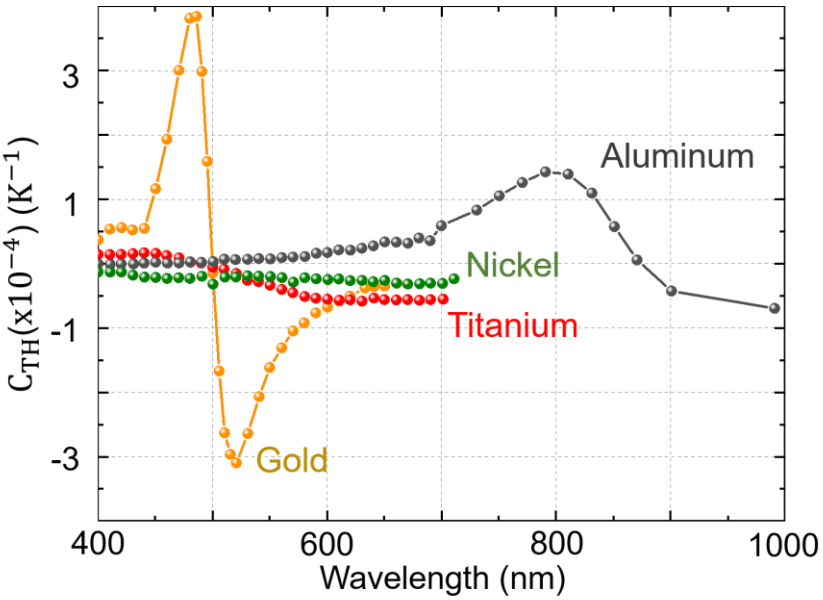

Figure 13. Relationship between thermoreflectance coefficient and illumination wavelength for Gold, Titanium, Nickel and Aluminum. Adapted from [25].

“Los empresarios no nos desanimamos a la primera. Somos como lagartijas apedreadas: sabemos correr, escondernos, defendernos y estar alerta”

„We, the entrepreneurs, are not discouraged easily. We are like stoned lizards: we know how to run, hide, defend ourselves and remain alert.“

– Lorenzo Servitje, mexican businessman and philanthropist, * 1918 † 2017 –

3 Design guidelines of micro-thermoelectric coolers

3.1 Introduction

In brief, there are three main aspects of µTECs that need to be studied separately in order to push forward their performance. These are: materials performance improvement, micro-device fabrication process development and the thermomechanical design optimization. Previous works have focused on the optimization of thermoelectric material properties [26, 27] and in the development of fabrication processes for integrated µTECs [3, 7].

Recently, the thermoelectric material and devices group at the IFW-Dresden has developed a route for the fabrication of integrated µTECs by a combination of standard photolithography and a modified ECD technique, by using bismuth tellurium (BiTe) compounds. The construction of this device involved multiple steps of photolithography and mask alignments, as shown in Figure 14. It achieved a maximum net cooling temperature of 6 K with a rapid cooling response time of 1 millisecond and demonstrate a stable cooling performance over 30 days with a reliability of more than 10 million cooling cycles [2].

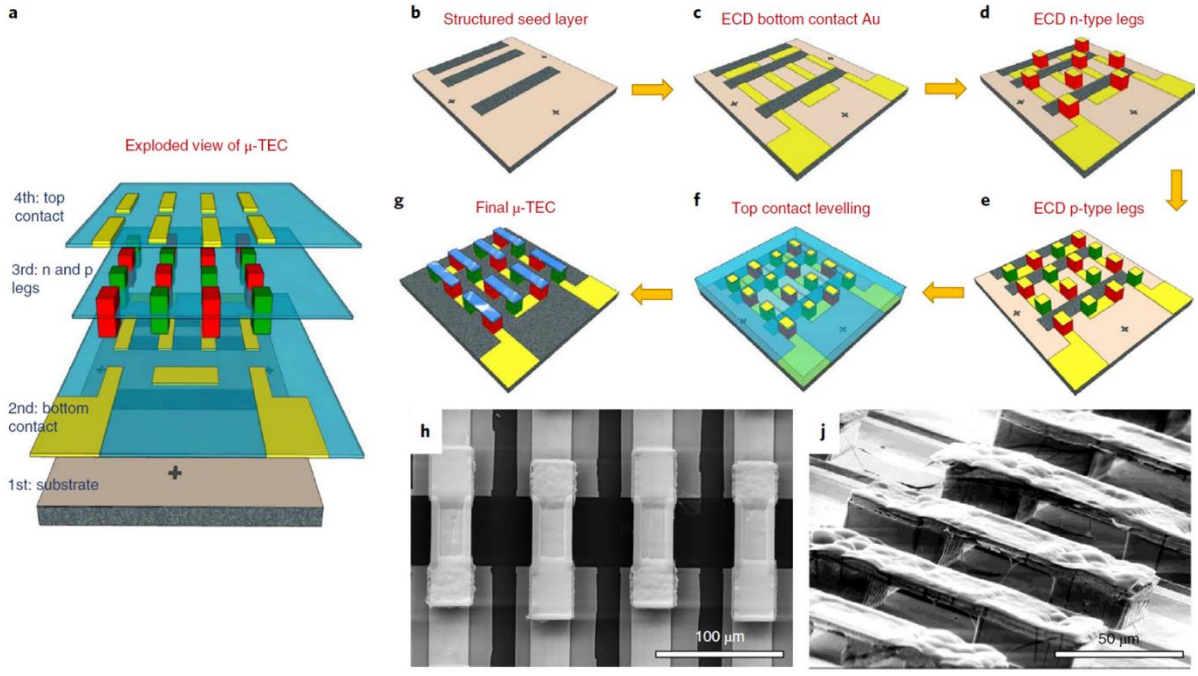

Figure 14. Schematic fabrication line for integrated µTECs and corresponding secondary electron images.a) Exploded view of an integrated µTEC with six leg pairs, demonstrating the four-layer structure. b)–g), The µTEC device is fabricated using the following steps: coating the supporting substrate with an Au seed layer (b), ECD of a 3 µm Au layer as bottom contact (c), ECD of 10 µm BiTeSe as n-type legs (d) and Te as p-type legs, followed by ECD of 1 µm Au protection on top (e), and top contact levelling by partially exposing thick photoresist (f), resulting in the final µTEC device (g). Top (h) and side (j) scanning electron microscopy views of the as-fabricated µTEC device. Published in [2].

On the other hand, in addition to the material properties and deposition techniques optimization, equally important for the performance improvement of μTECs is thermomechanical design optimization. Several works have demonstrated that substantial enhancement of the performance of a thermoelectric device can be achieved by optimizing its geometrical design, independently of the considered thermoelectric material [28-33]. However, these works have focused mainly on macro scale devices, leaving in-depth studies of μTECs largely unexplored.

As the size of a TEC is reduced, the detrimental impact that key parameters present during the device construction becomes increasingly relevant, which yields to substantial differences between the performances of TEC at the macro- and micro-scale. This includes the micro- structuring and material deposition technologies, which constrain the geometry definition of the μTEC under construction. Likewise, the deposition of materials at the micro- scale typically leads to significant deterioration of their properties with respect to their bulk values [7]. In addition, it is typically challenging to control the surface roughness of the materials during deposition process, which leads to the increment of the electrical contact resistances between deposited materials. This causes the increase of internal resistance of the device, which decreases its overall performance [4, 5].

Rather than optimizing the design of a μTEC for a specific application, this chapter systematically analyzes the trend effect that key parameters involved in the design and fabrication of μTECs present on the overall device performance. The aim is to formulate a comprehensive design guide to optimize the construction of next generation micrometer-sized thermal management thermoelectric devices. At the end of the chapter, experimental data obtained by thermoreflectance image microscopy of a μTEC is correlated to a finite element model, in order to estimate the thermal conductivity of the thermoelectric materials and the electrical contact resistance of the device.

3.2 Micro-thermoelectric coolers: an alternative for thermal management

Since the middle of 1960's, Gordon Moore predicted that, driven by a constant development of manufacturing processes, the reduction of component size would boost the number of components within integrated electronics, allowing them to double every 12 months [34]. This continual miniaturization tendency has dramatically increased the functionality of densely packed micro-electronics and photonic systems [4]. On the other hand, this has also carried a severe increase of localized heat fluxes, typically known as "hot spots". Hot spots are a technological challenge, since they lead to premature fatigue of components, with subsequent reduction of their reliability and increase of component failure.

For this reason, the development of efficient thermal management technologies capable to remediate this burden has been receiving increasing attention. Different research groups have consummated relevant contributions on the development of cooling technologies, such as single-phase and two-phase convective microchannel heat sinks [35, 36], air jet impingement cooling [37], spray cooling [38], and thermoelectric coolers at the macro- and micro-scale [3, 5, 39].

Among these technologies, solid state micro-cooling devices, based on the Peltier effect, present unique attributes that made them an attractive technology, despite their high cost and low energy efficiency. They can convert electricity directly into temperature differences, without moving parts; which makes them not only light weight, but also operation noise and maintenance free. Likewise, they can offer high accuracy and fast response, which makes them particularly suitable for precise dynamic temperature control.

Important achievements have been previously reported, such as the successful integration of μTECs at the package level [39]. It has been demonstrated their applicability for temperature stabilization of telecommunication laser diodes [6, 7], as well as on-chip hot spot remediation. Thereby, localized cooling of target heat fluxes between 600 and 1300 W cm^{-2} have been achieved [32, 39, 40]. In addition, it has been suggested that their performance can be improved by coupling additional cooling stages [4].

Several technologies have been proposed for the manufacturing of μTECs, including electrodeposition [3, 41], sintering [42], and combination of thin film and micro-systems technology [43]. Among the aforesaid processes, ECD presents several attributes that make it particularly advantageous. ECD of materials and contacts is the standard back-end-of-line (BEOL) process for integrated circuits in complementary metal-oxide semiconductor (CMOS) technologies, which makes it compatible with microelectromechanical system (MEMS) technology and allows on-chip integration [44]. Furthermore, it is relative low-cost and allows adjustable material compositions through modification of the electrolyte. It can be operated at ambient condition with large scalability and a high material deposition rate, which enables thick-film deposition of up to tens of micrometres [26, 27].

3.3 Analysis approach

In order to systematically study the impact that individual factors present on the performance of a µTEC, a single leg pair thermoelectric device was chosen. The thermoelectric materials were defined as electrochemically deposited $(Bi_xSb_{1-x})_2Te_3$ (p-type) and $Bi_2(Te_xSe_{1-x})_3$ (n-type), the top contact material was defined as Nickel, the bottom contact material was defined as Gold, and the substrate material was defined as Silicon. This baseline geometry is shown in Figure 15, and the detailed values used for the geometrical dimensions, electrical, thermal, and thermoelectric material properties are found in Table 2.

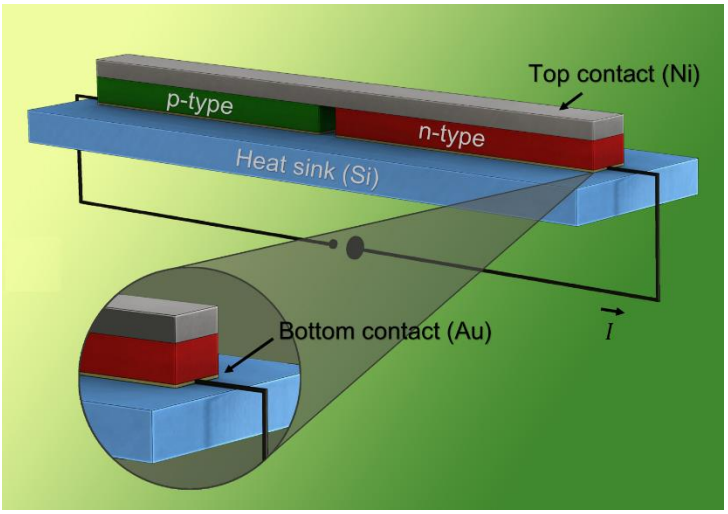

Figure 15. Schematic diagram of a single leg pair µTEC. This baseline geometry includes following sections: Silicon substrate (blue), Gold bottom contact (yellow), p-type semiconductor (green), n-type semiconductor (red) and top Nickel contact (gray). Published in [45]

Material	Section	Dimension [width×length×height] [µm x µm x µm]	Electrical conductivity [S cm^{-1}]	Seebeck coefficient [µV K^{-1}]	Thermal conductivity [W m^{-1} K^{-1}]
$Bi_2(Te_xSe_{1-x})_3$	n-type	140x20x12	950	-55	1.2
$(Bi_xSb_{1-x})_2Te_3$	p-type	140x20x12	1800	55	1.1
Nickel	Top contact	290x20x8	138000	-15	150
Gold	Bottom contact	140x20x1	456000	6.5	317
Silicon	Substrate	390x118x500	Electrically isolated	Electrically isolated	130

Table 2. Summary of device components baseline geometry for µTEC performance study. Thermoelectric material properties were measured from in-house electrochemical deposited continuous films. Published in [45].

A FEM based on the baseline geometry and material properties previously introduced was constructed in COMSOL Multiphysics, using the coupled heat transfer and electric current modules. In this manner, it was possible to vary individual design parameters of each of the involved sections and numerically analyze their impact on the device performance. As boundary conditions, an electrical current was applied to the μTEC, as shown in Figure 8, and the temperature at the bottom of the substrate was constrained at 300 K. All of the components were considered to be thermally contacted and the heat sink to be electrically isolated from the μTEC device. All the thermal contact resistances at the interface between different sections were neglected. The electrical contact resistance between the thermoelectric legs and the metallic contacts was constrained at a value of $r_c = 5\ x\ 10^{-11} \Omega m^2$, in accordance with previous works [6]. All other electrical or thermal losses were neglected.

For the results shown in this chapter, ΔT is defined as the temperature difference between the average temperature of the upper surface of the top contact and the bottom of the substrate, which in the studied case was constrained at 300 K.

3.3.1 Input current optimization

As a first step, the relationship between I and ΔT was studied for the baseline geometry. The results are summarized in Figure 16. A maximum ΔT, of around 4K, was achieved when I presented a value between 100 and 150 mA.

Hence, in order to be close to the optimal input current, I was fixed at 100 mA for the following FEM performed in this study. As shown in the insert from Figure 16, an inherently asymmetric temperature distribution along the device was predicted. This is caused by the asymmetric electrical resistivity values of the p- and n-type thermoelectric materials and subsequent asymmetric joule heating generated within the thermoelectric legs.

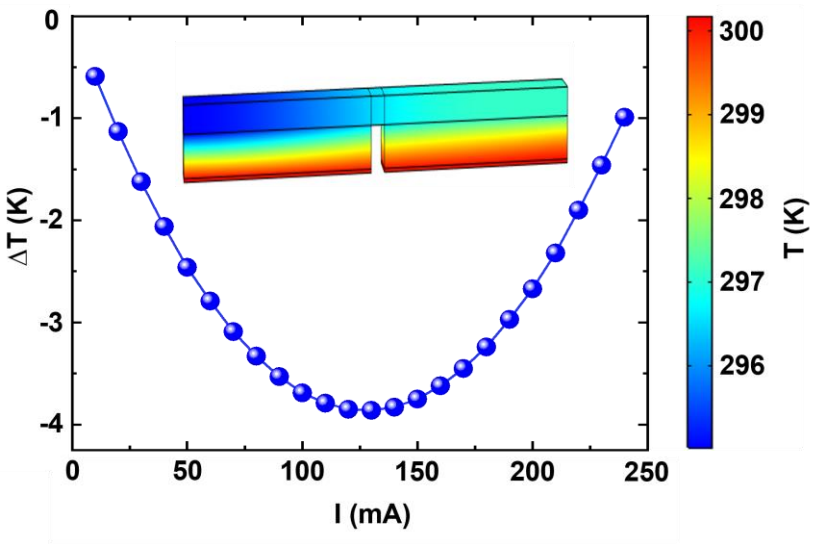

Figure 16. Simulation results of the impact that I presents on ΔT for baseline geometry. The insert shows the temperature distribution observed when a I of 100mA is applied. The insert depicts the obtained temperature distribution along the device. Published in [45]

3.3.2 Metallic contacts

Next, considering *I* fixed at 100mA, the impact that the bottom and top contact thickness represent on the μTEC performance was studied. In Figure 17 (a), (b), (c) and (d) diagrams of the thinnest and thickest bottom contact (BCT) and top contact (TCT) geometrical variations studied are shown.

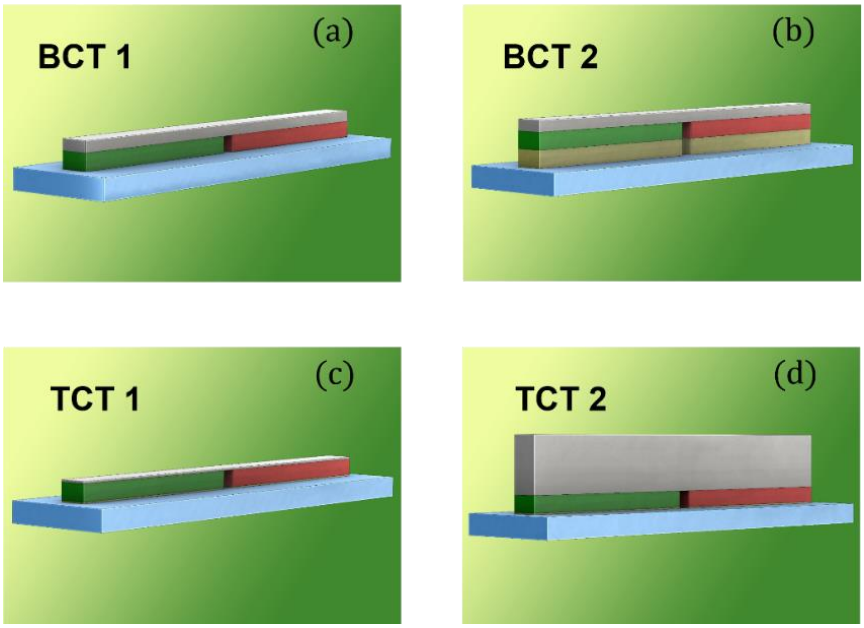

Figure 17. Schematic diagram of the initial and final data points for the metallic contact analysis of a μTEC. (a) The acronyms refer to the thinnest bottom contact (BCT 1), (b) the thickest bottom contact (BCT 2), (c) the thinnest top contact (TCT 1) and (d) thickest top contact (TCT 2). Published in [45].

The dependency between the total electrical resistance of the μTEC, *R*, and ΔT with respect to both BCT and TCT is summarized in Figure 18. It can be observed that *R* tends to decrease as the thickness of the top and bottom contacts increase, driven by an increment of the contacts' cross section area and subsequent reduction of their electrical resistance.

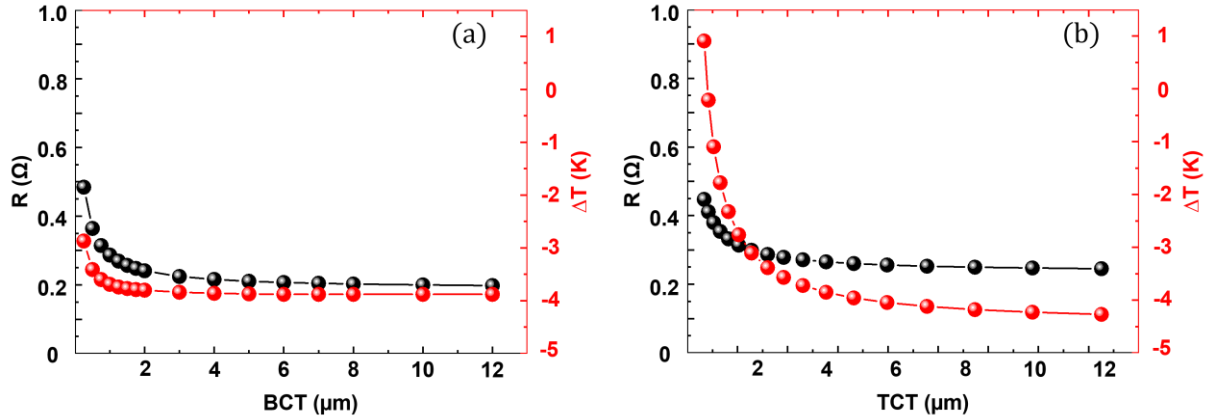

Figure 18. Relationship between metallic contact thickness, ΔT and R. The results summarized the evolution R (black) and ΔT (red) of the BCT (a) and TCT (b) as the contact thickness increases and both I and thermoelectric legs geometry are fixed. Published in [45].

It can be concluded that in both cases, the reduction of R helps to achieve a larger ΔT, due to the consequent reduction of the $\dot{Q}_{Joule}$. However, the impact of TCT variation on ΔT is more severe than its counterpart BCT, which leads to a more pronounced slope of the ΔT dependency of R, as shown in Figure 19.

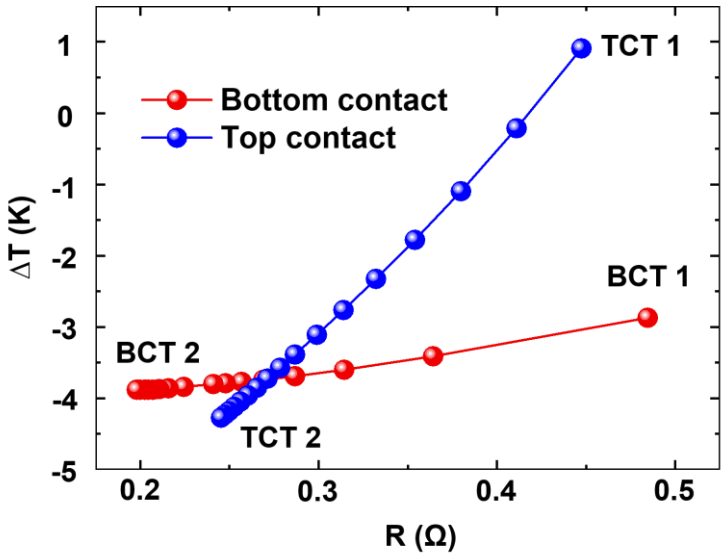

Figure 19. Relationship between ΔT and R for the baseline μTEC as a result of the metallic contacts thickness variation. The data in blue refers to the TCT and the data in red to the BCT. Published in [45].

Furthermore, Figure 18 suggests that for the particular case of the top contact, higher values of ΔT are reached as TCT is thicker than 10 μm, despite no significant reduction in R is observed. This provides an insight of the top contact role within the performance of μTECs, since it is not only an electrical but also a thermal bridge that additionally enhances the heat spreading at the cold side junction, as shown in Figure 20.

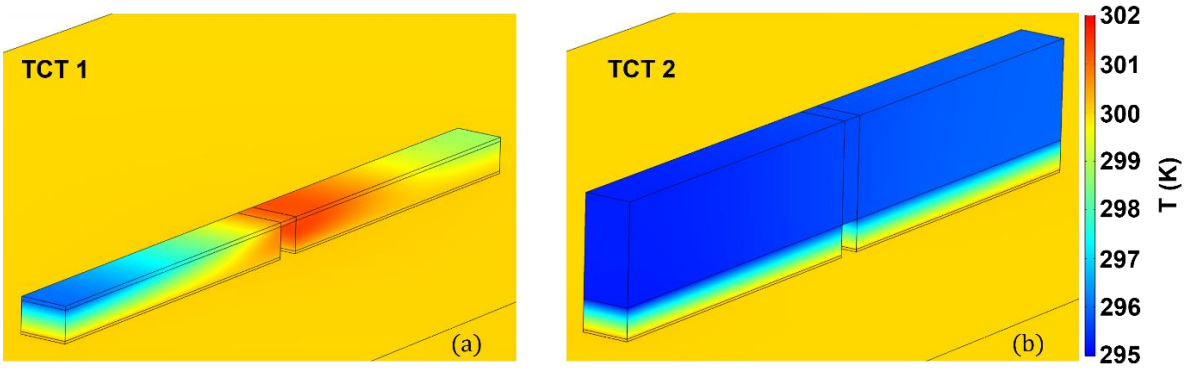

Figure 20. Variation of the temperature distribution as a result of the TCT variations. Temperature distribution obtained at studied device data points TCT 1 (a) and TCT 2(b). Published in [45].

It was also found that the thickness of the metallic contacts not only influences the calculated value of *R*, but also the distribution of the electrical current lines within the thermoelectric material. This can be clearly observed in Figure 21, where the current line distributions for the of the data points BCT1 and BCT2 are shown. In the case of a thin bottom contact, the current lines appear to be more densely packed at one side of the thermoelectric leg and run tilted to its sides. In the case of a thick BCT, a more even distribution of the current lines within the thermoelectric material is achieved and they run parallel across the thermoelectric leg.

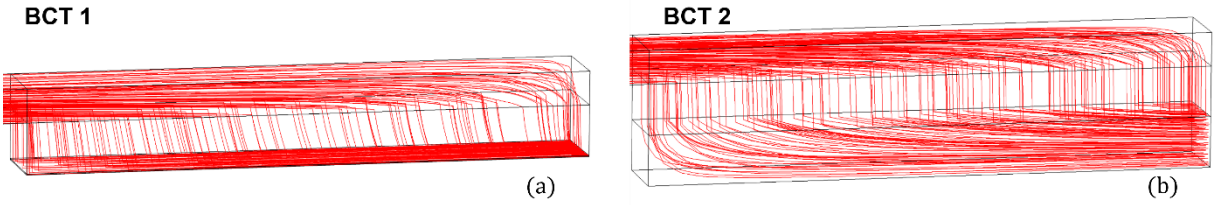

Figure 21. Dependency of the electrical field lines distribution as a result of BCT variations. The results obtained for data points BCT 1 (a) and BCT2 (b). Published in [45].

These results prove that, if the thickness for the metallic contacts is not properly dimensioned, a plausible detrimental effect on the device performance can be induced. From a practical stand point, it can be concluded that µTECs require that the thickness of the metallic contacts present a comparable size to the active thermoelectric elements. This findings clearly contrast with traditional design approaches for macro TECs, where the influence of the electric contacts is commonly neglected.

3.3.3 Leg pair geometry

The impact that geometrical variations of the thermoelectric elements present on the performance of the device was studied. The geometry of the n- and p-type thermoelectric materials at the X, Y and Z coordinates was individually varied, while taking the baseline model as a starting point. Diagrams corresponding to the initial and final geometries of the thermoelectric elements are depicted in Figure 22. The variation of thermoelectric leg width (W_{tec}) is labeled as (W1, W2), the one of the thermoelectric leg depth (D_{tec}) as (D1, D2) and the one of the thermoelectric leg height (H_{tec}) as (H1, H2).

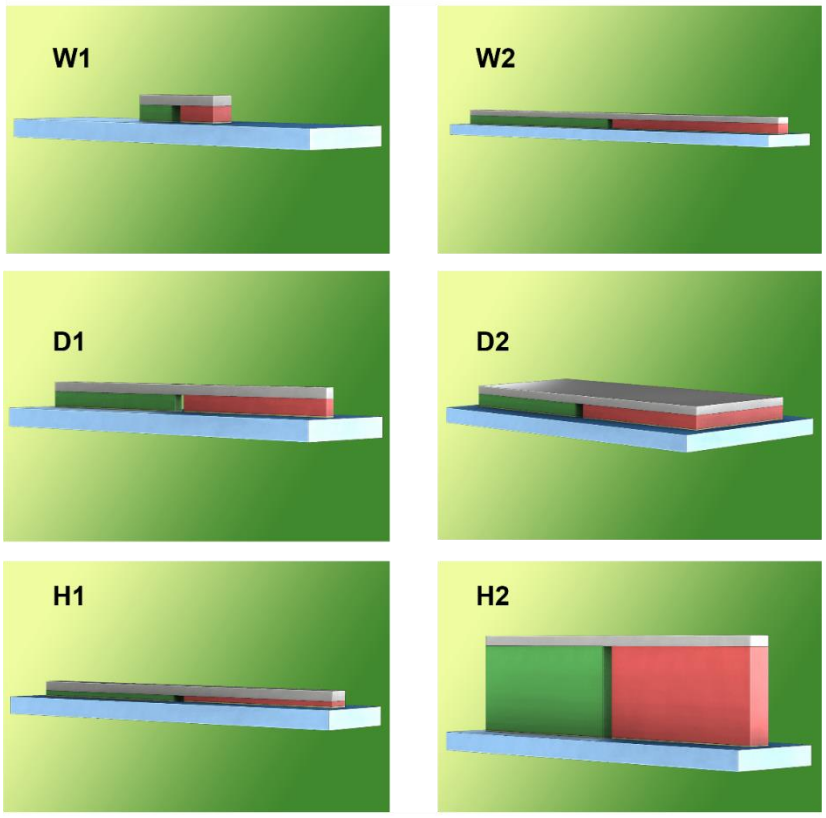

Figure 22. Schematic diagrams of the geometry variations for the thermoelectric leg geometry. The smallest and largest corresponding parameter of the data points W1, W2, D1, D2, H1 and H2 are shown. Published in [45].

The interplay between $\dot{Q}_{Peltier}$, $\dot{Q}_{Fourier}$, $\dot{Q}_{Joule}$ and $\dot{Q}_C$ and the values of ΔT and COP, as a result of independent modification of W_{tec}, D_{tec} and H_{tec}, were computed as the geometry was modified. In addition, it should be noted that $\dot{Q}_{Joule}$ comprises the contribution of the entire device. This includes the effect of the interface resistances as well as the resistance of the contact materials and thermoelectric elements. The results are summarized in Figure 23.

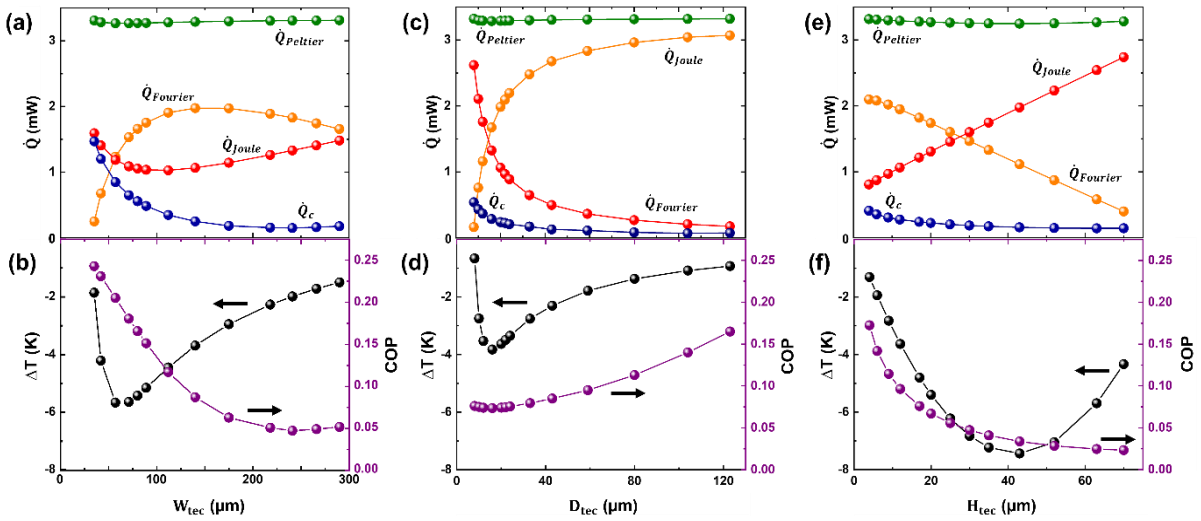

Figure 23. Interrelation of heat fluxes and resulting ΔT and COP for geometry variations of the thermoelectric legs.The interplay of the individual heat fluxes $\dot{Q}_{Peltier}$, $\dot{Q}_{Fourier}$, $\dot{Q}_{Joule}$ and $\dot{Q}_C$ and the parameters ΔT and COP are summarized as a function of independent variations of W_{tec} (a, b), D_{tec} (c, d) and H_{tec} (e, f). Published in [45].

These results show that for the case studies of ΔT as a function of W_{tec} and D_{tec} a clear asymmetry can be observed, as depicted in Figure 23 b) and d). This is due to the fact that variations of these two parameters also modify the contribution that the metallic contacts present on $\dot{Q}_{Joule}$. Furthermore, to understand the very different response of ΔT as during increments of W_{tec}, and D_{tec}, it should be noted that the thermoelectric legs of the µTEC under analysis present a rectangular geometry. Hence, individual increments of W_{tec} and D_{tec} of the leg pair carry dissimilar increment rates of the normal area of the p- and n-type thermoelectric legs. This factor defines whether $\dot{Q}_{Fourier}$ or $\dot{Q}_{Joule}$ is the dominating mechanism in each of the examined cases, as depicted in Figure 16 a) and c).

Additionally, it was found that variations of H_{tec} revert to linear changes in $\dot{Q}_{Fourier}$ and $\dot{Q}_{Joule}$, as seen in Figure 23 e). It can be concluded that H_{tec} is the parameter that presents the largest impact on ΔT, as shown in Figure 23 f). However, in practical terms this is not a free factor, since it is constrained due to fabrication factors, such as the choice of photoresist and the maximum possible deposited thickness of the material film.

It can be observed from Figure 23 b) and f) that variations of W_{tec} and H_{tec} yield to changes in COP that qualitatively follow the trend of $\dot{Q}_C$. The increase of W_{tec} and H_{tec} reverts to a decrease of COP, as a result of the increments of $\dot{Q}_{Joule}$. In contrast, progressive increments of D_{tec} revert to a reduction of the electrical resistance of the device and subsequently $\dot{Q}_{Joule}$, which ultimately yields to an increase of COP, as depicted in Figure 23 c) and d).

For all cases, it was also found that a maximum ΔT was achieved close to the point where $\dot{Q}_{Joule}$ compensates for $\dot{Q}_{Fourier}$, as summarized in Figure 24, where ΔT is expressed as a function of the balance between $\dot{Q}_{Joule}$ and $\dot{Q}_{Fourier}$. The reason why these curves are not completely

symmetric is due to the dissimilar thermoelectric material properties considered for the studied legs. Nevertheless, the case of W_{tec} presents a particularly asymmetric condition, which is the result of the increment of the contribution that the metallic contacts present on $\dot{Q}_{Joule}$, driven by the enlargement of W_{tec}. This asymmetry also suggest that under realistic micro-device construction, assuming an equal amount of joule heating contributing to the cold and the hot side of the device is not accurate.

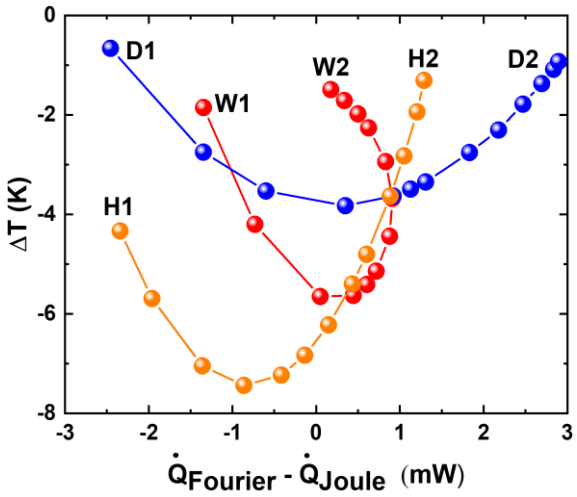

Figure 24. ΔT as a result of the heat flux balance between $\dot{Q}_{Fourier}$ and $\dot{Q}_{Joule}$, resulting from the geometry variation of W_{tec} (curve W1-W2), D_{tec} (curve D1-D2), and D_{tec} (curve H1-H2). Published in [45].

These results provide an insight on the internal electric and heat fluxes occurring within the µTEC under operation. They can be applied to any real application of µTEC design as guidelines for the compromises that need to be made.

3.3.4 Fill factor

For the analysis shown in the previous section, the single µTEC leg pair under study was deposited on a substrate with an area much larger than the n- and p-type thermoelectric legs. Therefore, this substrate allowed effective heat dissipation at the µTEC hot side, which made the impact of any detrimental effects that could arise by the distance between adjacent thermoelectric elements negligible. However, practical applications of µTECs require to construct arrays of several µTEC devices with large packing densities, which are necessarily thermally connected in series to the substrate. This situation means that the heat flux balance in Equation 9 cannot be treated as an isolated system, since the term $\dot{Q}_{Fourier}$ of each µTEC will be influenced by adjacent µTEC devices. For this reason, it is paramount to undertake a study regarding the effect that the µTEC thermoelectric leg fill factor (*FF*) presents on the device performance. *FF* is defined as the ratio between the cross sectional area of the active thermoelectric legs and the total substrate area. It follows from the previous explanation that *FF* is a parameter that must be assessed in order to optimize the number of active µTECs constructed without affecting the overall performance of the device. This is crucial for practical applications, where hundreds of µTECs may be deposited in the same substrate.

The relevance of *FF* in a real scenario is illustrated in Figure 25, where in-house constructed integrated µTECs consisting of 220 leg pairs were deposited within a 2x2mm² substrate area, with a resulting packing density of 5,500 leg pairs per cm ² and a *FF* around 0.20 [2].

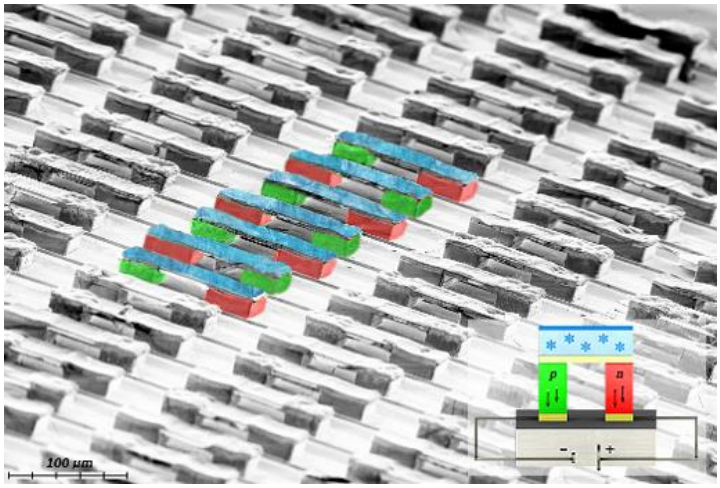

Figure 25. Scanning electron microscopy of an array of µTECs constructed by ECD. Published in [2].The insert exemplary shows the architecture of a single leg pair µTEC and the describes the colors used for the p- type (green), n-type (red), the metallic contacts (yellow) and the cold side junction (blue). Credits for the insert and image coloring to Ronald Uhlemann.

In order to highlight the impact of *FF* on this study and neglect any asymmetric heat fluxes that might arise due to dissimilar thermoelectric material properties, the geometry of the thermoelectric legs was adjusted. To ensure that the product $(K_p+K_n)(R_p+R_n)$ is as small as possible and that $\dot{Q}_{Fourier}$ is even across both legs, as proposed by [11], the geometry of the two legs was adapted to satisfy Equation 27

$$\frac{H_{tec-n}\ A_p}{H_{tec-p}\ A_n} = \sqrt{\frac{\rho_p \lambda_n}{\rho_n \lambda_p}} \qquad \text{Eqn. 27}$$

where A_p and A_n refer to the normal area of the p- and n-type thermoelectric materials, respectively. With this considerations, the geometry of the thermoelectric legs were fixed at 30x30x12 μm³ for the p-type and 40x30x12 μm³ for the n-type. A parametric study was undertaken in order to find out the optimal input current that leads to the maximum ΔT, which was found to be around 70 mA. This value was fixed for the following analysis in this section.

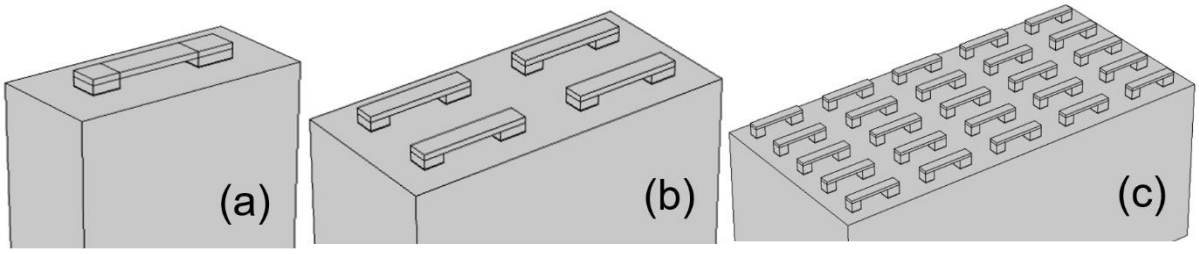

Figure 26. Schematic diagram of the study cases for the *FF* analysis for a single leg pair (a), four leg pair array (b) and twenty-five leg pair array (c).

The impact that *FF* presents on ΔT was evaluated for three different arrays of μTECs: a) a single leg pair, b) a four leg pair array and c) a 25 leg pair array. Schematics of the studied cases are shown in Figure 26. *FF* was analyzed by varying the distance between thermoelectric elements and the substrate area in each of the three study cases, in order to accommodate the studied array of μTECs. Simulation results are summarized in in Figure 27.

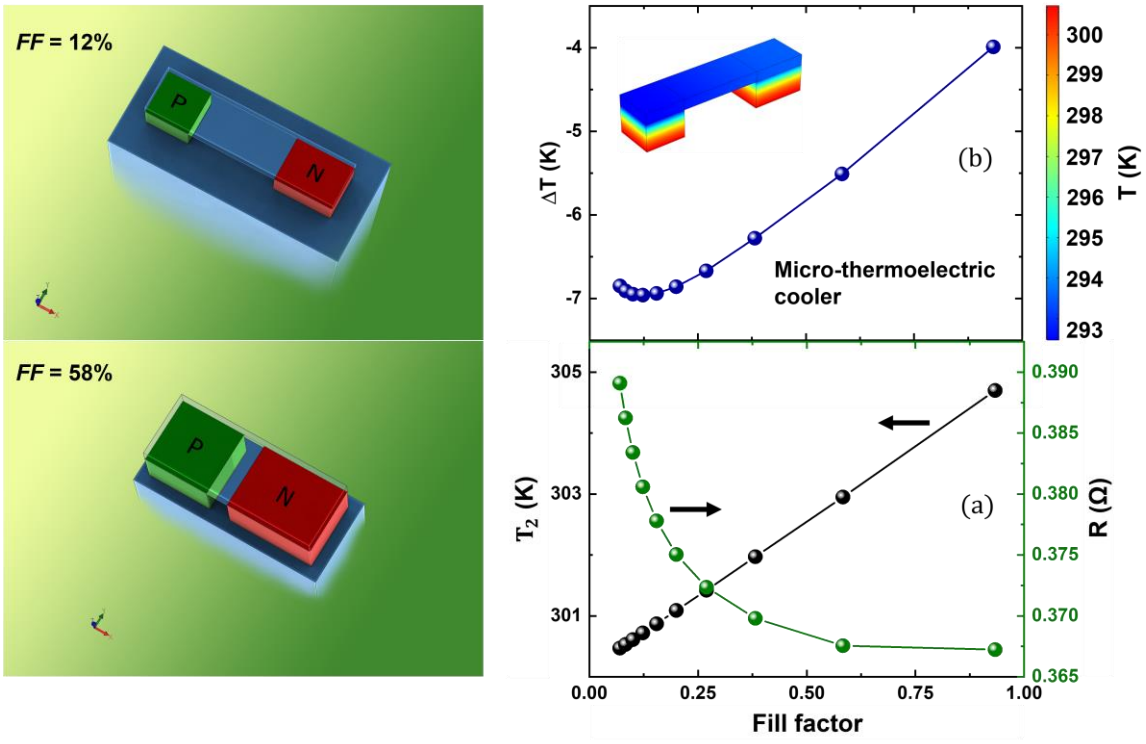

Figure 27. Dependency of ΔT, T_2 and R as a result of FF variation. Schematics diagram for the cases of FF=12% and FF=58% (left). Summary of numerically calculated results a) and b). The insert in b) depicts the temperature distribution calculated for the case of FF=12%. Published in [45].

Simulation results suggest that the increment of FF impacts the performance of the µTEC array in two different aspects. On the one hand, as FF increases, the distance between the thermoelectric elements is reduced. Consequently, a decrement of the electrical resistance of the top metallic bridge and the generated $\dot{Q}_{Joule}$ of the overall device can be observed, as shown in Figure 27 a). On the other hand, the temperature at the bottom of the thermoelectric element (T_2) increases linearly as the FF is increased, as shown in Figure 27 a). This is a consequence of the severe reduction of the heat sink area, which directly affects the finite thermal conductance of the substrate and its capacity to effectively dissipate the heat expelled by the thermoelectric elements at T_2. As a result of these two mechanisms, the maximum ΔT was found to be around a FF of 12 %, as depicted in Figure 27 b). When FF is raised further than this value, the increase of temperature T_2 becomes the dominating detrimental mechanism, which leaves to a lower ΔT, despite the reduction of the generated $\dot{Q}_{Joule}$.

These results contrasts with the FF values found within macro-scale TECs, since optimized commercial Bi_2Te_3 devices are typically fabricated with FF values of roughly 25.6 % [46]. Furthermore, identical results were observed for the cases of one, four and 25 leg pairs, which suggest that the system behaves symmetrically and hence the observed behavior is independent of the number of leg pairs considered.

3.3.5 Experimental characterization of µTECs

There are different commercially available techniques suitable to characterize the thermoelectric properties of bulk materials. However, this task becomes challenging for materials synthesized by ECD and deposited as thin and thick films. For the particular case of the thermal conductivity characterization of such materials, the experimental measurement procedure is not straight forward and a direct measurement is not feasible, since the thermoelectric material under analysis is thermally connected to the conductive seed layer and the substrate materials that are required for the material deposition [47].

For this reason, a study was undertaken in order to experimentally estimate the thermal conductivity properties of the thermoelectric leg pairs of an in-house constructed integrated µTEC device. Thereby, a correlation study was performed between experimentally obtained data from an in-house built µTEC and FEM. The dependency of ΔT with respect of input I of the device was experimentally measured and these data were used as a reference for the calibration of boundary parameters in the FEM. In particular, the objective of this study was to estimate the value of the thermal conductivity for the p- and n-type thermoelectric materials as well as the electrical contact resistance between the thermoelectric legs and the metallic contacts.

The in-house manufactured µTEC presented the material properties and geometry definition detailed in Table 3. All material properties considered for this analysis were defined as isotropic. Details of the manufacturing process can be found in [2]. Credits for the fabrication of the µTEC to Adytia Dutt, IFW-Dresden.

Material	Section	Dimension [width×length×height] [µm x µm x µm]	Electrical conductivity [S cm^{-1}]	Seebeck coefficient [µV K^{-1}]	Thermal conductivity [W m^{-1} K^{-1}]
BiTeSe	n-type	30x30x12	1000	-80	*
Tellurium	p-type	85x30x12	120	234	*
Gold	Top contact	75x30x8	456000	6.5	317
Gold	Bottom contact p-type	30x30x1	456000	6.5	317
Gold	Bottom contact n-type	40x30x1	456000	6.5	317
Silicon	Substrate	390x118x500	Electrically isolated	Electrically isolated	130

Table 3 Geometry and material properties of the experimentally characterized µTEC for *FF* analysis. The material properties correspond to previously reported values [2].

The experimental characterization of the device was performed via thermoreflectance imaging microscopy. Thereby, the relationship between achieved ΔT as a function of I on steady state was independently measured on top of the p- and n-type thermoelectric legs and on the top contact, as summarized in Figure 28. As shown in Figure 28 a), the recorded signal and the amplitude of its error bars vary considerably among the p-type, n-type and metallic top bridge. This variations are a result of the differences in the roughness of the electrodeposited materials. Hence, in order to obtain effective values of the thermoreflectance signal, independently measured signals of each of the aforementioned segments of the device were averaged.

A FEM was built in COMSOL Multiphysics, considering the material properties and geometry described in Table 3. In the FEM the effective thermal conductivity of the p- and n-type thermoelectric materials, $\lambda_{effective}$, as well as the value of r_c were parametrically varied to obtain the best fitting parameters to the experimental data. Results are summarized in Figure 28.

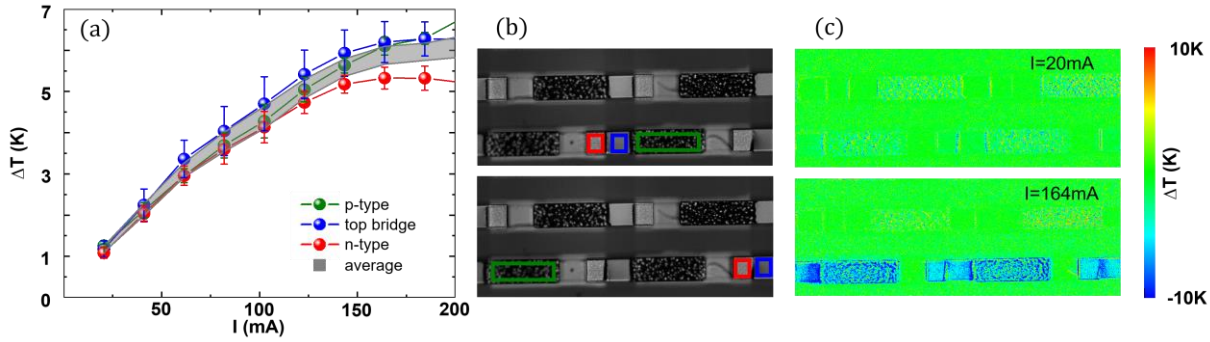

Figure 28. Thermal imaging characterization of µTEC device. (a) Summary of the independently measured ΔT on top of the p- type (green), n-type (red) and top bridge (blue) as a function of I. (b) CCD image of the characterized thermoelectric elements. Two different areas of each segment were considered for the characterization, as marked with color boxes; the green box corresponds to the p-type, the red box to the n-type and the blue box to the metallic top bridge. (c) Thermal imaging corresponding to I = 20mA and I =164 mA. The device was fabricated and the experimental measurements were taken by Adytia Dutt, IFW-Dresden.

The analysis shows that the experimental data can be well reproduced by the FEM when $\lambda_{effective}$ is between 3 and 4 $Wm^{-1}K^{-1}$. Depending of the aforementioned parameter, the value of r_c that provides the best fit varies between $1x10^{-11}$ and $8x10^{-11}$ Ω m², which is in good agreement with previous works [5, 6]. This confirms that the analysis approach and boundary conditions used for the analysis of the µTECs performance previously shown are adequate. However, a more detailed study is required in order to individually examine the thermal conductivity of the p- and n-type thermoelectric materials, for which expanding this analysis on single leg µTECs is suggested.

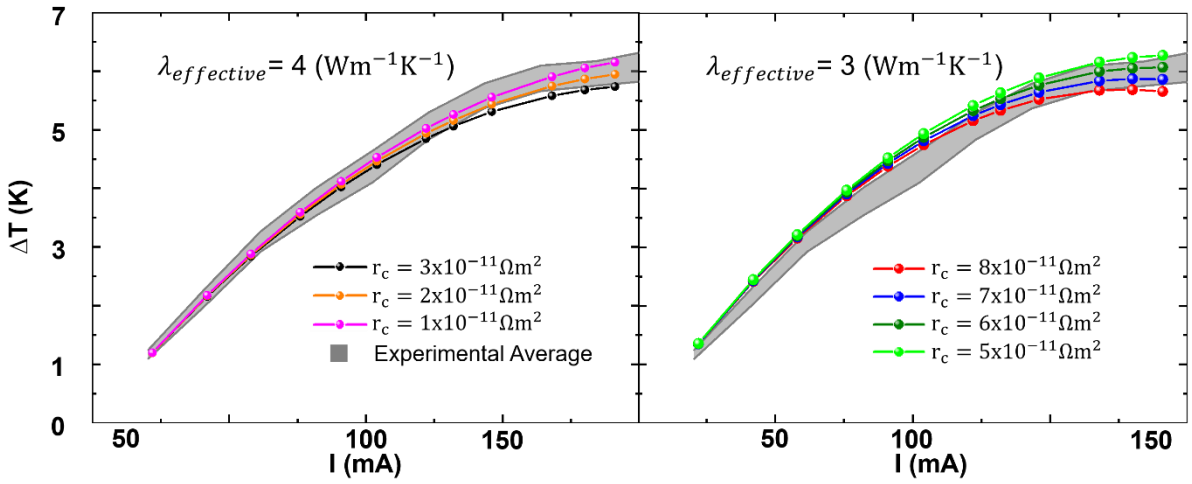

Figure 29. Correlation between the numerically and experimentally obtained ΔT. Two cases were considered, the first one for $\lambda_{effective}$ = 4 $Wm^{-1}K^{-1}$ (left) and the second for $\lambda_{effective}$ = 3 $Wm^{-1}K^{-1}$ (right).

3.4 Summary

In this chapter the impact that key parameters present on the performance of μTECs was systematically studied, considering realistic material properties, analysis assumptions, and device dimensions. This analysis demonstrated that in the micrometer range, the net electrical and thermal resistances of p- and n-type materials are of comparable magnitude to that of the top and bottom contacts. This clearly contrasts with the case of macro-TECs, where the electrical and thermal resistances of the metallic contacts are much lower than those of the thermoelectric legs and therefore neglected from the design analysis. It was found that a poor design of the metallic contacts negatively affects the current and temperature field distributions throughout the device, which subsequently decreases the device performance. The thickness of the metallic contacts enable an overall reduction of the internal resistance of the device, which reduces losses due to Joule heating. Furthermore, the metallic top contacts enhance the heat spreading ability at the cold junction, which further increments the device performance.

It was shown that the performance of a μTEC can be optimized by allowing a mutual balance of the Joule heating and Fourier heat conduction across the device, which can be achieved by properly selecting the geometry of the thermoelectric legs.

The optimal performance of the μTEC analyzed was found when a *FF* of 12 % was considered, which is a lower value than typical designs in optimized macro-sized TECs. This value was found to be independent of the number of leg pairs studied, which suggest that the system behaves symmetrically.

The analysis was complemented with a correlation study between simulation results and experimentally obtained values of the performance operation of a μTEC. This allowed us to extract key parameters of the thermoelectric device and estimate the discrepancies between simulation results and the operation of a real device.

In summary, these results highlight the impact that key parameters present on the design of μTECs. There are several factors that need to be considered for practical microstructuring and deposition of micro-devices. These manufacture limitations constrain, in many cases, the selection of geometry or materials to be used in the construction of a μTEC. Hence, trade-offs are typically required, for which the results and main conclusions shown in this chapter are a useful tool. They provide guidelines for understanding how a combination of factors may impact the performance of the device under analysis.

“Todo momento es bueno para aquellos que saben cómo trabajar y tienen las herramientas para hacerlo.”

“Every moment is favorable for those who know how to work and have the tools to do it.”

– Carlos Slim Helú, mexican entrepreneur and philanthropist, * 1940 –

4 Development of a platform for biological systems experimentation

4.1 Introduction

Currently, there are several commercially available products based on solid-state thermoelectric technology. They are found in the field of medicine and biological sciences, where high reliability and precise temperature control are required. For example, macro-sized TECs are particularly advantageous for the refrigeration of vaccines and medicine, since the fact that they are highly scalable allows to manufacture compact refrigerators in sizes that are not possible with other methods. They also enable to fabricate refrigerators with near silent operation, which is ideal for noise sensitive areas, such as medication rooms, pharmacies, laboratories and patient rooms. A commercially available compact refrigerator developed by Helmer Scientific Inc. that exemplifies this is shown in Figure 30. The operation of this medical-grade refrigerator is based on thermoelectric cooling technology, which makes it maintenance free.

Figure 30. Commercial use of solid state thermoelectric devices. The figure on the left shows a typical application for this product, while the figure on the right shows the operation principle of the device, whereas a refrigerant that absorbs and transfer heat away from the refrigerator chamber is used. This heat is then dissipated into the environment by a macro-sized thermoelectric module that functions as a heat pump. Courtesy of Helmer Scientific Inc [48].

Other proposed applications of macro-scale TECs in healthcare include cooling bags for medicine transportation [49] and the usage of therapy devices [50-52].

For µTECs, on the other hand, there are several potential applications where their unique properties make them particularly suitable and advantageous. This is the case in biological sciences, where the capability of µTECs to precisely control temperature at scales similar to the

size of biological systems such as cells, could represent a new frontier for in vitro experimentation.

Recent advances in microstructuring and deposition techniques of micro-devices have proven that μTECs can be constructed in a reproducible way and with high reliability [2]. This is the first step towards the manufacture of an experimental platform composed by μTECs, with the aim to be used for studies of the interaction of cellular systems with their thermal microenvironment. However, there are many technical challenges that need to be addressed to make this platform functional.

Hence, in this chapter a conceptual design of a platform for experimentation in microbiological systems is proposed. A study on key parameters that must be addressed is performed and design guidelines for the construction of the experimental platform are provided, with the aim of optimizing its capability to locally and precisely control temperature.

4.2 Thermal analysis on biological systems

Temperature is a physical factor that plays a very important role within biological systems, such as in the form and function of tissue [53]. Some organs and biological systems are known to be highly sensitive to small temperature fluctuations, which has motivated important efforts to study biothermal effects on macro scale biological systems [54, 55].

Novel approaches have been explored, such as using thermocouples [56] and thermistors [57] to investigate the brain or thermal-based therapeutics, like tumor treatment using laser irradiation [58]. Thermotaxis, which refers to the impact that thermal gradients present on the growth or motion of cells, has been largely studied at the organismal level [54, 55, 59, 60]. Yet, perhaps the most revolutionary breakthrough in the last decades within this field has been the discovery of the Polymerase Chain Reaction (PCR) [61, 62].

However, the study of the aforementioned thermal effects at the microscale, i.e. at the cellular level, has not yet been explored in-depth due to severe technology limitations [63]. There is a large variety of attractive applications that could be studied at the scale of tens of microns. From simple studies, such as selective control of cell viability, to more advanced experiments. These could be spatially selective lysing of detection assays, exploring thermotaxis at the cellular level [63] and control and manipulation of biosystems, such as proteins and different cells, as well as biological macromolecules like DNA, which would allow miniaturized PCR processes.

This evidences the necessity of finding novel approaches capable of achieving highly localized temperature control, since traditional technologies are not able to meet this requirements at the microscale. Technological advances of micro-fabrication processes, such as lithographic structuring, deposition techniques, and deep reactive ion etching (DRIE), have made it possible to fabricate novel MEMS capable to perform in-depth investigations of the thermal phenomena in biological microsystems [53, 63-66]. Also to be mentioned is the recent development of a wide range of materials which can be used for novel micro-devices, including Silicon and Silicon related materials [53], soft polymers [67], organic compounds [68] and plastics [69].

In contrast to traditional experiments based on macro scale devices, micro-scale devices allow to locally control several physical factors, such as temperature fields at spatial scales similar to biological cells [53], which enables new possibilities for in-situ cell and macromolecule experimentation [53]. As a consequence, several applications of micro-scale devices have already been proposed, for both basic biological investigations [70] and clinical applications [71, 72].

Miniaturization of bioanalytical tools is also a convenient strategy to overcome some disadvantages and limitations found on macro scale systems. Micro-scale devices reduce costs due to small reagent volumes and they present a much lower thermal mass than their macro scale counterparts. This leads to faster thermal response and thus shorter assay times [73-78].

They also enable to highly parallelize the system by integration of several assays on a single chip [79, 80]. Furthermore, the surface-to-volume ratio is dramatically improved with miniaturization, which opens new chances of functionalization by surface chemistry [81].

Recently, the applicability of a micro-scale heater platform to study the effect of temperature on cell viability and thermotactic effects on individual Pheochromocytoma (PC12) and fibroblast cells was evidenced. This platform was composed by a free-standing thin film, which made it possible to adhere cells on the micro-heater surface and subject them to a controlled spatial temperature gradient. The platform was able to operate over long periods of time and allowed to generate temperature gradients from 0.04 K to 40 K with high resolution [63].

To the author's knowledge, the only study reported that suggests the use of active cooling as a tool for of bioanalytical studies was performed by Prabhakar et al [82]. An analysis of a μTEC was performed using FEM, in order to optimize key parameters involved on the design of discrete temperature regions with minimal interference between them. The study proposed an array of μTECs, whose leg dimensions were 20x10x10 μm, in the format of width, depth and height and a distance between TE legs of 10μm. The whole array of μTECs was embedded within a block of poly methyl-methacrylate (PMMA). The parameters to optimize were the distance between μTEC leg element and the distance between μTEC in a proposed array. It was concluded that the achieved temperature reduction can be enhanced by reducing the distance between μTECs as much as possible, which is limited by fabrication constrains. This reduction of distance helps to obtain a uniform temperature field across the device surface, by diminishing the fluctuations. Furthermore, for the particular system analyzed by the authors, the study concluded that in order to create discrete temperature regions with minimal interference a, distance of 50 μm between adjacent arrays of μTECs should be set. These findings are encouraging, since they proof that localized temperature gradients of ~ 4K could be achieved by μTECs, which is sufficient for most hypothermic experiments on biosystems [63].

4.3 Platform conceptual proposal

While the conceptual design of the an experimental platform for studies of thermal phenomena in biological microsystems is straight forward, a detailed analysis must be undertaken to identify and understand the role that key parameters present on the platform performance. These parameters include the fill and top material required for the system encapsulation and the distance considered between two adjacent arrays of µTECs. This analysis will enable us to reduce the adverse effects involved in the construction and optimize the performance of the system.

A diagram of the proposed experimental platform is shown in Figure 31. The device is composed by an array of µTECs deposited on a substrate and embedded in an isolating material. A commercially available petri dish with a hole in the middle is attached on top of the device and these two components are glued together to prevent fluid leakage with a commercially available sealing frame. In this manner, the assembled set up is suitable for in vitro experimentation. This device can then be placed on top of a printed circuit board (PCB), which is specifically designed to accommodate it and makes it possible to connect external contacts to control the device via wire bonding. This configuration allows the biological system under study to be in direct contact with the µTEC devices and thus to a locally controlled temperature.

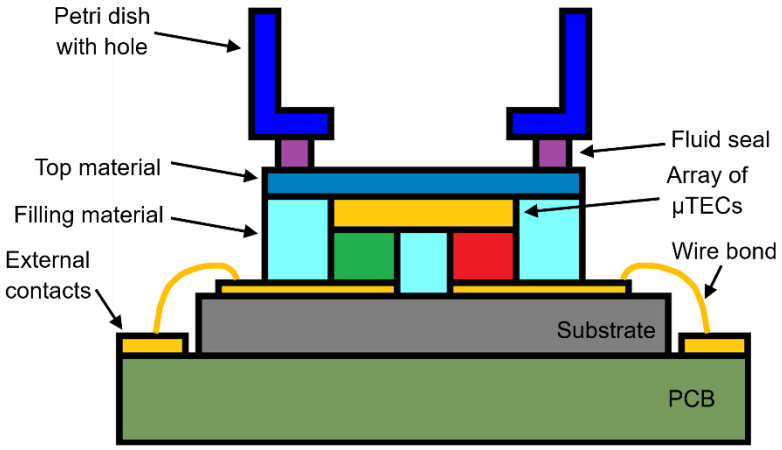

Figure 31. Schematic diagram of the proposed platform for experimentation on the thermal microenvironment of biological systems.

In the previous chapter in-depth studies were carried out on a single leg µTEC in order to optimize its performance. In this section, the parameters to be examined and optimized will be the surrounding components and factors that need to be included in an array of µTECs in order to be adequate for running an experiment. Therefore, the primary objective is to provide

guidelines for the design of a platform, capable of taking advantage of the localized temperature control of μTECs to study the influence of temperature in biological systems.

In particular, two different aspects are analyzed. First, the impact that the presence of fill and top materials carry to the maximum ΔT achieved by the device is examined. These materials are required to isolate the μTEC from the studied biological system, so that any risk of contamination is avoided. The second aspect considered is the interactions between two adjacent arrays of μTECs with the goal of defining the minimum distance that they must present from each other in order to enable the platform to achieve different areas of precisely controlled temperature without mutual interference.

The aforementioned factors and their impact on the micro-device performance will be analyzed in order to provide design guidelines for the optimization, implementation, and construction of an experimental platform for thermal analysis in micro-biological systems.

4.4 Analysis approach

4.4.1 Input current optimization

Using the material properties and geometrical definition detailed in Table 4, a FEM was built with COMSOL Multiphysics. The model consisted of an array of three lines of tree μTECs, each line containing three columns of μTECs, i.e. an array of 3 x 3 μTECs, whereas the considered μTECs were electrically connected in series. The distance between the thermoelectric legs was fixed at 5μm, which represents a realistic scenario that can be manufactured by micro- structuring techniques.

Material	Section	Dimension [width×length×height] [μm x μm x μm]	Electrical conductivity [S cm^{-1}]	Seebeck coefficient [μV K^{-1}]	Thermal conductivity [W m^{-1} K^{-1}]
$Bi_2(Te_xSe_{1-x})_3$	n-type	40x30x12	950	-55	1.2
$(Bi_xSb_{1-x})_2Te_3$	p-type	30x30x12	1800	55	1.1
Gold	Top contact	75x30x8	456000	6.5	317
Gold	Bottom contact p-type	30x30x1	456000	6.5	317
Gold	Bottom contact n-type	40x30x1	456000	6.5	317
Silicon	Substrate	430x300x100	Electrically isolated	Electrically isolated	130

Table 4. Geometry and material properties for analysis of μTEC for biological microsystems experimentation.

It should be noted that the thermoelectric material geometry was defined in order to match the aspect ratio as in Eqn. 27. As a first step, the impact that I presents on the achieved ΔT was numerically investigated. Two different scenarios were studied, the first one considering only the μTEC leg array and the second one considering that the μTEC devices are embedded in PMMA, with a thermal conductivity of 0.18 $Wm^{-1}K^{-1}$[82]. The latter is a common polymer used in many applications for its mechanical properties, environmental stability, and low cost [83]. Diagrams of the FEM used for the analysis of the studied systems are shown in Figure 32.

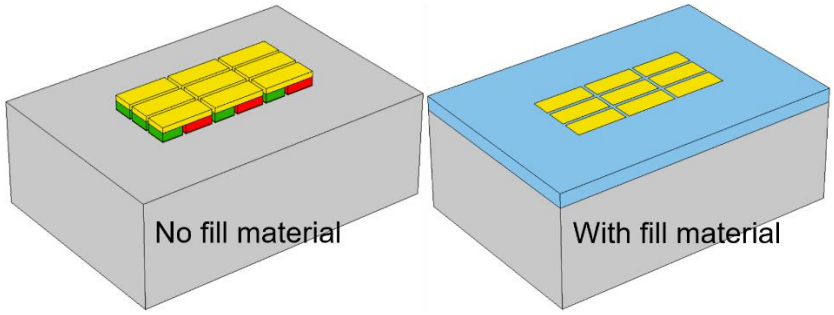

Figure 32. Schematics of the FEM used to analyze the effect that the fill material presents on ΔT. Two studied scenarios are considered: a device without fill material and a device embedded in PMMA. The colors in the diagram correspond to the p-type thermoelectric material (green), n-type thermoelectric material (red), Au contacts (yellow), Silicon substrate (gray), and fill material (blue).

The input current was varied from 0 to around 100 mA and the calculated average ΔT on top of the metallic contact was recorded, as summarized in Figure 33. In both cases, a maximum ΔT was found when a current of 80 mA was applied. The maximum ΔT obtained for the case without fill material was 6.55 K, while for the case with fill material this value was found to be 5.76 K. The presence of a fill material did not shift the maximum ΔT to higher or lower input currents, but significantly attenuated the amplitude of ΔT, due to the thermal shortcut that arises between the Joule heating generated at the bulk of the leg pairs and the metallic top contact.

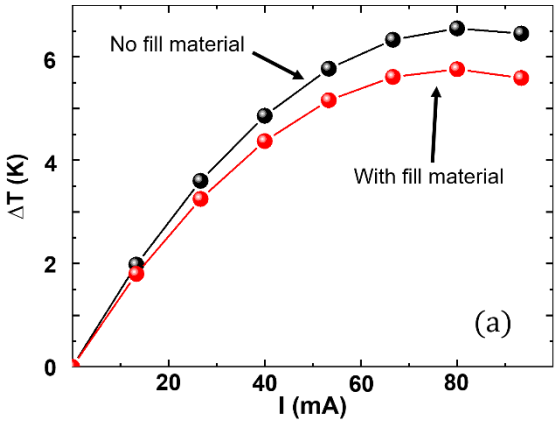

Figure 33. Summary of the FEM on the effect that the fill material presents on ΔT for the case of a device without fill material and a device embedded in PMMA.

4.4.2 Fill material

Next, the effect that the choice of fill material presents on ΔT was investigated. For this, the thermal conductivity of the fill material, λ_{fill}, was varied from 0.1 to 300 $Wm^{-1}K^{-1}$, while keeping the I at 80 mA. Results revealed that the increment of λ_{fill} from 0.1 $Wm^{-1}K^{-1}$ to 1 $Wm^{-1}K^{-1}$ reverts to an abrupt decrement of ΔT from 6 to 4 K. From this point on, as λ_{fill} increases a further reduction of ΔT is observed, but with a less pronounced effect. When λ_{fill} reaches 10 $Wm^{-1}K^{-1}$, ΔT is reduced to only 0.8K and no effective cooling is observed when λ_{fill} is roughly 50 $Wm^{-1}K^{-1}$, as shown in Figure 34.

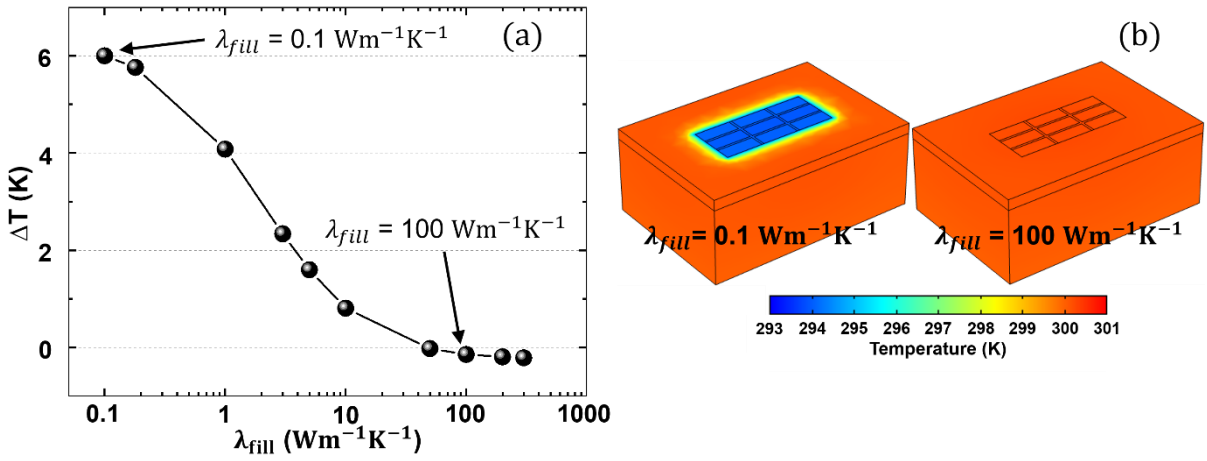

Figure 34. Impact of λ_{fill} on ΔT. a) Evolution of ΔT as a function of λ_{fill}. b) Temperature distribution for the cases of λ_{fill} = 0.1 $Wm^{-1}K^{-1}$ and λ_{fill} =100 $Wm^{-1}K^{-1}$.

This evidences the need of choosing a fill material with the lowest thermal conductivity possible, which is not always a free parameter due to construction limitations.

4.4.3 Thermotaxis

In order to analyze the variability of the studied platform for thermotaxis investigations, the FEM was extended into a 6 column x 3 line configuration and different *I* values were applied at each column, to generate a temperature gradient across the device surface. Hence, *I* values of 80mA, 70 mA, 60 mA, 50 mA, 40 mA and 30 mA were applied to each of the thermoelectric leg pairs at each of the studied columns, respectively. This condition was analyzed for the case of varying λ_{fill} .

As observed in Figure 35, as the thermal conductivity of the fill material was increased, the system gradually lost the capability to precisely control the temperature gradient. Nevertheless, depending on the desired application of the experimental platform, the distance between thermoelectric elements as well as λ_{fill} can be selected so that specific requirements are met. There are several fill materials whose thermal conductivities are low, making them potential candidates for this propose, for example, polymers or sodium silicate.

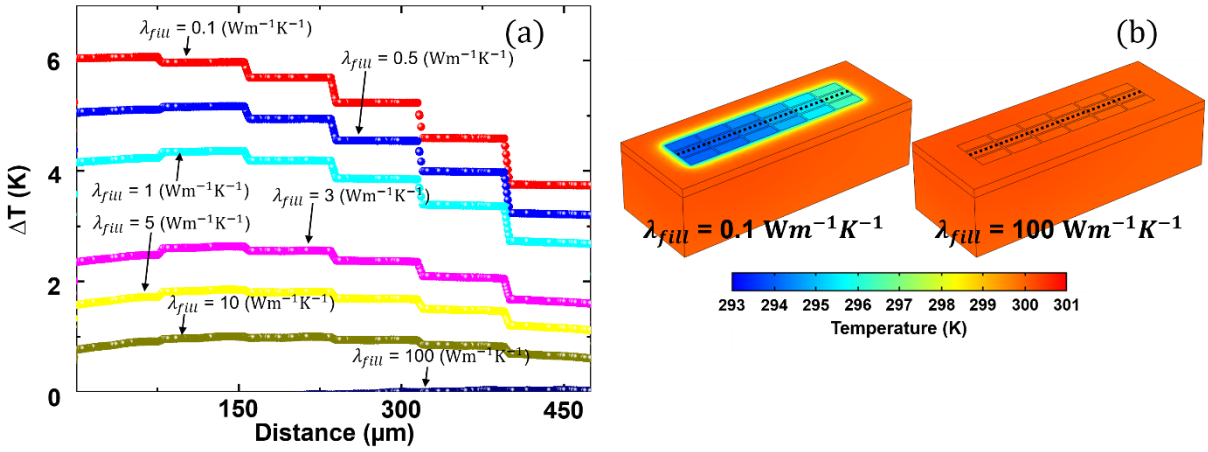

Figure 35. Impact of λ_{fill} on ΔT across the μTEC device. a) ΔT across the surface of the μTEC device after applying a varying current between 80 mA and 30 mA at each line of μTECs for different λ_{fill} . b) Temperature distribution for the cases λ_{fill} 0.1 Wm^{-1}K^{-1}.and 100 Wm^{-1}K^{-1}.

It can be concluded that the platform under development is a suitable approach to study thermotaxis in micro-biological systems, whereas the capability of the platform to generate temperature gradients with great precision will depend solely on the selection of the fill material.

4.4.4 Top material

Once the fill material has been selected, the next step is to deposit a biocompatible top material on the device. This is to encapsulate the array of μTECs and thus prevent contamination of the biological system with the electrochemically deposited materials. Therefore, the impact of this top material on the device performance has to be analyzed, so that its detrimental effects are diminished.

There are some commercially available biocompatible materials that can be considered for the encapsulation process, such as Al_2O_3, TiO_2, and PMMA. Depending on the material selected its thickness will be constrained by manufacturing limitations. For this investigation a 10 μm thick layer of top material was set for the FEM, which is a typical value used for the deposition polymers, such as photoresists. In addition, the previously studied fill material was considered as PMMA, with a thermal conductivity of 0.18 $Wm^{-1}K^{-1}$ [84, 85]. For the analysis, the applied electrical current was the same as the one described in the previous thermotaxis study, with an input I between 80 mA and 30 mA across the different columns of μTECs. Likewise, the thermal conductivity of this top material, λ_{top} was parametrically analyzed.

Results are summarized in Figure 36 and they show that adding a top material creates significant losses of both the achieved ΔT and the temperature profile measured across the device compared to the results without top material. The temperature profiles are considerably smoothed out, even in the case when the λ_{top} presents a low value. As λ_{top} increases, the capability of the system to precisely control temperature is compromised. However, the ΔT achieved was still relatively high, at a value of around 5.3 K, when λ_{top} of 0.5 $Wm^{-1}K^{-1}$ was considered. This suggests that the platform is well suited for common thermal experimentation in biological systems after the encapsulating process [63].

It is noteworthy to highlight that further improvement of the system can be achieved by optimizing the deposition parameters of the selected encapsulating material. As its thickness is reduced, the capability of the system to control locally the temperature will increase.

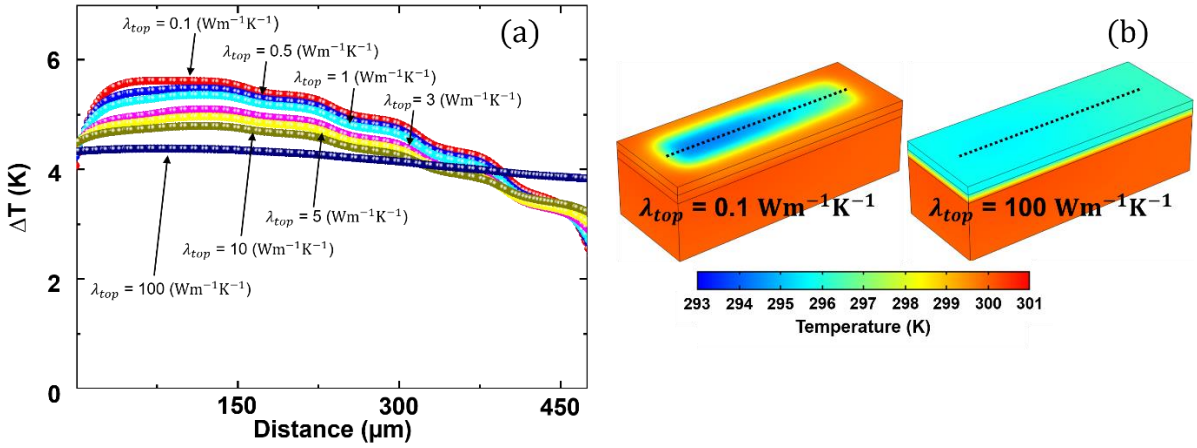

Figure 36. Impact of the encapsulating material thermal conductivity on ΔT across the μTEC device. a) ΔT across the surface of the μTEC device as a result of λ_{top}.variations. b) Temperature field of as for the case of λ_{top} 0.1 $Wm^{-1}K^{-1}$ and 100 $Wm^{-1}K^{-1}$.

4.4.5 Cold spot optimization

An attractive capability of a platform composed by µTECs is the possibility to run different studies simultaneously. For this, two areas with high temperature control or "cold spots" must be able to operate simultaneously without interfering each other. To address this, the distance between two adjacent cold spots must be optimized in order to allocate as many cold spots within the same area of the micro-device with interference free operation as possible.

Starting from the FEM shown in the last section, the array of µTECs was subdivided into two different arrays of 3 x 3 µTECs each. An input *I* of 80 mA was applied at each of the µTECs considered. With this model, two main parameters were studied: the distance between these two different arrays and the thickness of the top material. The results are summarized in Figure 37. It can be concluded from this analysis that both parameters present a plausible effect on the temperature distribution. The distance between the µTEC arrays strongly affects the capability of the cold spots to interfere with each other. It was found that a distance of 200 µm is sufficient to allow two different arrays of µTECs to operate without mutual interference. Furthermore, it was observed that an increment of the thickness of the top material smooths the calculated temperature profile, although its impact is smaller than the one of the previous parameter.

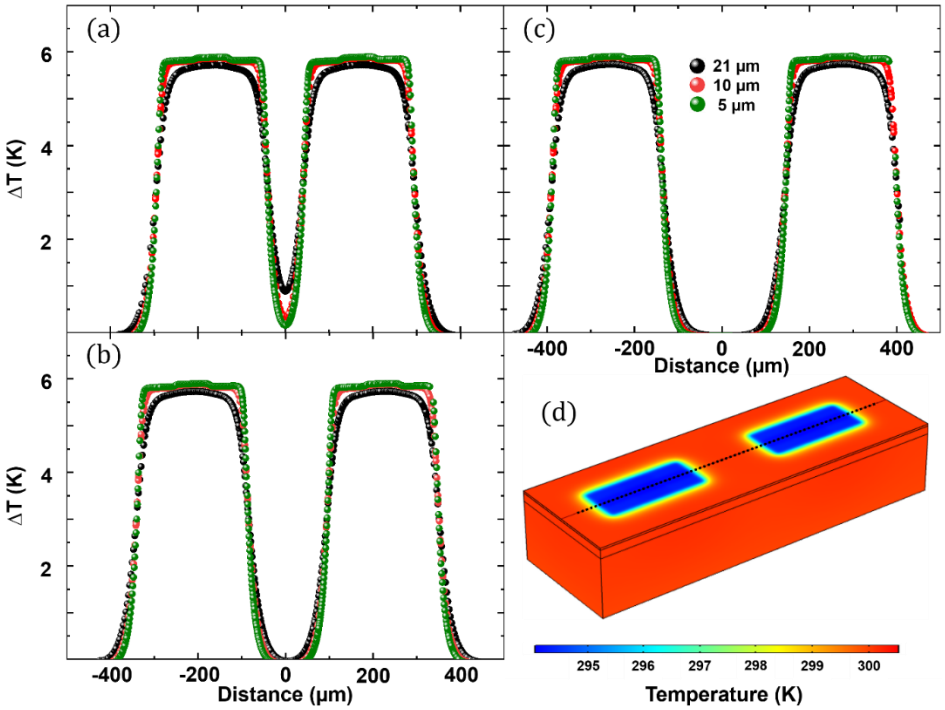

Figure 37. Effect of the top material thickness and distance between arrays of µTECs on ΔT across the µTEC device. The displayed results consider a distance between the arrays of µTECs of 100 µm (a), 200µm (b) and 300 µm (c) for the cases of a top material thickness of 21µm (black), 10µm (red) and 5µm (green). d) Temperature distribution for the case of 300 µm distance between thermoelectric leg pairs array and a thickness of the top material of 5µm.

4.5 Experimental platform construction

The analysis results previously shown can be directly used for the design optimization of the experimental platform for thermal investigations in biological microsystems. The device is designed with three independent active areas, each being composed by single rows of cooling elements that can be actuated individually. Diagrams of the device as well as the steps involved in the proposed experimental implementation are depicted in Figure 38.

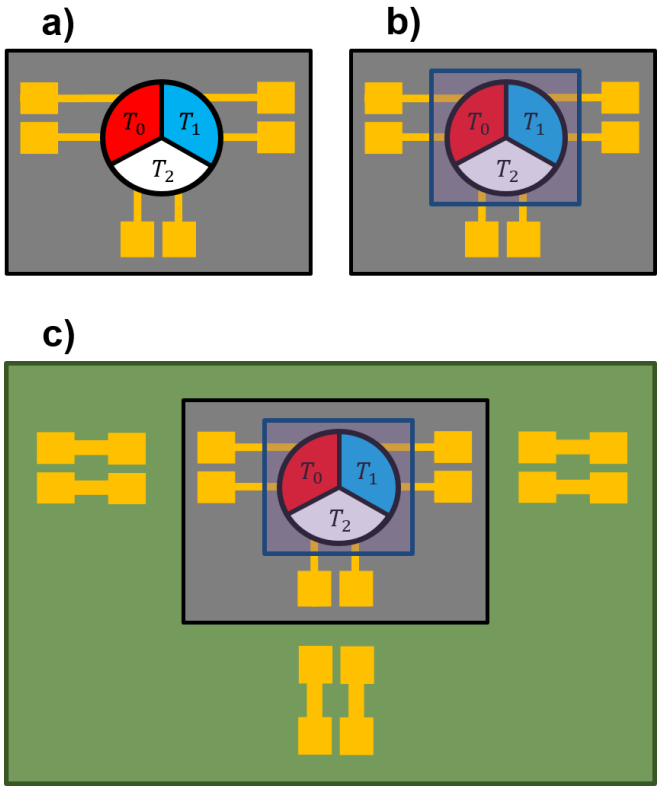

Figure 38. Schematic diagram of the proposed experimental implementation of the platform for thermal investigations in biological microsystems. a) The device has three different active areas where single rows of µTECs can be independently activated, which are defined as T_0, T_1, and T_2. It is constructed according to the process developed by Li et al. [2]. b) The encapsulating process is performed by covering the area where the active µTECs are deposited with a biocompatible material. c) A PCB is attached to the chip where the active µTECs are located. The latter is specifically designed to match the electrical contacts of the µTECs, while the contacting between the two can be performed by wire bonding. The material colors in the diagram correspond to the PCB (green), Au contacts (yellow), Silicon substrate (gray), and encapsulate material (blue).

The total area where the active µTECs are deposited was defined as 19.63 mm^2, which corresponds to a diameter of 5 mm and is a standard dimension for ECD process. Likewise, in accordance with the results from the cold spot optimization, a distance between adjacent arrays of µTECs is defined between 200 µm and 300 µm, so that interference free operation is granted. With the aforementioned criteria a mask to be used for photolithography was constructed within

LASI, as shown in Figure 39 and 40. The geometry of the µTECs was optimized by considering the material properties reported by Li et al. [2] and the aspect ratio of Eqn. 27, which resulted in a geometry of 115 x 30 µm2 for the p-type and 30 x 30 µm2 for the n-type cavities. The distance between the thermoelectric legs was set at 50 µm. A mockup of the proposed experimental set up is shown in Figure 41.

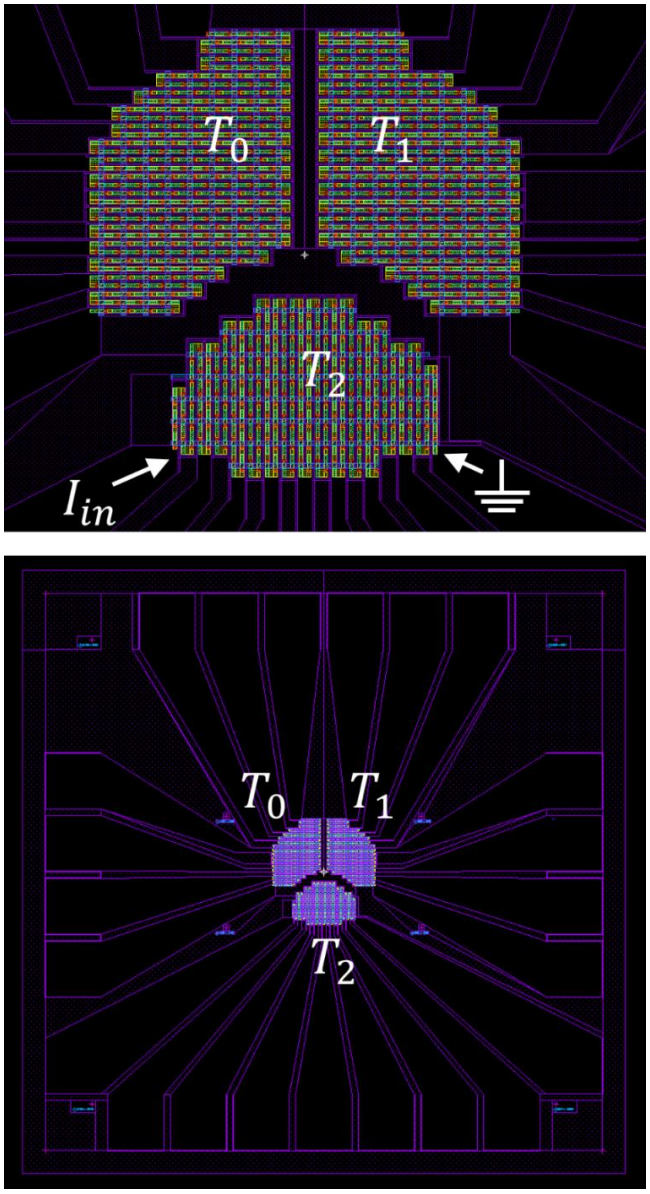

Figure 39. Photolithography mask design for the independently activated µTECs for thermal investigations in biological microsystems.The different active temperature controlled areas T_0, T_1, and T_2 are indicated. The configuration of the input electrical control signal is illustrated for the case of T_2 (above). Redundant electrical connections are included for all of the independently controlled temperature areas (below). The total number of active leg pairs is 241 for T_0 and T_1, and 170 for T_2 The different layer colors in the mask correspond to the p-type (green), n-type (red), Au contacts (yellow), and Au seed layer removal (purple and blue).

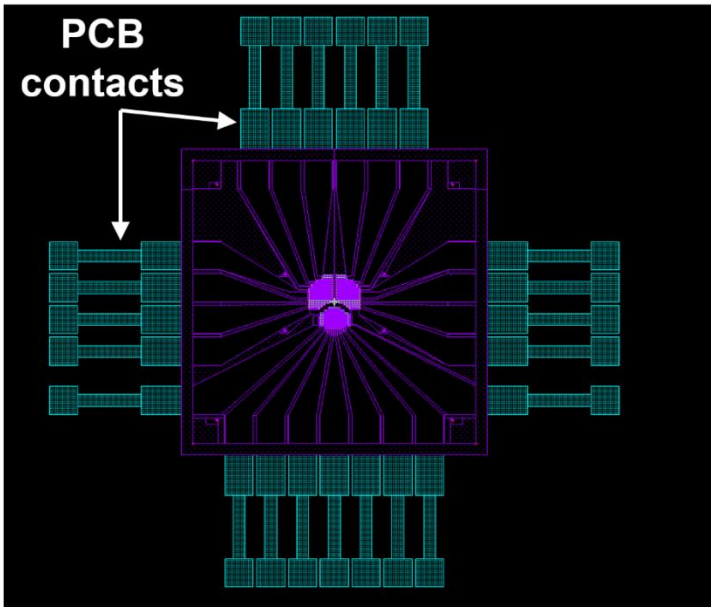

Figure 40. Photolithography mask for the chip containing the active µTECs and the PCB designed to externally connect the electrical control signal. The total area of the Silicon substrate is 25 x 25 mm^2 and the area for the attached PCB is 50 x 50 mm^2. After fixing the chip with the µTECs on the PCB, wire bonding can be employed to connect them electrically.

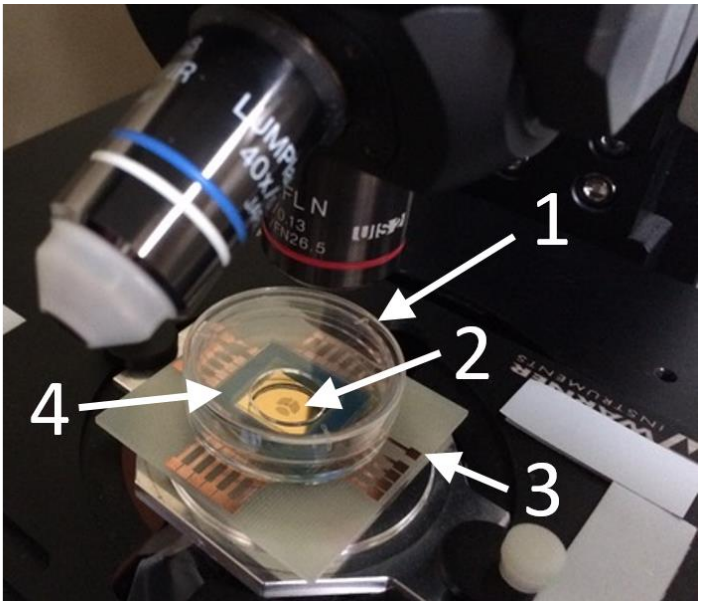

Figure 41. Mockup of the proposed experimental set up for the platform for thermal investigations in biological microsystems. The set up is composed of 1) a commercially available petri dish with a hole in the middle, 2) a chip with three independent arrays of active µTECs, 3) a PCB with external contacts, 4) a commercially available sealing frame, developed by Thermo Fischer Scientific and suitable for cellular imaging. The complete platform is placed under an optical microscope to perform in vitro investigations. Photograph taken by Dr. Nicolas Perez and Adytia Dutt.

4.6 Summary

In this chapter the conceptual design of an experimental platform based on μTECs to be used for thermal investigations in biological micro-systems was proposed. A systematic study on key involved parameters was undertaken, taking into account realistic material properties, analysis assumptions, and device dimensions.

It was demonstrated that even after performing the required embedding and isolating processes on the analyzed array of μTECs, the experimental platform is capable to achieve temperature gradients of around 5.3 K with high spatial resolution. The predicted temperature gradient is close to values typically used for similar investigations, which suggests that this technique is suitable for the intended experimentations.

Results evidenced that the material selection for both the fill and the encapsulating processes is a critical factor, since the thermal conductivity of these materials presents a strong influence on the achieved temperature gradient. A poor selection of these materials can lead to significant losses of the temperature and spatial control of the platform. It should be noted, however, that the selection of the embedding and fill material is not always a free parameter, as this can be constrained by manufacturing limitations.

The analysis results allowed us to design a lay out for the photolithography mask to fabricate the device, as well as the required components for the experimental implementation.

In summary, these results offer design guidelines for the proper selection of materials and dimensions that enable the practical implementation of the studied experimental set up with optimized performance.

“No repartas riquezas, reparte trabajo: así elevaras el nivel de vida del pueblo.”

“Do not distribute wealth, distribute work opportunities: this way you will raise the standard of living of the people.”

– Eugenio Garza Sada, mexican industrialist and philanthropist, * 1892 † 1973 –

5 Development of a technique for thermal transport characterization in thin films

5.1 Introduction

As previously discussed in Chapter 3, the characterization of the thermal parameters of materials deposited as thin and thick films is not a straight forward task due to different technology challenges involved. In addition, it is commonly found across a wide variety of materials that the thermal transport properties are directionally dependent, i.e. anisotropic. This condition can be caused by several reasons, such as anisotropy of the Bravais lattices, interatomic strengths or nano- and microstructures [86].

In recent decades, various works have focused on developing experimental techniques for the characterization of the anisotropic thermal transport of bulk materials. Nonetheless, these techniques are normally not suitable to extract thermal parameters of materials at the nano- and micro-scale, due to their lack of spatial resolution [87, 88].

Hence, this chapter introduces an experimental methodology to estimate anisotropic thermal conductivity of nano- and micro-scale materials, which is based on optical pump-probe thermoreflectance imaging microscopy. The sample under study was composed of a transducer-thin film-substrate stack. The thermal conductivity of the individual sections of the sample was characterized beforehand. In this manner, this sample was used as a model system for the validation of the proposed technique.

The experimental set up was employed to optically excite the examined sample and simultaneously perform thermal imaging to map the generated temperature distribution on its surface. The experimental data was later used as a correlation parameter for a FEM, which allowed us to perform a numerical analysis of the impact that key experimental parameters present on the surface temperature distribution. In this manner, the impact of the thermal conductivity anisotropy of the examined thin film on the generated temperature distribution was assessed. The conclusions of this study made it possible to define the conditions under which the experiment needs to be carried out in order to extract both the in-plane and the through-plane thermal conductivity of the analyzed sample.

This chapter represents the summary of a research collaboration between the Thermoelectric Materials and Devices group of Dr. habil. Gabi Schierning at the Leibniz Institute for Solid State and Materials Research (Dresden, Germany) and the Quantum Engineered Systems and Technology group of Prof. Dr. Ali Shakouri at the Birck Nanotechnology Center in Purdue University (West Lafayette, USA).

5.2 Thermal anisotropy characterization in thin films

Several approaches based on time domain thermoreflectance (TDTR) have been proposed to extract the anisotropic thermal conductivity of thin films. Among them, Jiang et al. [86] simultaneously extracted both the in-plane (λ_r) and the through-plane (λ_z) thermal conductivity of different materials by a variable spot size approach. Feser et al. [89, 90] proposed to use a TDTR beam-offset configuration in order to extract the material anisotropy by sensing the surface temperature at a different location than where heat was induced. Jiang et al. [87] proposed an alternative to the beam-offset method by using a highly elliptical pump beam in order to induce a quasi one-dimensional temperature profile whose TDTR signal is exclusively sensitive to λ_r. Also, modified 3-omega method [91, 92] and the transient thermal grating for this purpose have been reported [93].

However, the above methods require elaborated experimental set ups and the solution of complex analytical mathematical models to characterize the target sample, which significantly inhibits their broad practical application. Therefore, the development of a straightforward experimental technique to characterize anisotropic thermal conductivity of thin film systems remains as a paramount tasks. This would allow further enhancement among a range of engineering fields such as electronics, optoelectronics, high-temperature superconductors, thermoelectrics, thermal insulators, and thermal management [88].

5.3 Experimental apparatus

Thermoreflectance imaging microscopy has already been introduced in this work, as a technique capable to measure temperature changes in surfaces and devices under cyclic pumping. The excitation is typically performed by applying an electric current to the device under test. This technique is well suited for investigations of hot spots in integrated circuits and micro-electronic components [23], for the characterization of the thermal properties of materials [23, 94], and for the thermal characterization of micro-thermoelectric devices [2, 24, 95, 96].

Thermoreflectance imaging can also be operated by applying an optical excitation to the device under study instead of an electrical current. This modified experimental configuration is known as optical pump-probe thermoreflectance imaging microscopy. The applicability of this technique to extract thermal parameters of materials at the macro-scale and micro-scale has recently been demonstrated [97]. The primary advantage of this technique, compared to other optical techniques, such as TDTR, is that instead of using a photodiode to probe the temperature of the target sample's surface at a single point, a high signal-to-noise camera simultaneously measures the change in reflectivity of the sample's surface within the complete field of view of the coupled microscope. This is achieved by using a probe pulse that illuminates the sample and records the change in each pixel intensity of the coupled camera, obtaining a 3D probe response. After this process, the acquired thermoreflectance image can be transformed to a 3D thermal map from the device surface by scaling it with the material thermoreflectance coefficient. The experimental apparatus used for this work is shown in Figure 42.

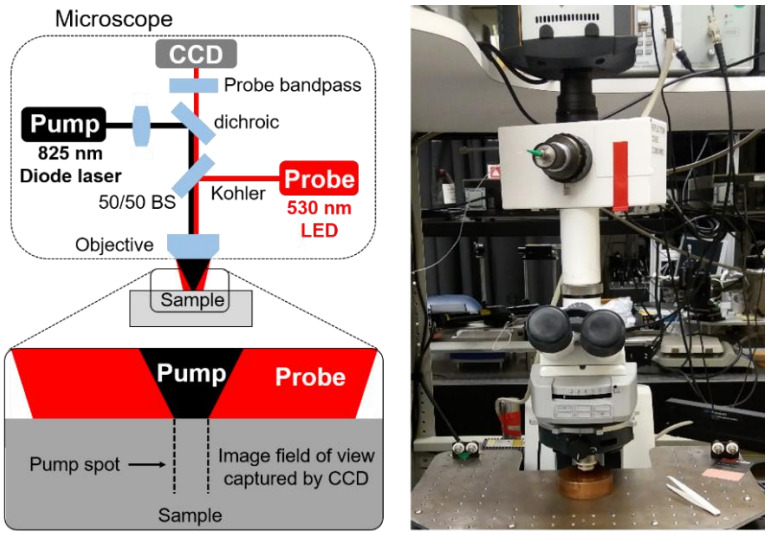

Figure 42. Experimental set up for optical pump-probe thermoreflectance imaging microscopy. Schematic diagram of the main components, adapted from [97] (left). Photograph of device used for the measurements shown in this work (right).

The experimental set up employed for this study featured an 825 nm diode laser coupled into the microscope. The laser was focused to a spot on the sample surface in order to thermally excite it. The microscope full field of view was illuminated by a monochromatic LED centered at 530 nm that functioned as a probe. This set up was based on a commercially available Microsanj equipment.

The experimental measurements performed in this work were taken with a 100X magnification objective, with a numerical aperture of NA = 0.75. The field of view captured by the CCD at this magnification was approximately 80 x 80 μm^2. This particular experimental set up provided temperature and spatial resolutions of ~10 millikelvin and ~250 nm, respectively [97, 98]. The experimentally obtained pump and probe signals from the control sample are shown in Figure 43 and 44, respectively.

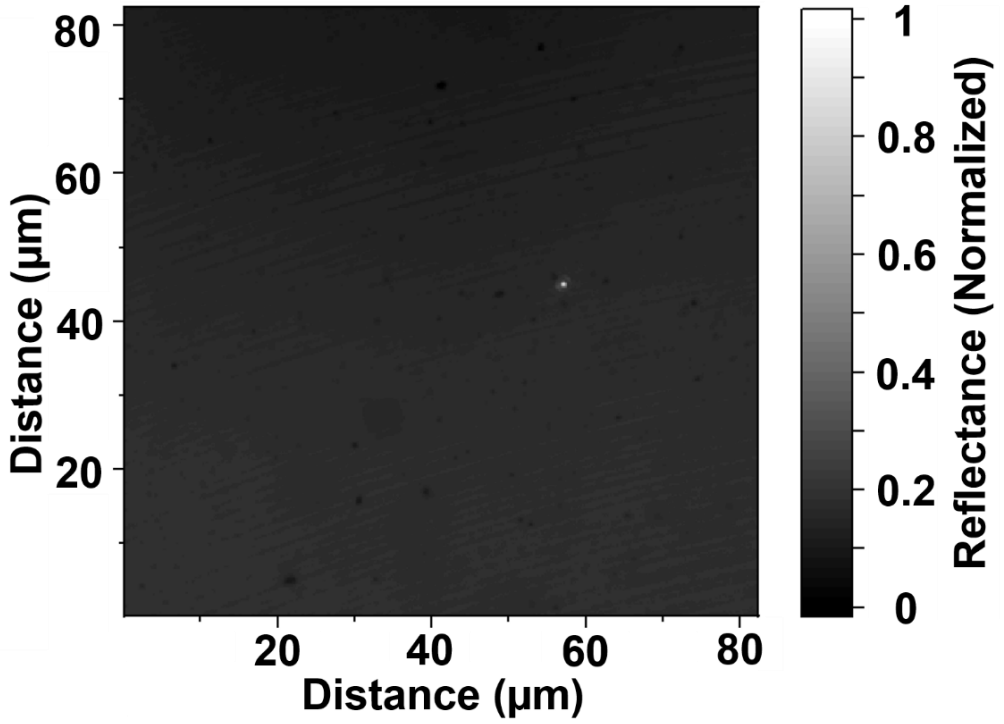

Figure 43. CCD image of the pump laser spot focused on the control sample surface.

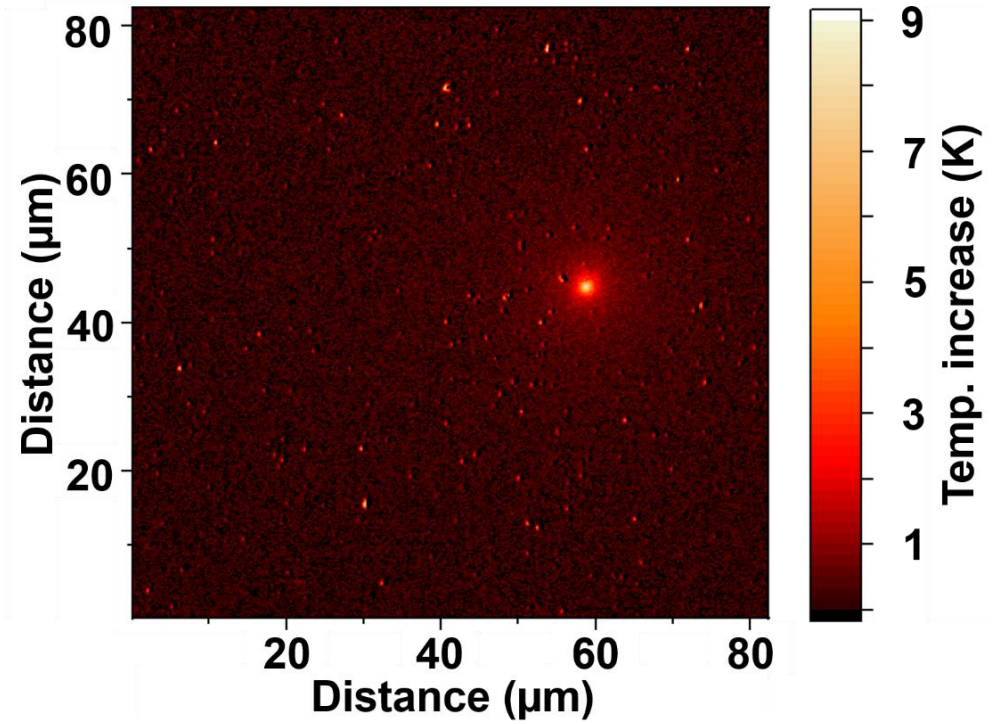

Figure 44. Measured temperature map generated on the control sample surface.

5.4 Experimental measurements

Several measurements of the normalized reflectance from the pump laser focused to a spot on the sample surface were taken from the CCD image. These data was later processed in MATLAB in order to find the fitting parameters by assuming a Gaussian distribution, expressed as

$$f(x) = \frac{1}{\sqrt{2\ Pi\ S^2}} exp^{\frac{-(x-\mu)^2}{2\ S^2}} \qquad \text{Eqn. 28}$$

where S stands for the standard deviation and μ refers to the mean value. An average of the laser spot S was found at 0.45 (+/- 0.1) µm. The normalized pump laser Gaussian profiles that were fitted in MATLAB are summarized in Figure 45.

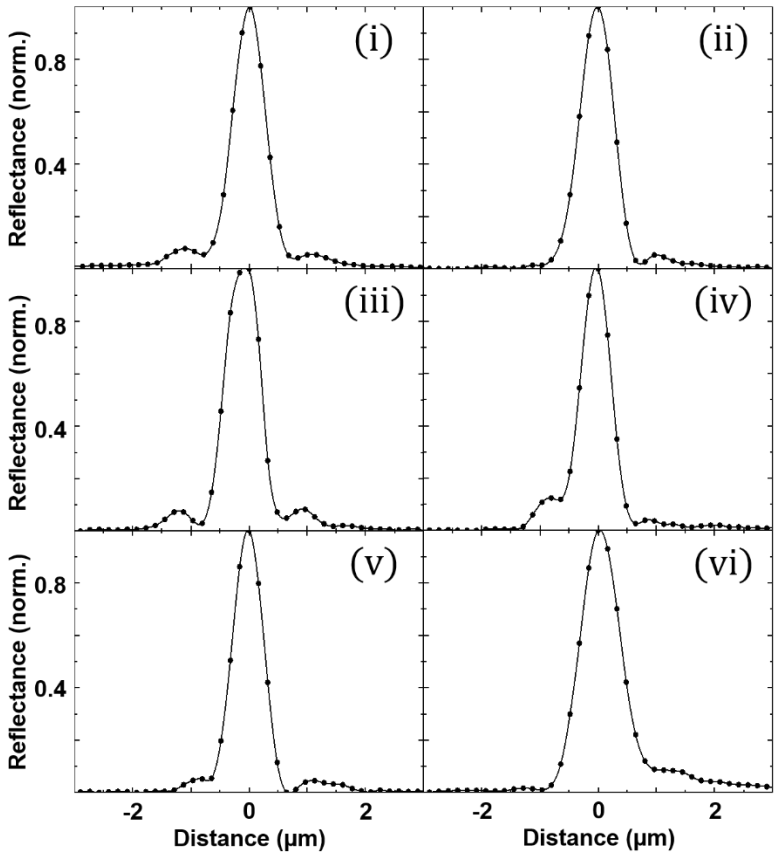

Figure 45. Normalized profile of the laser pump spot focused on the surface of the sample under study.

The target sample was then subjected to thermal excitation by the pump laser and the average temperature increase signal was recorded. A total of ten measurements were performed on the sample at different locations.

The signal-to-noise ratio of the recorded thermoreflectance signal can be enhanced by averaging the measured change in reflectance over a long period of time, described as

$$measured\ noise = \frac{1}{\sqrt{t_{averaging}}} \quad \text{Eqn. 29}$$

where $t_{averaging}$ refers to the averaging time. Nevertheless, while carrying out long time averaging measurements at high magnifications, slight temperature fluctuations lead to thermal expansion of the experimental apparatus. This can originate microscope defocusing at the plane of the sample. For this reason, commercially available electrically pumped thermoreflectance imaging microscopy equipment features a high performance piezoelectric fixture stage. This controls the system focus and allows the user to average a measurement over long periods of times. However, the experimental measurements shown herein were conducted at a newly developed experimental platform that did not present a piezoelectric fixture stage. Hence, in order to reduce the effect of defocusing over time, all of the measurements taken were averaged over relatively short durations of ten minutes. The analyzed sample was placed on top of a large Copper heat sink during measurements so that the pump laser input power could be effectively dissipated.

In order to reduce the inherent noise that the experimental data could present and maximize the number of data points used for the analysis, a surface fit can be performed to the 3D recorded probe signal by selecting an appropriate fitting function. It has recently been demonstrated that a Gaussian distribution is relatively inappropriate to describe anisotropic heat diffusion analyzed via optical pump-probe thermoreflectance imaging, since the measured temperature is relatively closer to a Lorentzian distribution [97]. Hence, for the results shown in this chapter, the experimentally obtained temperature maps were fitted by a 3D Lorentzian distribution in MATLAB, by considering the following equation

$$f(x,y) = \left[\frac{\Upsilon}{Pi\ [\ \Upsilon^2 + (x-a)^2 + (y-b)^2\ ]} \right] c \quad \text{Eqn. 30}$$

where Υ refers to a scale parameter, a is the location parameter in the x coordinate, b is the location parameter in the y coordinate and c refers to a linear factor. The extraction of Υ, a and c from the 3D temperature map made it possible to express the temperature map within a two-dimensional (2D) Lorentzian distribution. This allowed us to directly compare the experimental measurements to our FEM results.

The different temperature maps obtained experimentally were fitted by a 3D Lorentzian distribution and the effect of the number of pixels considered on the R-squared value of the curve fit was analyzed. In all cases, the best fit was obtained when a temperature map of 15 x 15 pixels (~ 2.4 x 2.4 μm²) was considered, leading to R-squared values up to 0.92.

The previously described process for the experimental extraction of the pump and measured signals as well as the resulting Lorentzian fit is depicted in Figure 46.

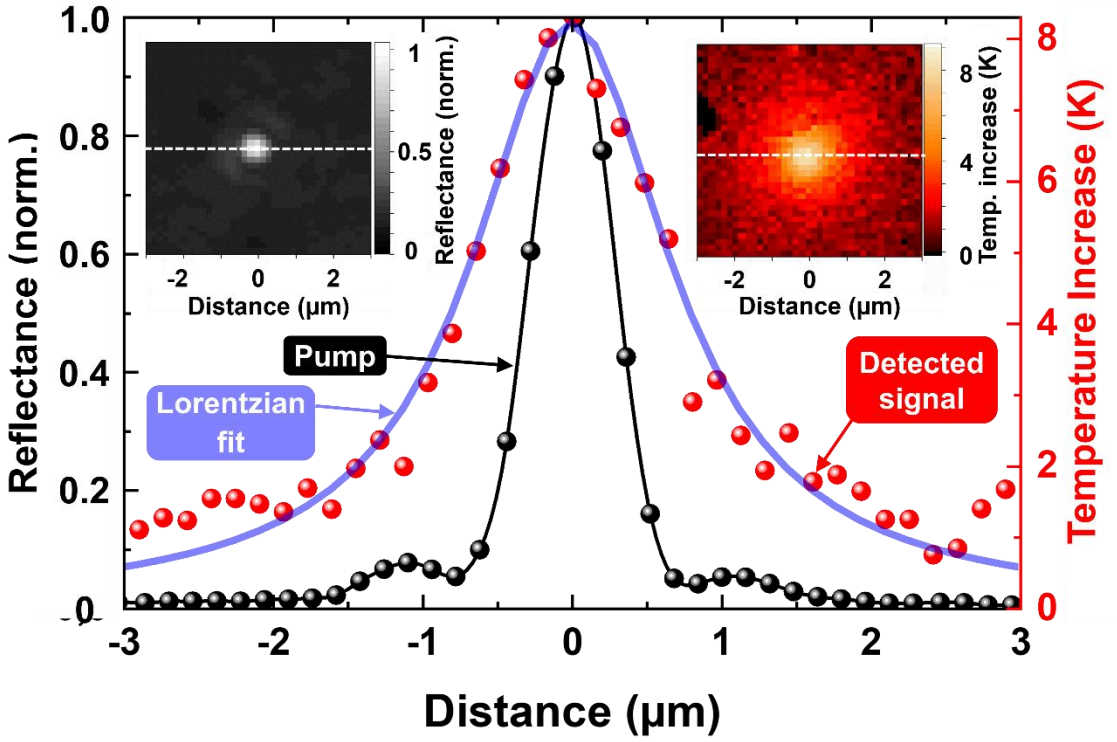

Figure 46. Extracted profiles of the normalized pump reflectance, the measured temperature increase, and the Lorentzian fit of the control sample.

5.5 Analysis approach

A FEM that included the target sample geometry and material properties, as detailed in Table 5, was built in COMSOL Multiphysics. For the laser pump, a deposited beam power with a Gaussian profile was constrained at the center of the top face of the TiN transducer. It was assumed that the effect of defocusing is negligible. Therefore, the laser S was fixed at 0.45 µm. In addition, the effect that the thermal contact resistances present on the generated temperature distribution was neglected. Hence, the laser power, P_0, was the only free parameter to correlate our FEM with the experimental data.

Section	Material	Thickness	Thermal conductivity $[\mathrm{W\ m^{-1}K^{-1}}]$
Transducer	TiN	100 nm	63
Thin film	(TiAlSc)N	250 nm	24
Substrate	MgO	100 µm	60

Table 5. Isotropic material properties and geometry of control sample used for optical pump-probe thermoreflectance imaging. This sample was previously characterized via TDTR [99].

A schematic diagram of the FEM of the analyzed sample including material properties and geometry considered is shown in Figure 47. As boundary conditions, a perfect heat sink was assumed and therefore the temperature at the bottom of the MgO substrate, T_{MgO}, was fixed at 300 K.

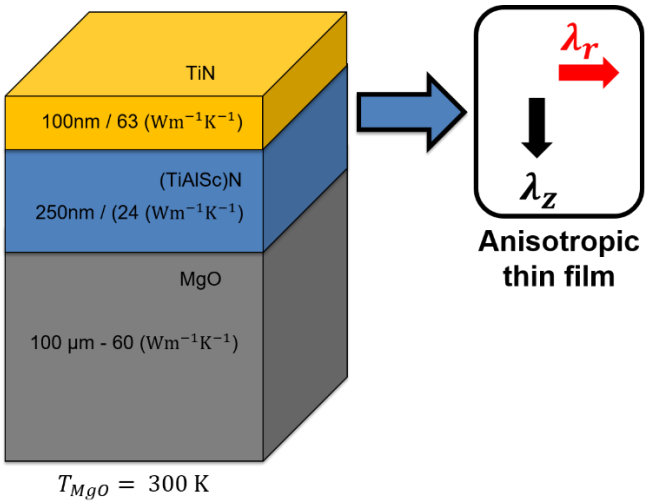

Figure 47. Schematic diagram of the FEM of the control sample used for optical pump-probe thermoreflectance imaging. The corresponding anisotropy thermal conductivities of the thin film under analysis, λ_r and λ_z, are illustrated in the schematics.

In the experiments, fluctuations of the amplitude in the measured temperature increase between ~ 8 K and ~ 4 K were observed. All of these temperature distribution curves could be correlated to numerical simulation by varying the laser P_0 in the FEM. A summary of the best fit between experimental and simulation results, as well as the 2D Lorentzian representation of the measured temperature distributions is shown in Figure 48.

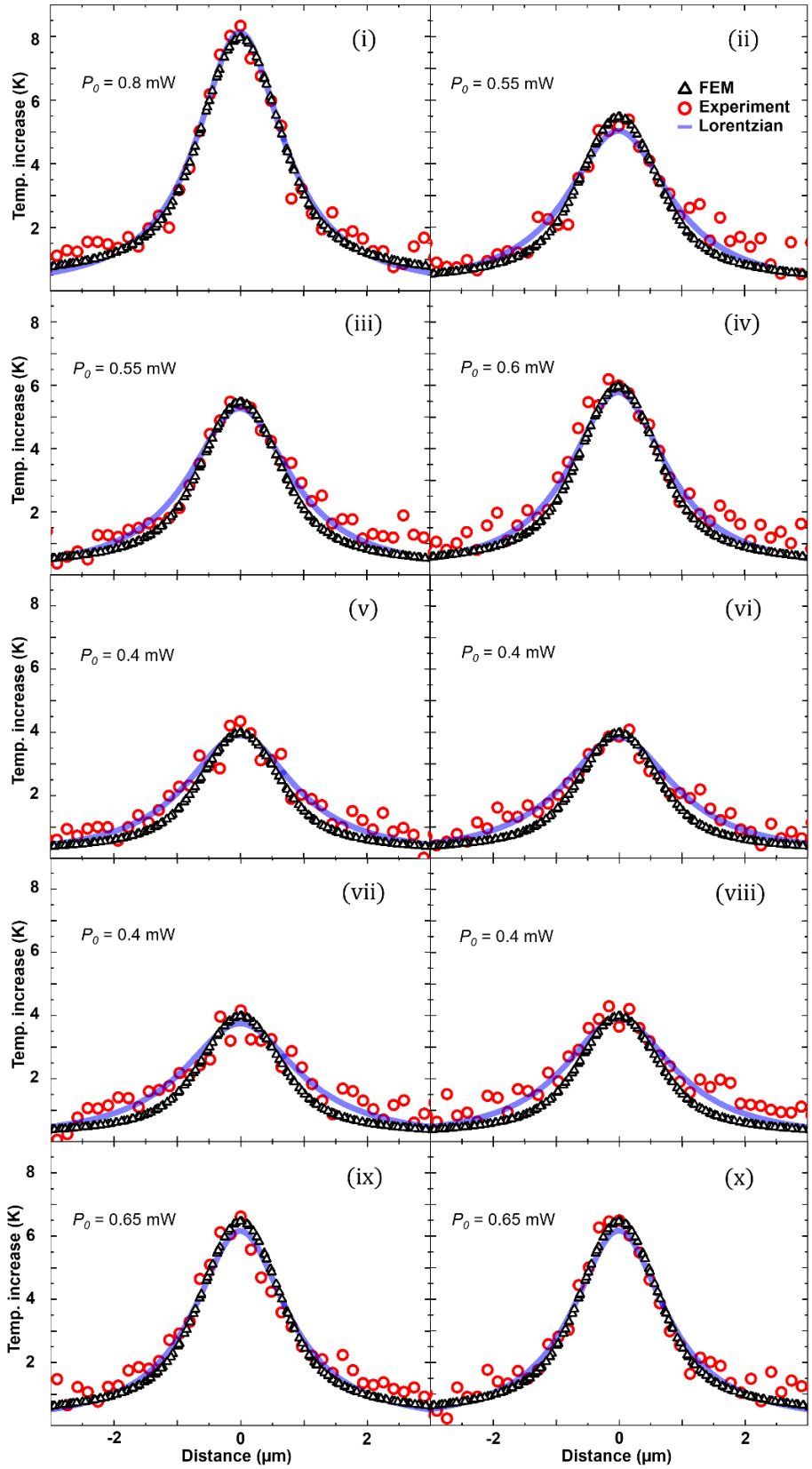

Figure 48. Summary of the temperature distributions obtained by experimental measurements and FEM simulation. In each case the value of P_0 that led to the best fit in the FEM as well the 2D Lorentzian representation of the experimental data are included.

It can be observed in Figure 48 v), vi), vii) and viii) that the measurements with low laser power absorption (with P_0 values of 0.4 mW) show a low signal-to-noise ratio and a poor agreement between FEM and experimental data. The agreement tends to increase as P_0 presents higher values, which is the case for Figure 48 i), ii), iii), iv), ix) and x).

In summary, fluctuations of P_0 between 0.4 to 0.8 mW were observed across the different measurements, which were performed under identical experimental conditions on the same sample. These fluctuations result from surface inhomogeneities of the investigated sample, as evidenced in Figure 44. This provides an insight on the profound effect that roughness variations and defects of the sample surface present on all-optical thermal imaging measurements.

The effect of fluctuations on the P_0 experimental measurement is illustrated in Figure 49, where numerically calculated temperature distributions for the studied sample are shown as a function of P_0 variations from 0.4 mW to 0.8 mW.

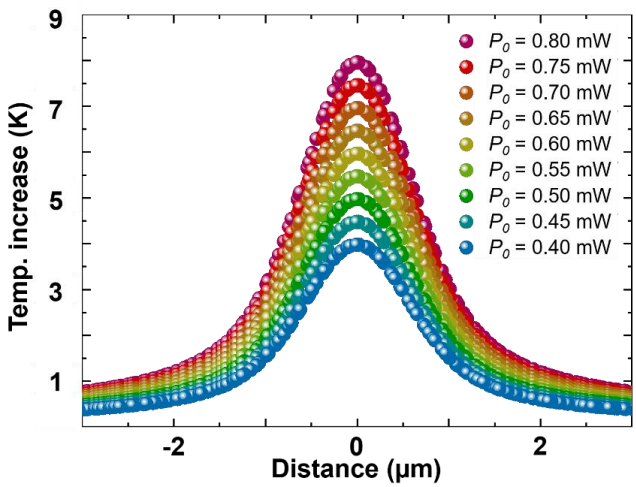

Figure 49. Effect of P_0 on the temperature increase.

In a further step, the previously correlated FEM was used to parametrically study the effect that anisotropic properties, λ_z and λ_r, of the problem layer (in the experiment TiAlSc) present on the temperature distribution on the sample surface. In order to perform a conservative analysis, P_0 was set in the FEM to the lowest experimentally observed value of 0.4 mW for the following simulation cases.

5.5.1 Thermal conductivity anisotropy analysis

The simulation results, shown in Figure 50, suggest that λ_z has a large effect on the temperature distribution over a significant distance from the center of excitation. A factor of 10 difference in λ_z produces a factor of 2 increase in the temperature distribution and this effect persists as we move away from the center of excitation, finally decaying at approximately 5 µm away from the impact point. On the other hand, when we change λ_r by a factor of 10, the effect on temperature distribution is limited mostly to the region close to the center of excitation (i.e. x=0 µm) and this effect decays rapidly as observation point goes away from the origin. At a distance of x=2.5 µm, the effect of λ_r is already negligible, at a value of 3 and 2 millikelvin when λ_z =1 $Wm^{-1}K^{-1}$ and 10 $Wm^{-1}K^{-1}$, respectively.

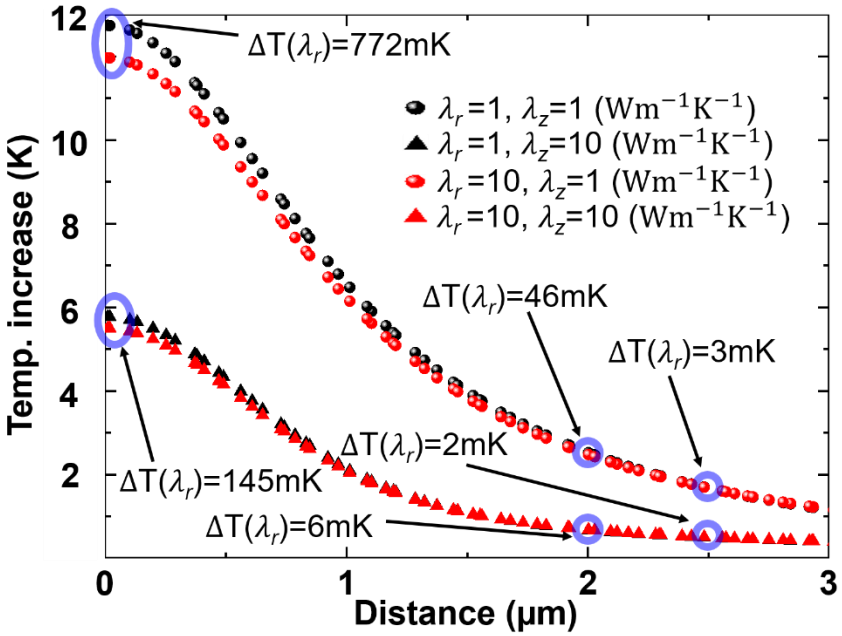

Figure 50. Impact of the thin film thermal conductivity anisotropy on the temperature increase.

These results suggest that, for the case shown, the effect on the temperature increase profile due to λ_r and λ_z can be separated when inspecting temperature distribution at lengths close to the center of excitation, x < 2 µm. The value of λ_r of the analyzed thin film can be estimated by inspecting the temperature distribution at the center of excitation (i.e. x=0 µm), where λ_r presents its most notable influence. Diversely, λ_z can be estimated when the inspecting point is placed at a further distance from the center of excitation (e.g. x=2 µm), where the effect λ_z on heating persists but the effect of λ_r is small.

The system sensitivity to variations of λ_z at 2 μm away from the excitation point for λ_r=1 $Wm^{-1}K^{-1}$ and 10 $Wm^{-1}K^{-1}$ is shown in Figure 51. Results indicate that as the value of λ_z increases, the system sensitivity decreases rapidly and this behavior is not significantly affected by λ_r variations from 1 $Wm^{-1}K^{-1}$ to 10 $Wm^{-1}K^{-1}$.

A system sensitivity study to variations of λ_r at the center of excitation was undertaken for λ_z = 1 $Wm^{-1}K^{-1}$ and 10 $Wm^{-1}K^{-1}$ as it is shown in Figure 52. It was found that as λ_r increases, the system sensitivity decreases linearly. Additionally, variations of λ_z revert to an attenuation of the sensitivity curve slope.

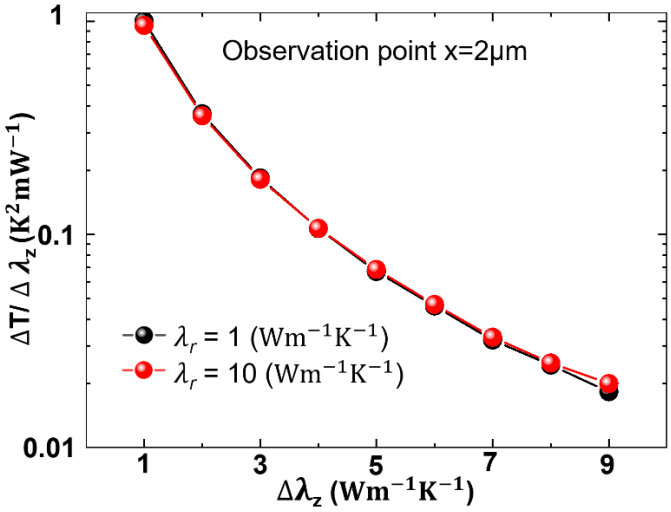

Figure 51. System sensitivity of small λ_z variations when λ_r =1 $Wm^{-1}K^{-1}$ and λ_r =10 $Wm^{-1}K^{-1}$ at 2 μm away from the excitation point.

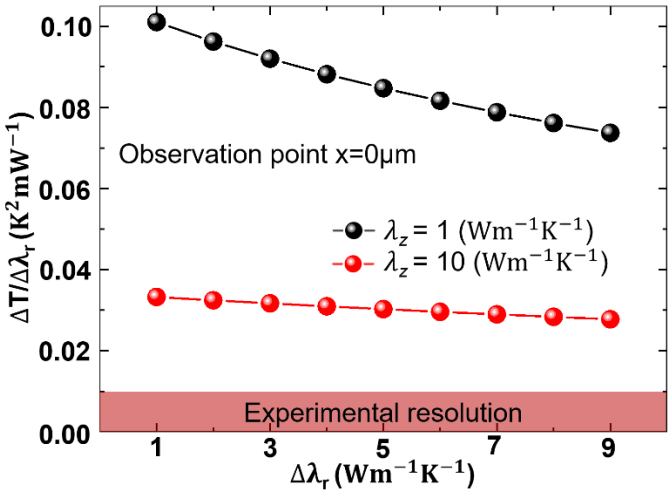

Figure 52. System sensitivity of small λ_r variations when λ_z =1 $Wm^{-1}K^{-1}$ and λ_z =10 $Wm^{-1}K^{-1}$ at the center of excitation. The system temperature resolution is indicated in the figure [97, 98].

This confirms that the system is capable to detect changes of both λ_z and λ_r within a range from 1 $\mathrm{Wm^{-1}K^{-1}}$ to 10 $\mathrm{Wm^{-1}K^{-1}}$, since the temperature variations generated from such thermal conductivity changes are above the system sensitivity threshold of 10 millikelvin [97, 98]. Furthermore, these numerical calculations are of a conservative character, since the amplitude of the temperature distributions are expected to be larger due to P_0 fluctuations. Similarly, improvements in experiment configuration and choice of pump laser can enhance the experimental conditions.

5.5.2 Effect of the laser power on the temperature distribution

As previously discussed, it was observed experimentally that substantial variations of P_0 can occur while performing an all-optically pumped thermoreflectance measurement. Therefore, it is necessary to rule out the effect of P_0 for determining the thermal properties of the problem thin film.

Numerical simulations demonstrated that the surface temperature increases linearly with P_0 at small distances from the center of excitation, independently of thin film λ_r and λ_z. Hence, due to the different trends of the temperature response towards P_0 and λ_z, both effects can be ruled out by FEM. P_0 causes a linear increase of ΔT, while λ_z causes a non-linear change of ΔT. To illustrate these results, the obtained temperature maps at 2 µm away from the excitation point were generated as a function of λ_z and P_0, as shown in Figure 53.

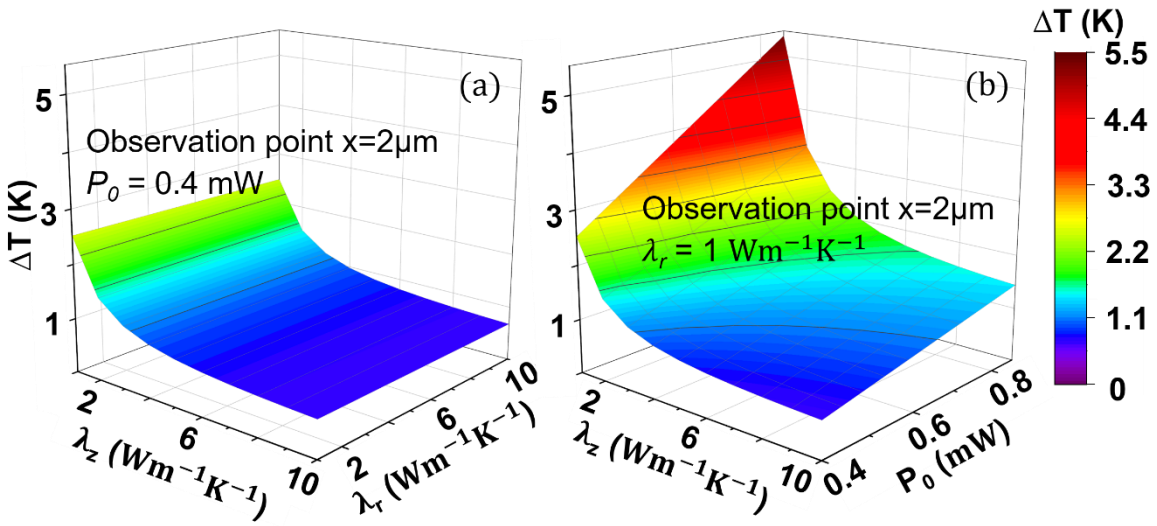

Figure 53. Effect of P_0 on the temperature increase. a) Temperature map at x=2 µm, as a function of λ_z and λ_r when P_0 is fixed at 0.4 mW. b) Temperature map, at x=2 µm, as a function of λ_z and P_0 when λ_r is fixed at 1 Wm^{-1}K^{-1}.

5.5.3 Enhancement of the system sensitivity

The preceding numerical analysis suggests that the system is dominated by the high value of the thermal conductivity of the substrate (in the analyzed sample MgO), which effectively drains away the heat that was deposited by the pump laser. Hence, the viability of enhancing the system sensitivity by reducing the thermal conductivity of the substrate, $\lambda_{substrate}$, was analyzed. The effect that λ_r variations from 1 $Wm^{-1}K^{-1}$ to 10 $Wm^{-1}K^{-1}$ present on the temperature increase at the center of excitation when the isotropic thermal conductivity of the heat sink is reduced was calculated. This was performed for the cases of λ_z fixed at 1 $Wm^{-1}K^{-1}$ and 10 $Wm^{-1}K^{-1}$. It was found that as the $\lambda_{substrate}$ decreases from ranges between 60 $Wm^{-1}K^{-1}$and 10 $Wm^{-1}K^{-1}$, the system sensitivity slowly increases. This is dramatically improved after $\lambda_{substrate}$ decreases lower than ~10 $Wm^{-1}K^{-1}$. Furthermore, when $\lambda_{substrate}$ is higher than ~8 $Wm^{-1}K^{-1}$, the variations of λ_r are more pronounced when λ_z presents a value of 1 $Wm^{-1}K^{-1}$. This condition is inversed when $\lambda_{substrate}$ is below ~8 $Wm^{-1}K^{-1}$. At that point, higher values of λ_z further enhance the system sensitivity towards λ_r changes. This means, a high $\lambda_{substrate}$ has a strong impact on the sensitivity towards λ_z, a low $\lambda_{substrate}$ has a strong impact towards λ_r. These results are depicted in Figure 54.

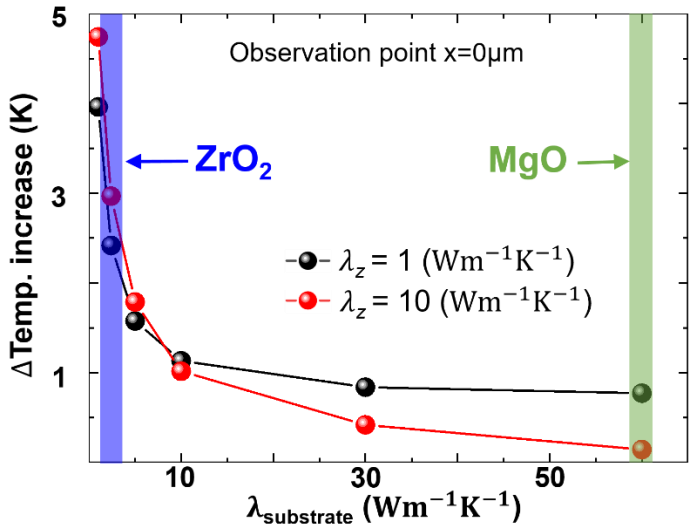

Figure 54. System sensitivity to variations of λ_r as a function of $\lambda_{substrate}$. The system sensitivity to variations of λ_r from 1 $Wm^{-1}K^{-1}$ to 10 $Wm^{-1}K^{-1}$ can be improved when the isotropic thermal conductivity of the substrate is reduced. This was calculated for λ_z values of 1 $Wm^{-1}K^{-1}$ and 10 $Wm^{-1}K^{-1}$. The thermal conductivities corresponding to substrates of MgO (60 $Wm^{-1}K^{-1}$) and ZrO_2 (2.4 $Wm^{-1}K^{-1}$) are indicated in the figure.

To illustrate how the experimental sensitivity can be improved by the choice of substrate, a system sensitivity analysis was performed considering a ZrO_2 substrate with an isotropic $\lambda_{substrate}$ of 2.4 $Wm^{-1}K^{-1}$. The numerically calculated system sensitivity to variations in λ_z

at a distance of 2 µm from the center of excitation and to variations in λ_r at the impact point is summarized in Figure 55 a) and b), respectively. The analysis determined that when a ZrO_2 substrate is considered, the system sensitivity to changes in λ_z shows a slow linear decay. This response presents a small offset that reduces its value as λ_r increases. This sensitivity curve represents a clear improvement for the case of λ_z values higher than 4 $Wm^{-1}K^{-1}$ compared to the sensitivity results of a MgO substrate, as shown in Figure 55 a). It was estimated that significant enhancements of the sensitivity of the system towards variations of λ_r between 1 $Wm^{-1}K^{-1}$ and 10 $Wm^{-1}K^{-1}$ are observed when the thin film is deposited on a ZrO_2 substrate, compared to the sensitivity results of a MgO substrate. It was found that increments of λ_z additionally enhance the sensitivity of the system towards λ_r variations, as shown in Figure 55 b).

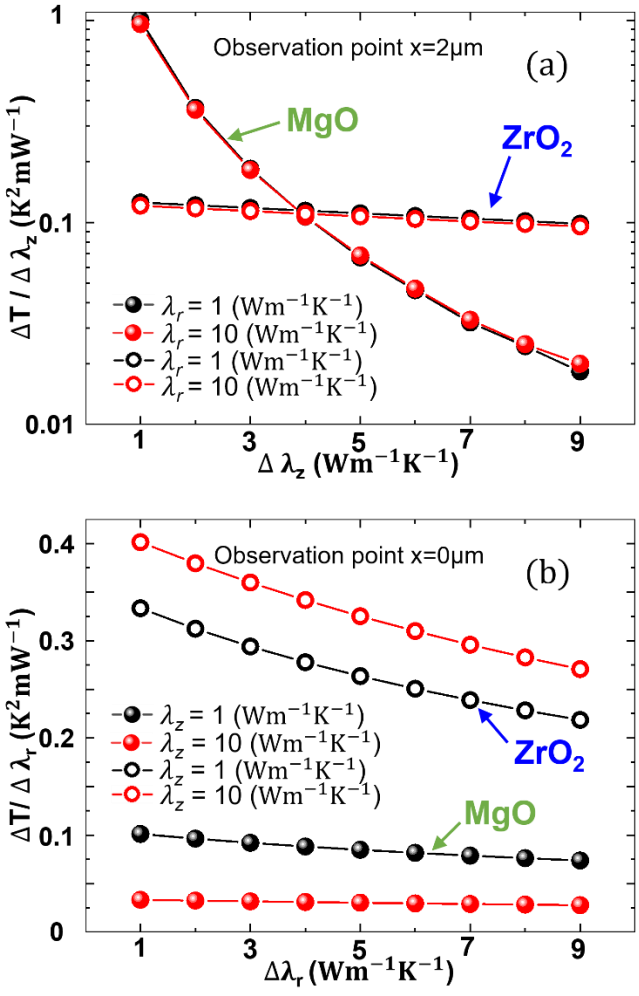

Figure 55. Improvement of the system sensitivity to variations of λ_z and λ_r as a function of $\lambda_{substrate}$. a) System sensitivity of small λ_z variations at x=2 µm for a substrate of MgO and ZrO_2. b) System sensitivity of small λ_r variations at x=0 µm for a substrate of MgO and ZrO_2.

The results illustrate that with the reduction of $\lambda_{substrate}$ the overall resistance of the system to the heat flux in the through-plane direction is strongly restricted and thus the temperature distribution is less sensitive to changes in λ_z. A highly restricted heat flux through-plane in the system as a whole pushes the heat flux to be more susceptible to move towards the in-plane direction and less susceptible to flow towards the through-plane direction within the thin film. This leads to an offset towards higher values of the sensitivity curve obtained and λ_r to become the dominating mechanism. Results also confirmed that the system is capable to detect variations of both λ_z and λ_r within a range from 1 $\mathrm{Wm^{-1}K^{-1}}$ to 10 $\mathrm{Wm^{-1}K^{-1}}$ in the conservative scenario of low P_0.

5.6 Summary

This chapter was dedicated to the development of an experimental method to characterize the anisotropic thermal conductivity of materials deposited as thin films. A sample, whose thermal conductivity properties were known, was used as a model system for the validation of this study. It was thermally excited by optical pump-probe thermoreflectance imaging microscopy and the temperature distributions generated on its surface were simultaneously recorded. The experimental data were later used as correlation parameters for a FEM, which allowed us to perform a numerical analysis of the impact that key experimental factors present on the surface temperature distribution.

It was found that roughness and defects of the sample surface are key experimental criteria, since they can provoke variations on the laser power absorption between 0.4 mW and 0.8 mW, leading to temperature increases of ~4 K and ~8 K in amplitude for the particular sample analyzed.

Furthermore, it was observed that the signal-to-noise ratio of the experimental data as well as the agreement between experimental and FEM values was improved as the amplitude of the measured temperature increases.

The effect of the laser power was found to be linear on the temperature increase and therefore it can be ruled out by the FEM. Fitting the temperature increase maps with 3D Lorentzian distributions proved to be an appropriate approach to reduce the inherent noise from the measurement.

It was numerically estimated that the thin-film λ_z can be extracted by inspecting the temperature dependence at a finite distance from the center of excitation, for example at 2 μm from the center of the focused pump spot. Similarly, λ_r can be extracted by inspecting the temperature dependence at the center of excitation. Variations of both λ_z and λ_r from 1 $\mathrm{Wm^{-1}K^{-1}}$ to 10 $\mathrm{Wm^{-1}K^{-1}}$ were found to provoke changes on the sample's surface temperature distribution greater than the experimental measurement resolution of 10 millikelvin.

FEM proved that reducing the thermal conductivity of the substrate can increase the overall system sensitivity towards variations of λ_z and λ_r. Furthermore, it was found that λ_r becomes the dominating mechanism when $\lambda_{substrate}$ is below 5 $\mathrm{Wm^{-1}K^{-1}}$.

This leads to the conclusion that an optimal experimental condition to characterize λ_z and λ_r can be achieved by performing measurements of optical pump-probe thermal imaging on two different systems. In the first system, the investigated thin film is deposited on a substrate with a high $\lambda_{substrate}$ value, while in the other system $\lambda_{substrate}$ presents a value below 5 $\mathrm{Wm^{-1}K^{-1}}$.

“Creo que cualquier cosa que tenga privilegios tiene responsabilidad y toda la gente que tiene claras sus responsabilidades tiene compromiso.”

“I believe that anything that brings privileges brings responsibilities and everybody who is clear about his responsibilities has a commitment.”

– Carlos Slim Helú, mexican entrepreneur and philanthropist, * 1940 –

6 Main conclusion and future research

6.1 Main conclusion

In the present thesis experimental and numerical analysis approaches have been used to investigate electrothermal phenomena occurring in thermoelectric materials and devices at the micro-scale. In particular, three different aspects were systematically studied. First, the development of a novel design approach specifically tailored to improve the performance optimization of μTECs. These results were then used to examine key factors involved in the practical implementation of a novel experimental platform for biological research based on μTECs. The last section of this work focused on the development of a characterization technique capable to extract the thermal conductivity anisotropy of thin films, which is suitable for a wide range of thermoelectric materials that typically present low thermal conductivity values.

A comprehensive study on certain criteria for the design and fabrication of μTECs was undertaken. This study summarized a quantitative analysis of the detrimental impact on the device performance caused by key design and construction factors, taking into account realistic material properties and device dimensions. It was demonstrated that neglecting the impact of the metallic contacts during the design of μTECs is not an adequate approach. Poorly designed contacts increase losses in performance due to Joule heating. Furthermore, the impact of the top contact was found to be particularly relevant because of its dual role as an electric and thermal contact. It was found that the metallic contacts can be optimized by constructing them with a similar size to the one selected for the thermoelectric elements.

A study, regarding the effect that the geometry of thermoelectric legs causes to the device performance, showed that the lowest point of temperature at the cold junction is found when the contributions of the Joule heating and Fourier heat conduction across the device are mutually balanced.

It was demonstrated that the fill factor plays a major role in the achieved device performance. The optimal fill factor of the analyzed μTECs was found to be lower than typical values of commercially available optimized macroscopic devices.

The results were followed by a conceptual development study of a platform that can take advantage of the highly localized temperature control capabilities of μTECs for biological micro-system experiments. First, the key factors that are required to adapt an array of μTECs for the particular experimental purpose were identified, such as embedding and isolating processes. The relationship that these processes present on the platform's capability to locally and precisely control temperature was studied. Based on this analysis, guidelines were provided specifically for the dimensioning and choice of embedding and isolating materials and generally

for optimizing the distance between adjacent arrays of thermoelectric elements. The study demonstrated the viability of μTECs as a technology for the research of thermal phenomena in micro-biological systems. It was estimated that temperature gradients of around 5.3 K with high spatial resolution can be achieved with this platform. In addition, different assays on the same platform can be run simultaneously. Guidelines for the practical construction of the experimental platform were provided.

The last section of this work was dedicated to the development of a characterization technique for the anisotropy thermal transport in thin films by thermal imaging and numerical simulations. A previously characterized sample was used as a model system for the validation of the technique. A pump laser beam was used to thermally excite the investigated sample and the temperature field produced on its surface was recorded. The experimental data were used as a correlation criteria for a FEM, which replicated with high precision the recorded temperature distribution by numerically calculated values.

An analysis performed with the correlated FEM indicated that this measurement approach is highly sensitive to roughness and small defects that may be present on the surface of the sample under test. They can carry important variations in the laser power that is absorbed by the sample during experimentation. These variations were observed between 0.4 and 0.8 mW, which reverted to temperature increases between ~4 and ~8 K in amplitude. The intensity of the laser power absorbed and the subsequent temperature increase presents a strong influence on the experimentally measured signal-to-noise ratio. It was observed that this improves with the increments of the absorbed laser power. Likewise, the agreement between the experimental and numerical values benefits as the absorbed laser power increases.

Despite the large impact that the absorbed laser presents on the recorded temperature increase, it was found that its influence can be ruled out by the numerical simulations, due to its linear effect on the surface temperature. It was also demonstrated that a Lorentzian distribution is adequate to express the generated temperature profile.

The effect that the thin film through-plane and in-plane thermal conductivities have on the generated temperature increase at the sample's surface was investigated. It was concluded that the first parameter can be estimated by analyzing the temperature increase at a finite distance from the center of excitation, where its impact is dominant with respect to the in-plane thermal conductivity. In contrast, the in-plane thermal conductivity can be estimated by analyzing the temperature dependence at the center of excitation, where its influence presents the largest effect. It was shown that variations of both parameters from 1 $\mathrm{Wm^{-1}K^{-1}}$ to 10 $\mathrm{Wm^{-1}K^{-1}}$ can be measured experimentally.

Finally, the study demonstrated that the choice of substrate on which the thin film is deposited plays a major role in the system sensitivity. For high thermal conductivity values of the substrate, the through-plane thermal conductivity of the thin film is the dominate mechanism. This condition is inversed when the thermal conductivity of the substrate is lower than

5 $Wm^{-1}K^{-1}$. Thus, it was proposed that an optimal experimental scenario for the characterization of the through-plane and in-plane thermal conductivities of a thin film can be performed by running two different experiments while considering two different samples. The only difference between the samples being the substrate material used: the first featured with substrate whose thermal conductivity is high, and the second sample deposited on a substrate with a thermal conductivity below 5 $Wm^{-1}K^{-1}$.

6.2 Outlook

All shown results contributed to the development of experimental and numerical approaches to further understand electrothermal phenomena at the micro-scale. The approach pursued in this work placed particular emphasis on: i) the development of optimization strategies for next generation micro-thermoelectric coolers, ii) the development of an experimental platform to study thermal effects in biological microsystems, and iii) the evaluation of a characterization technique to extract the thermal conductivity anisotropy of materials deposited as thin films.

The outcomes of the design study are a guideline for the construction of next generation micro-devices. Novel considerations can be assessed to overcome the rapid decrement of the device performance as a result of an increased fill factor. This includes the use of materials with high thermal conductivity for the choice of the substrate as well as auxiliary temperature control for the heat sink by microfluidic channels.

This thesis demonstrated the viability of using micro-thermoelectric coolers to fabricate a platform for thermal experimentation on microbiological systems. Guidelines for its design and construction were provided. Upon successful implementation of this set up, this research line can be continued by performing simple studies, such as selective control of cell viability. Afterwards, more advanced experiments can be considered, such as spatially selective lysing of detection assays, exploring thermotaxis at the cellular level and control and manipulation of biosystems, and miniaturized PCR processes. The systems to be investigated can be a variety of human and animal biological cells, such as HeLa, blood, and neuronal, proteins, and biological macromolecules like DNA.

The last aspect of this work demonstrated the applicability of optical pump-probe thermoreflectance imaging and numerical simulations to estimate the thermal conductivity anisotropy of thin films. Further studies may be performed by analyzing materials deposited as thin films in substrates with low and high thermal conductivities. The experimental set up used for the results shown in this work presented considerably high noise levels due to the lack of a piezoelectric stage required to compensate for the thermal expansion that the system might be exposed. Further development of the experimental apparatus may be pursued. Further studies are needed to understand the mechanisms that determine the effect of the roughness on the absorbed laser power in order to control the temperature fluctuations. The effect that the thermal contact resistances present on the measured temperature distributions was neglected from the FEM results shown in this work, due to the lack of reliable experimental values. This factor iins expected to present an offset effect on the numerically calculated temperature distributions and therefore its impact can be assessed to increase the precision of the experimental characterization method. Finally, the applicability of the proposed technique can be expanded by analyzing the technique sensitivity in the case of thick film samples.

7 References

[1] Ziabari, A., "Finite element and imaging approaches to analyze multiscale electrothermal phenonema", Purdue University, Doctoral Thesis (2016).

[2] Li, G., Garcia Fernandez, J., Lara Ramos, D., Barati, V., Pérez, N., Soldatov, I., Reith H., Schierning G., and Nielsch K. Integrated micro-thermoelectric coolers with rapid response time and high device reliability. *Nature Electronics 1*, 555–561 (2018).

[3] Snyder, G., Lim, J., Huang, C.-K., and Fleurial, J.-P. Thermoelectric microdevice fabricated by a MEMS-like electrochemical process. *Nature Materials 2*, 528–531 (2003).

[4] Enright, R., Lei, S., Nolan, K., Mathews, I., Shen, A., Levaufre, G., Frizzell, R., Duan, G.-H., and Hernon, D. A vision for thermally integrated photonics systems. *Bell Labs Technical Journal 19*, 31–45 (2014).

[5] Enright, R., Cunningham G., Mathews, I., Frizzell, R., and Shen, A. Integrated Thermoelectric Cooling for Silicon Photonics. *ECS Journal of Solid State Science and Technology 6,* N3103– N3112 (2017).

[6] Enright, R, Lei, S., Mathews, I., Cunningham, G., Frizzell, R., and Shen, A. (Invited) Electrodeposited Micro Thermoelectric Module Design for Hybrid Semiconductor Laser Cooling on a Silicon Photonics Platform. *ECS Transactions 69 (9),* 37–51 (2015).

[7] García, J., Lara Ramos, D., Mohn, M., Schlörb, H., Rodriguez, N., Akinsinde, L., Nielsch, K., Schierning, G., and Reith, H. Fabrication and Modeling of Integrated Micro-Thermoelectric Cooler by Template-Assisted Electrochemical Deposition. *ECS Journal of Solid State Science and Technology 6*, N3022-N3028 (2017).

[8] Seebeck, T.J. Ueber den Magnetismus der galvanischen Kette. Berlin, Königlichen Akademie der Wissenschaft in Berlin (1822).

[9] Rowe D. M and Bhandari C. M. Modern Thermoelectrics. New York City, Holt, Rinehart and Winston (1983).

[10] Peltier, J. C. A. Nouvelles expériences sur la caloricité des courants électrique. *Annales de Chimie et de Physique 56*, 371–386 (1834).

[11] Goldsmid, H. J. Introduction to Thermoelectricity, First Edition. Heidelberg, Springer Series in Materials Science (2010).

[12] Thomson, W. Account of Researches in Thermo-Electricity. *Philosophical Magazine 8,* 49–58 (1854).

[13] Mishra, A., Bhattacharjee, S., and Anwar, S. Simple apparatus to measure Seebeck coefficient up to 900 K. *Measurement 68*, 295–301 (2015).

[14] Borup, K.A., de Boor, J., Wang, H., Drymiotis, F., Gascoin, F., Shi, X., Chen L., Fedorov M. I., Mueller, E., Iversen, B. B. , and Snyder, G. J. Measuring thermoelectric transport properties of materials. *Energy & Environmental Science 8*, 423–435 (2015).

[15] Courant, R. Variational methods for the solution of problems of equilibrium and vibrations. *Transactions of the American Mathematical Society 49 (1)*, 1–23 (1943).

[16] Logan, D. L. A First Course in the Finite Element Method, Fifth Edition. Boston, Cengage Learning (2011).

[17] Thompson, M.K, and Thompson, J. M. ANSYS Mechanical APDL for Finite Element Analysis. Oxford, Butterworth-Heinemann (2017).

[18] Jaegle, M. Multiphysics Simulation of Thermoelectric Systems - Modeling of Peltier-Cooling and Thermoelectric Generation. *Excerpt from the Proceedings of the COMSOL Conference in Hannover* (2008), https://www.comsol.de/paper/download/37149/Jaegle.pdf [last downloaded 2020/03/31].

[19] Antonova, E.E., and Looman, D.C. Finite Elements for Thermoelectric Device Analysis in ANSYS. *Proceedings of the 24th International Conference on Thermoelectrics ICT in Clemson,* 215–218 (2005).

[20] Christofferson, J., Maize, K., Ezzahri, Y. and Shabani, J. and Wang, X., and Shakouri, A. Microscale and Nanoscale Thermal Characterization Techniques. *Journal of Electronic Packaging 130 (4)* (2008).

[21] Li, B., Pottier, L., Roger, J.P. Fournier, D., Watari, K., and Hirao, K. Measuring the anisotropic thermal diffusivity of silicon nitride grains by thermoreflectance microscopy. *Journal of the European Ceramic Society 19*, 1631–1639 (1999).

[22] Mansanares, A. M., Velinov, T., Bozoki, Z., Fournier, D., and Boccara, A. Photothermal Microscopy: Thermal Contrast at Grain Interface in Sintered Metallic Materials. *Journal of Applied Physics 75 (7)*, 3344-3350 (1994).

[23] Maize, K. High Resolution Thermoreflectance Imaging of Power Transistors and Nanoscale Percolation Network. Santa Cruz, University of California (2014).

[24] Vermeersch, B., Maize, K., Shakouri, A., and Mey G. Time and Frequency Domain CCD-Based Thermoreflectance Techniques for High-Resolution Transient Thermal Imaging. 26th *Annual IEEE Semiconductor Thermal Measurement and Management Symposium in Santa Clara*, 228–234 (2010).

[25] Raad, P.E. Thermo-Reflectance Thermography For Submicron Temperature Measurements. *Electronics Cooling 14* (2008), https://www.electronics-cooling.com/2008/02/thermo-reflectance-thermography-for-submicron-temperature-measurements/ [last downloaded 2020/03/31].

[26] Schumacher, C., Reinsberg, K.-G., Akinsinde, L., Zastrow, S., Heiderich, S.,Töllner, W., Rampelberg, G., Detavernier, C., Broeckaert, J., Nielsch, K., and Bachmann, J. Optimization of Electrodeposited p-Doped Sb2Te3 Thermoelectric Films by Millisecond Potentiostatic Pulses. *Advanced Energy Materials 2 (3),* 345–352 (2012).

[27] Schumacher, C., Reinsberg, K.-G., Rostek, R., Akinsinde, L., Baessler, S., Zastrow, S., Rampelberg, G., Woias, P., Detavernier, C., Broekaert, J., Bachmann, J., and Nielsch, K. Optimizations of Pulsed Plated p and n-type Bi2Te3-Based Ternary Compounds by Annealing in Different Ambient Atmospheres. *Advanced Energy Materials* 3 (1), 95–104 (2013).

[28] Fraisse, G., Ramousse, J., Sgorlon D., and Goupil, C. Comparison of different modeling approaches for thermoelectric element. *Energy Conversion and Management 65*, 351–356 (2013).

[29] Huang, B.-J., Chin, C.J., and Duang, C.L. A design method of thermoelectric cooler. *International Journal of Refrigeration 23*, 208–218 (2000).

[30] Voelklein, F., Min, G., and Rowe, D.M. Modelling of a microelectromechanical thermoelectric cooler. *Sensors and Actuators A: Physical 75*, 95–101 (1999).

[31] Astrain, D., Vián, J.G., and Albizua, J. Computational model for refrigerators based on Peltier effect application. *Applied Thermal Engineering 25*, 3149–3162 (2005).

[32] Vashaee, D., Christofferson, J., Zhang, Y., Shakouri, A., Zeng, G., LaBounty, C., Fan, X., Piprek, J., Bowers, J., and Croke, E. Modeling and optimization of single-element bulk SiGe thin-film coolers. *Microscale Thermophysical Engineering 9*, 99–118 (2005).

[33] Ioffe, A. F. Semiconductor thermoelements, and thermoelectric cooling. London, Infosearch Ltd. (1957).

[34] Moore, G. E. Cramming more components onto integrated circuits. *Electronics 38 (8)* (1965).

[35] Morini, G. Single-phase convective heat transfer in microchannels: a review of experimental results. *International Journal of Thermal Sciences 43*, 631–651 (2004).

[36] Mudawar I. Two-Phase Microchannel Heat Sinks: Theory, Applications and Limitations. *Journal of Electronic Packaging 133 (4)* (2011).

[37] O'Donovan, T. S., and Murray D. B. Fluctuating fluid flow and heat transfer measurements of an impinging air jet. *13th International Symp on Applications of Laser Techniques to Fluid Mechanics in Lisbon* (2006).

[38] Cheng, W.-L., Zhang, W.-W., Chen, H., and Hu, L. Spray cooling and flash evaporation cooling: The current development and application. *Renewable and Sustainable Energy Reviews 55,* 614–628 (2016).

[39] Chowdhury, I., Prasher, R., Lofgreen, K., Chrysler, G., Narasimhan, S., Mahajan, R., Koester, D. Alley, R., and Venkatasubramanian, R. On-Chip Cooling by Superlattice-Based Thin-Film Thermoelectrics. *Nature Nanotechnology 4*, 235–238 (2009).

[40] Wang, P., Bar-Cohen, A., Yang, B., Solbrekken, G.L., and Shakouri, A. Analytical modeling of silicon thermoelectric microcooler. *Journal of Applied Physics 100*, 014501–014501 (2006).

[41] Qu, W., Plötner, M., and Fischer, W.-J. Microfabrication of thermoelectric generators on flexible foil substrates as a power source for autonomous microsystems. *Journal of Micromechanics and Microengineering 11* (108), 97–102 (2003).

[42] Kishi, M., Yoshida, Y., Okano, H., Nemoto, H., Funanami, Y., Yamamoto, M., Kanazawa, H. Fabrication of a miniature thermoelectric module with elements composed of sintered Bi-Te compounds. *Proceedings of the 16th International Conference on Thermoelectrics ICT in Dresden,* 653–656 (1997).

[43] Bottner, H., Nurnus, J., Gavrikov, A., Kuhner, G., Jaegle, M., Kunzel, C., Eberhard, D., Plescher, G., Schubert, A., and Schlereth, K.-H. New thermoelectric components using microsystem technologies. *Journal of microelectromechanical systems 13 (3)*, 414–420 (2004).

[44] Wendt H., and Kreysa G. Electrochemical Engineering: Science and Technology in Chemical and Other Industries. Berlin, Springer Science & Business Media (1999).

[45] Lara Ramos, D., Barati, V., García, J., Reith, H., Li, G., Pérez, N., Schierning, G., and Nielsch, K. Design Guidelines for Micro-Thermoelectric Devices by Finite Element Analysis. *Advanced Sustainable Systems 3 (2),* 1800093 (2019).

[46] Gordiz, K., Menon, A., and Yee, S. Interconnect patterns for printed organic thermoelectric devices with large fill factors. *Journal of Applied Physics 122 (12)*, 124507 (2017).

[47] Barati, V., García, J., Geishendorf, K., Schnatmann, L., Lammel, M., Kunzmann, A., Pérez, N., Li, G., Schierning, G., Nielsch, K., and Reith, H. Thermoelectric Characterization Platform for Electrochemically Deposited Materials. *Advanced Electronic Materials 1901288* (2020).

[48] Helmer Sientific. Countertop Refrigerators. Laboratory/Pharmacy. https://www.helmerinc.com/sites/default/files/2019-04/countertop-refrigerator-380395-1.pdf. [last downloaded 2020/03/31].

[49] MacPherson, E. T., Bridges C.A., and Peters, R. K. Thermoelectric medicine cooling bag. United States Patent, Patent version number 5,865,032, Application number 991, 223 (1999).

[50] Deutsch, R. Thermoelectric therapy device. United States Patent, Patent Version number 5,097,828, Application number 587,407 (1992).

[51] Tu, H. Medical device having temperature sensing and ablation capabilities. United States Patent, Patent version number 6,451,011 B2, Application number 09/827,692 (2002).

[52] Johnson, N. Thermoelectrically controlled heat medical catheter. World intellectual property organization, Patent version number WO 89/04137 (1989).

[53] Jain, A., and Goodson, K. Thermal microdevices for biological and biomedical applications. *Journal of Thermal Biology 36 (4),* 209–218 (2011).

[54] Ryu, W., and Samuel, A. Thermotaxis in Caenorhabditis elegans Analyzed by Measuring Responses to Defined Thermal Stimuli. *The Journal of neuroscience : the official journal of the Society for Neuroscience 22 (3)*, 5727–5733 (2002).

[55] Hedgecock, E., and Russell, R. Normal and mutant thermotaxis in the nematode Caenorhabditis elegans. *Proceedings of the National Academy of Sciences of the United States of America 72*, 4061–4065 (1975).

[56] Brambrink, A., Kopacz, L., Astheimer, A., Noga, H., Heimann, A., and Kempski, O. Control of brain temperature during experimental global ischemia in rats. *Journal of neuroscience methods 92,* 111–122 (1999).

[57] Childs, C., and Machin, G. Reliability issues in human brain temperature measurement. *Critical Care 13 (4)*, R106 (2009).

[58] Roemer, R. B. Engineering aspects of hyperthermia therapy. *Annual review of biomedical engineering 1 (1)*, 347–376 (1999)

[59] Davis, H. K. S. Observations on the response of goldfish to temperature gradients. *American Zoologist 11 (4),* 695 (1971).

[60] Mori, I., and Ohshima,Y. Neural regulation of thermotaxis in Caenorhabditis elegans. *Nature 376,* 344–348 (1995).

[61] Mullis, K., and Faloona, F. Specific synthesis of DNA in vitro via a polymerase-catalyzed chain reaction. *Methods in enzymology 155,* 335–350 (1987).

[62] Saiki, R. K., Gelfand, D. H., Stoffel, S. J., Scharf, S. J., Higuchi, R., Horn, G. T., Mullis, K., and Erlich, H. A. Primer-directed enzymatic amplification of DNA with a thermostable DNA polymerase. *Science 239 (4839),* 487–491 (1988).

[63] Jain, A., Ness, K., and Goodson K. Theoretical and experimental investigation of spatial temperature gradient effects on cells using a microfabricated microheater platform. *Sensors and Actuators B-chemical 143 (1)*, 286–294 (2009).

[64] Petersen K. E. Silicon as a mechanical material. *Proceedings of the IEEE 70 (5),* 420–457 (1982).

[65] Kovacs, G. T. A. Micromachined Transducers Sourcebook, Second Edition. New York City, McGraw-Hill (1984).

[66] Trimmer, W. S. Micromechanics and MEMS: Classic and Seminal Papers to 1990. New York City, Wiley-IEEE Press (1997).

[67] McDonald, J., Duffy, D., Anderson, J., Chiu, D., Wu, H., Schueller, O., and Whitesides, G. Fabrication of microfluidic systems in poly(dimethylsiloxane). *Electrophoresis 21 (1)*, 27–40 (2000).

[68] Labianca, N., and Gelorme. J. High aspect ratio resist for thick film applications. *Proceedings of SPIE - The International Society for Optical Engineering 2438*, 846–852 (1995).

[69] Martin, P., Matson, D., Bennett, W., Lin, Y., and Hammerstrom, D. Laminated plastic microfluidic components for biological and chemical systems. *Journal of Vacuum Science & Technology A Vacuum Surfaces and Films 17 (4),* 2264–2269 (1999).

[70] Folch, A., and Toner, M. Microengineering of cellular interactions. *Annual review of biomedical engineering 2,* 227–256 (2000).

[71] Polla, D., Erdman, A., Robbins, W., Markus, D., Diaz, J., Rizq, R., Nam, Y., Brickner, H., Wang, A., and Krulevitch, P. Microdevices in Medicine 1. *Annual review of biomedical engineering 2,* 551–576 (2000).

[72] Singh, K., and Kim, K. Clinical bio-micro-electro-mechanical systems: technology and applications. *Sensor Letters 7 (6),* 1013–1024 (2009).

[73] Purves, W., Sadava, D., Orians, G., and Heller, H. Life: The science of Biology, Sixth Edition. New York City, W.H. Freeman (2000).

[74] Woolley, A., Hadley, D., Landre, P., deMello, A., Mathies, R., and Northrup, M. Functional integration of PCR amplification and capillary electrophoresis in a microfabricated DNA analysis device. A*nalytical chemistry 68 (23)*, 4081–4086 (1996).

[75] Taylor T., Winn-Deen E., Picozza, E., Woudenberg, T., and Albin M. Optimization of the performance of the polymerase chain reaction in siliconbased microstructures. *Nucleic Acids Research 25 (15)*, 3164–3168 (1997).

[76] Kopp, M., Mello, A., and Manz, A. Chemical amplification: continuous-flow PCR on a chip. *Science 280 (5366),* 1046–1048 (1998).

[77] Khandurina K., Mcknight, T., Jacobson, S., Waters, L., Foote, R., and Ramsey, J. Integrated system for rapid PCR-based DNA analysis in microfluidic devices. *Analytical chemistry 72 (13)*, 2995–3000 (2000).

[78] Northrup, M., Ching, M., White, and R.,Watson. DNA amplification with a microfabricated reaction chamber. *Proceedings of the 7th International Conference on Solid-state Sensors and Actuators in New York City* (1993).

[79] Van den Berg, A., and Lammerink, T. Micro total analysis systems: microfluidic aspects, integration concept and applications. In: Microsystem Technology in Chemistry and Life Science, 21–49, Berlin, Springer (1998).

[80] Arora, A., Simone, G., Salieb-Beugelaar, G., Kim, J., and Manz, A. Latest Developments in Micro Total Analysis Systems. *Analytical chemistry 82 (12)*, 4830–4847 (2010).

[81] Shoffner, M., Cheng, J., Hvichia, G., Kricka, L., and Wilding, P. Chip PCR. I. Surface Passivation of Microfabricated Silicon-Glass Chips for PCR. *Nucleic acids research 24 (2),* 375–379 (1996).

[82] Prabhakar, A., Murphy, M., and Devireddy, R. Modeling of a Bio-Thermo-Electric Micro-Cooler. *The Open Biotechnology Journal 1 (1),* 1-8 (2007).

[83] Cantarella, M., Sanz, R., Buccheri, M.-A., Ruffino, F., Rappazzo, G., Scalese, S., Impellizzeri, G., Romano, L., and Privitera, V. Immobilization of nanomaterials in PMMA composites for photocatalytic removal of dyes, phenols and bacteria from water. *Journal of Photochemistry and Photobiology A Chemistry 321*, 1–11 (2016).

[84] Assael, M., Botsios, S., Gialou, K., and Metaxa, I. Thermal Conductivity of Polymethyl Methacrylate (PMMA) and Borosilicate Crown Glass BK7. *International Journal of Thermophysics 26 (5)*, 1595-1605 (2005).

[85] Yoshio, B., Wang, W., Tang, C., Hiroaki, K., and Dmitri, G. Mechanical and Thermal Properties of Polymethyl Methacrylate-BN Nanotube Composites. *Journal of Nanomaterials 1* (2008).

[86] Jiang, P., Qian, X., and Yang, R. Time-domain thermoreflectance (TDTR) measurements of anisotropic thermal conductivity using a variable spot size approach. *Review of Scientific Instruments 88 (7)* (2017).

[87] Jiang, P., Qian, X., and Yang, R. A new elliptical-beam method based on time-domain thermoreflectance (TDTR) to measure the in-plane anisotropic thermal conductivity and its comparison with the beam-offset method. *Review of Scientific Instruments 89 (9),* 094902 (2018).

[88] P. Jiang, Qian, X. and Yang, R. Tutorial: Time-domain thermoreflectance (TDTR) for thermal property characterization of bulk and thin film materials. https://arxiv.org/pdf/1807.01258.pdf [last downloaded 2020/03/31].

[89] Feser, J., and Cahill, D. Probing anisotropic heat transport using time-domain thermoreflectance with offset laser spots. *The Review of scientific instruments 83 (10)*, 104901 (2012).

[90] Feser, J., Liu, J., and Cahill, D. Pump-probe measurements of the thermal conductivity tensor for materials lacking in-plane symmetry. *The Review of Scientific Instruments 85 (10)*, 104903 (2014).

[91] Mishra, V., Hardin, C., Garay, J., and Dames, C. A 3 omega method to measure an arbitrary anisotropic thermal conductivity tensor. *The Review of Scientific Instruments 86 (5),* 054902 (2015).

[92] Ramu, A., and Bowers, J. A "2-omega" technique for measuring anisotropy of thermal conductivity. *The Review of Scientific Instruments 83 (12)*, 124903 (2012).

[93] Luckyanova, M., Johnson, J., Maznev, A., Garg, J., Jandl, A., Bulsara, M., Fitzgerald, E., and Nelson, K. Nelson, and Chen, G. Anisotropy of the Thermal Conductivity in GaAs/AlAs Superlattices. *Nano Letters 13 (9)*, 3973−3977 (2013).

[94] Ziabari, A., Torres, P., Vermeersch, B., Xuan, Y., Cartoixa, X., Torello Massana, A., Bahk, J.-H., Koh, Y.R., Parsa, M., Ye, P., Alvarez, F., and Shakouri, A. Full-field thermal imaging of quasiballistic crosstalk reduction in nanoscale devices. *Nature communications* 9 *,* 255 (2018).

[95] Christofferson, J., and Shakouri, A. Thermal measurements of active semiconductor micro-structures acquired through the substrate using near IR thermoreflectance. *Microelectronics Journal 35 (10)*, 791–796 (2004).

[96] Vermeersch, B., Bahk, J.-H., Christofferson, J., and Shakouri, A. Thermoreflectance imaging of sub 100 ns pulsed cooling in high-speed thermoelectric microcoolers. *Journal of Applied Physics 113 (10)*, 104502 (2013).

[97] Yazawa, K., Gil, J., Maze, K., Kendig, D., and Shakouri, A. Optical Pump-Probe Thermoreflectance Imaging for Anisotropic Heat Diffusion. *17th IEEE Intersociety Conference on Thermal and Thermomechanical Phenomena in Electronic Systems in San Diego,* 59-66 (2018).

[98] Lueerssen, D., Hudgings, J., Mayer, P., and Ram, R. Nanoscale thermoreflectance with 10mk temperature resolution using stochastic resonance. 21st *Annual IEEE Semiconductor Thermal Measurement and Management Symposium in San Jose,* 253–258 (2005).

[99] Saha, B., Koh, Y., Feser, J., Sadasivam, S., Fisher, T., Shakouri, A., and Sands, T. Phonon wave effects in the thermal transport of epitaxial TiN/(Al,Sc)N metal/semiconductor superlattices. *Journal of Applied Physics 121(1),* 015109 (2017).

8 Scientific output

8.1 Publications in peer review journals

1 **David Alberto Lara Ramos**, Kerry Maize, Nicolas Perez, Gabi Schierning, Kornelius Nielsch, Ali Shakouri (2020). A method to extract thermal conductivity anisotropy of thin films by optically pumped thermal imaging and finite element modelling. **Under preparation**.

2 Aditya S. Dutt, **David Alberto Lara Ramos**, Guodong Li, Javier Garcia, Vida Barati, Nicolas Perez, Kornelius Nielsch, Gabi Schierning, Heiko Reith (2020). Geometry-optimized polymer-embedded micro-thermoelectric coolers with high cooling-performance and cycling stability. **Under preparation**.

3 **David Alberto Lara Ramos**, Vida Barati, Javier Garcia, Heiko Reith, Guodong Li, Nicolás Pérez, Gabi Schierning, Kornelius Nielsch (2019). Design Guidelines for Micro-Thermoelectric Devices by Finite Element Analysis. **Advanced Sustainable Systems**. (2) 1800093.

4 Guodong Li, Javier Garcia Fernandez, **David Alberto Lara Ramos**, Vida Barati, Nicolás Pérez, Ivan Soldatov, Heiko Reith, Gabi Schierning, Kornelius Nielsch (2018). Integrated micro-thermoelectric coolers with rapid response time and high device reliability. **Nature Electronics** (10) 555-561.

5 Javier Garcia, **David Alberto Lara Ramos**, Melanie Mohn, Heike Schlörb, Nicolas Perez Rodriguez, Lewis Akinsinde, Kornelius Nielsch, Gabi Schierning, Heiko Reith (2017). Fabrication and modeling of integrated micro-thermoelectric cooler by template-assisted electrochemical deposition. **ECS Journal of Solid State Science and Technology**. (3) N3022-N3028

8.2 Selected conference abstracts

1 **David Alberto Lara Ramos**, Kerry Maize, Nicolas Perez, Gabi Schierning, Kornelius Nielsch, Ali Shakouri (2019). Finite Element Modelling of Optically Pumped Thermoreflectance. MRS 2019 Fall Meeting. Boston, USA. (Oral communication)

2 Guodong Li, Javier Garcia, **David Alberto Lara Ramos**, Vida Barati, Nicolas Perez, Ivan Soldatov, Heiko Reith, Gabi Schierning, Kornelius Nielsch (2019). Integrated Micro-Thermoelectric Coolers with Free-Standing Design and Robust Device Performance. MRS 2019 Spring Meeting. Phoenix, USA. (Oral communication)

3 Guodong Li, Javier Garcia, Tom Sieger, Lauritz Ule Schnatmann, **David Alberto Lara Ramos**, Vida Barati, Nicolas Perez Rodriguez, Heiko Reith, Gabi Schierning, Kornelius Nielsch (2018). Compact Telluride Films Prepared By Electrochemical Deposition and Their Applications for Integrated Micro- Thermoelectric Devices. AIMES 2018. Cancun, Mexico. (Oral communication)

4 **David Alberto Lara Ramos**, Vida Barati, Gabi Schierning, Heiko Reith, Kornelius Nielsch (2018). Performance simulation of micro-thermoelectric coolers. DPG-Frühjahrstagung. Berlin, Germany. (Oral communication)

5 Gabi Schierning, Guodong Li, Vida Barati, **David Alberto Lara Ramos**, Tom Sieger, Javier Garcia, Nicolas Perez Rodriguez, Melanie Mohn, Heike Schlörb, Jens Freudenberger, Heiko Reith, and Kornelius Nielsch (2017). Template Assisted Electrochemical Deposition and High Power Factor Materials for Integrated Thermoelectric Devices. 232nd ECS Meeting. National Harbor Fort Washington, USA. (Oral communication)

9 Curriculum vitae

David Alberto Lara Ramos

ing.davidlara@hotmail.com

Nationality: Mexican | Date of birth 28/03/1990

Education

06/2016 - 03/2020	Technical University Dresden. Dresden, Germany.
	Ph.D. candidate at the chair of Mechanical Engineering
	Thesis: Experimental and numerical studies of electrothermal phenomena in micro-scale thermoelectric systems.
02/2017 - 05/2017	Purdue University. West Lafayette, USA.
	Post-graduate visiting researcher at the Birck Nanotechnology Center
09/2014 - 09/2015	University of Sheffield. Sheffield, UK.
	M.Sc. Advanced Mechanical Engineering
	Thesis: Experimental investigations of composite materials under static and dynamic loading.
08/2008 - 08/2013	Queretaro Institute of Technology. Queretaro, Mexico.
	B.Sc. Mechatronics Engineering
	Thesis: Static and dynamic numerical analysis of turbofan engine components.

Professional Experience

06/2016 - 03/2020	Research assistant. Leibniz Institute for Solid State and Materials Research. Dresden, Germany.
06/2012 - 07/2014	Product Design and Development Engineer. General Electric Aviation. Queretaro, Mexico.
01/2012 - 06/2012	Factory Performance and Reliability Trainee. Colgate-Palmolive Company. Guanajuato, Mexico.

Secured Scholarships

09/2014 - 09/2015	Mexican Council of Science and Technology (CONACYT).
	Fully founded M.Sc. at the University of Sheffield.
06/2016 - 03/2020	Mexican Council of Science and Technology (CONACYT).
	Partially founded Ph.D. at the IFW-Dresden.